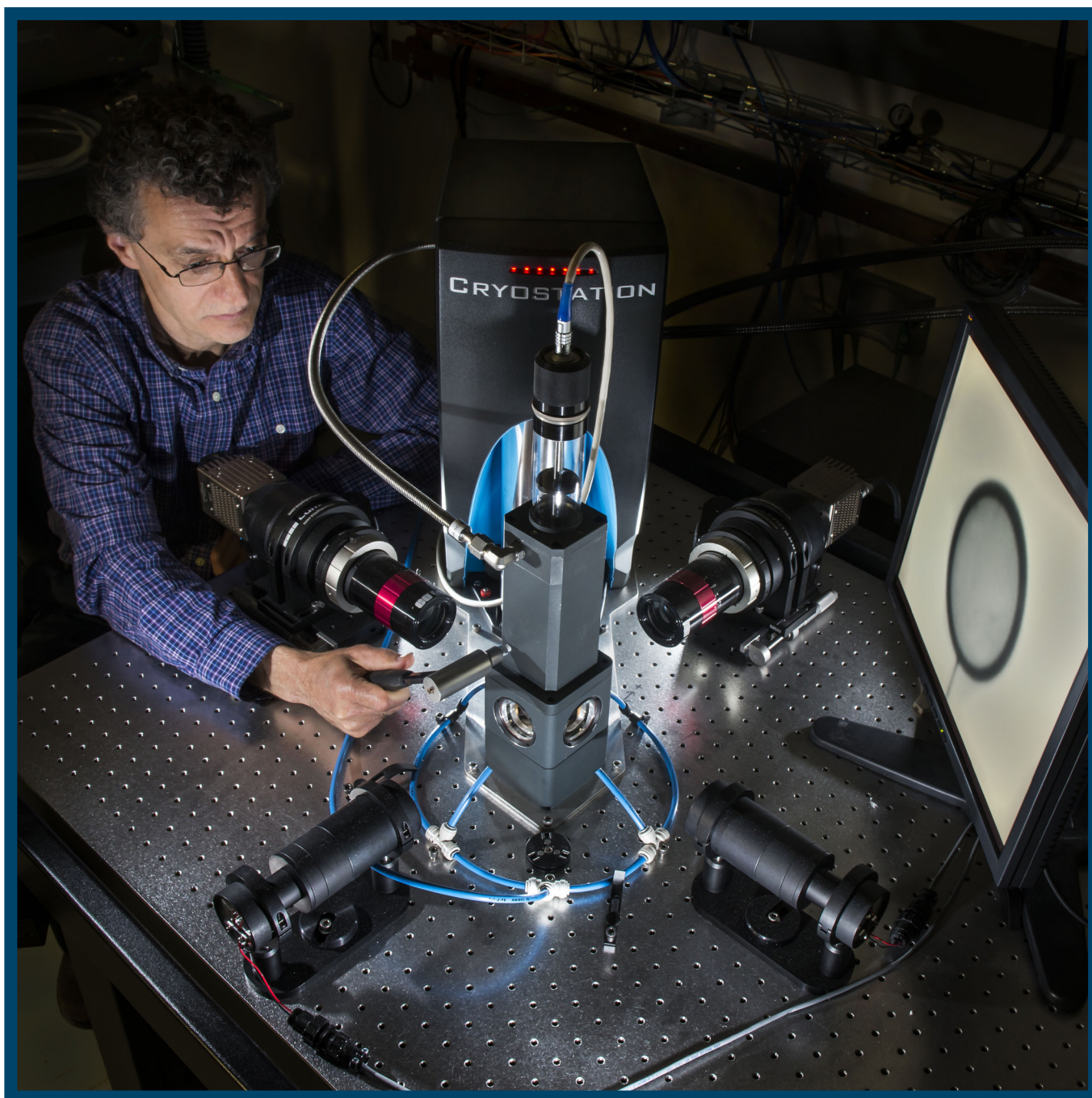


LLE Review

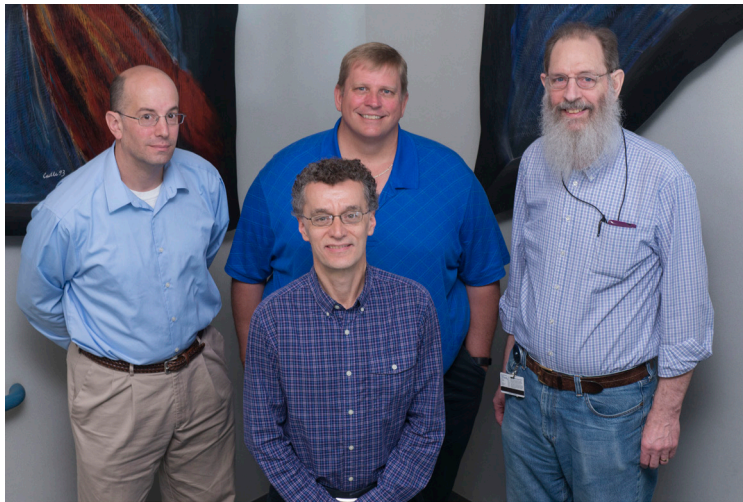
Quarterly Report



About the Cover:

The photograph on the cover features Brian Rice, a research engineer in the Mechanical Engineering Group at LLE, with the cryogenic vibration measurement test setup that was assembled at LLE and used to measure key physical properties of several types of fibers at cryogenic temperatures. The fibers were studied for their potential to provide more-stable mounting of cryogenic targets as part of LLE's direct-drive-implosion experiments on the OMEGA Laser System. The ability to maintain target positional stability of 10 μm or better prior to an implosion has been an important part of LLE's strategy to achieve higher-yield implosions on OMEGA.

The photograph below includes LLE research engineers (from left to right) Jeffrey Ulreich, Milton Shoup (LLE Mechanical Engineering Group Leader), Brian Rice, and Lance Lund. Brian Rice and Jeffrey Ulreich developed the overall concept for the experiment mentioned above, while Milton Shoup and Lance Lund designed and assembled the test setup. Joseph Quinzi (not pictured), an undergraduate in Mechanical Engineering at Clarkson University, conducted many of the experiments on the potential cryogenic target mounting fibers that were evaluated as part of this study.



This report was prepared as an account of work conducted by the Laboratory for Laser Energetics and sponsored by New York State Energy Research and Development Authority, the University of Rochester, the U.S. Department of Energy, and other agencies. Neither the above-named sponsors nor any of their employees makes any warranty, expressed or implied, or assumes any legal liability or responsibility for the accuracy, completeness, or usefulness of any information, apparatus, product, or process disclosed, or represents that its use would not infringe privately owned rights. Reference herein to any specific commercial product, process, or service by trade name, mark, manufacturer, or otherwise, does not necessarily constitute or imply its endorsement, recommendation, or favoring

by the United States Government or any agency thereof or any other sponsor. Results reported in the LLE Review should not be taken as necessarily final results as they represent active research. The views and opinions of authors expressed herein do not necessarily state or reflect those of any of the above sponsoring entities.

The work described in this volume includes current research at the Laboratory for Laser Energetics, which is supported by New York State Energy Research and Development Authority, the University of Rochester, the U.S. Department of Energy Office of Inertial Confinement Fusion under Cooperative Agreement No. DE-NA0001944, and other agencies.

Printed in the United States of America
Available from
National Technical Information Services
U.S. Department of Commerce
5285 Port Royal Road
Springfield, VA 22161
www.ntis.gov

For questions or comments, contact Matthew Barczys, Editor, Laboratory for Laser Energetics, 250 East River Road, Rochester, NY 14623-1299, (585) 273-3732.

Worldwide-Web Home Page: <http://www.lle.rochester.edu/>
(Color online)

LLE Review

Quarterly Report



Contents

In Brief	iii
Method to Measure Young's Modulus and Damping of Fibers at Cryogenic Temperatures	103
Self-Generated Magnetic Fields in Direct- Drive–Implosion Experiments	110
Absolute Calibration of the OMEGA Streaked Optical Pyrometer for Laser-Driven Shock Waves	122
Multibeam Two-Plasmon Decay in Three Dimensions: Thresholds and Saturation.....	129
Near-Ultraviolet Absorption Annealing in HfO ₂ Thin Films Subjected to Continuous-Wave Laser Irradiation	135
Static and Optical Properties of Warm Dense Polystyrene Along the Principal Hugoniot	142
Fabrication of a Continuous-Enfolded Grating by Ion-Beam–Sputter Deposition.....	148
Publications and Conference Presentations	

In Brief

This volume of the LLE Review, covering January–March 2014, features “Method to Measure Young’s Modulus and Damping of Fibers at Cryogenic Temperatures” by B. S. Rice, L. D. Lund, J. Ulreich, and M. J. Shoup III (LLE); and J. Quinzi (Clarkson University). This article (p. 103) reports on a novel experimental method that is used to measure key physical properties for fibers used to mount cryogenic implosion targets. Young’s modulus and the critical damping ratio of such fibers, at temperatures from 295 K to 20 K, are needed to design stable targets that are required for high-yield implosions, but these property values do not exist in the literature. The method described makes it possible to accurately measure the properties of interest for fiber diameters as small as 12 μm at ~ 20 K; measurements are reported for fibers made of the following materials: NicalonTM ceramic grade [silicon carbide (SiC)], Zylon[®]HM {poly[p-phenylene-2,6-benzobisoxazole] (PBO)}, M5 {dimidazo-pyridinylene [dihydroxy] phenylene (PIPD)}, and polyimide. Significant changes are seen in Young’s modulus for the three polymeric fibers with respect to temperature, while Young’s modulus is relatively invariant to temperature for the ceramic fiber.

Additional highlights of research presented in this issue include the following:

- I. V. Igumenshchev, P. M. Nilson, and V. N. Goncharov (LLE); and A. B. Zylstra, C. K. Li, and R. D. Petrasso (Plasma Science and Fusion Center, MIT) employ radiography with ~ 10 - to 50-MeV protons to investigate electric and self-generated magnetic fields in direct-drive–implosion experiments at the Omega Laser Facility (p. 110). The experiments used plastic-shell targets with imposed surface defects (glue spots, wires, and mount stalks) that enhance self-generated fields. The fields were measured during the 1-ns laser drive and the proton radiographs show multiple ring-like structures produced by $\sim 10^7$ -V/cm electric fields as well as fine structures from surface defects, indicating self-generated fields up to ~ 3 MG. These electric and magnetic fields show good agreement with two-dimensional magnetohydrodynamic simulations when the latter include the $\nabla T_e \times \nabla n_e$ source, Nernst convection, and anisotropic resistivity. The simulations predict that self-generated fields affect heat fluxes in the conduction zone and, through this, affect the growth of local perturbations.
- M. C. Gregor, R. Boni, A. Sorce, C. A. McCoy, and T. R. Boehly (LLE); D. D. Meyerhofer (LLE and Departments of Mechanical Engineering and Physics and Astronomy, University of Rochester); M. Millot (University of California, Berkeley); and P. M. Celliers and J. H. Eggert (LLNL) describe an absolute calibration of the optical response of the streaked optical pyrometer on the OMEGA Laser System using a NIST–traceable tungsten-filament lamp (p. 122). High-energy-density–physics (HEDP) experiments often use optical pyrometry to measure the temperatures of compressed materials. Laser-driven HEDP experiments typically have time scales of tens of picoseconds, requiring the use of a streak camera, which complicates the already formidable task of absolute calibration. The article reports a simple closed-form equation for the brightness temperature as a function of streak-camera intensity derived from this calibration. Error estimates indicate that brightness temperature can be inferred to a precision of $\sim 7\%$ for ~ 5 -eV shocks.

- J. Zhang, J. F. Myatt, and A. V. Maximov (LLE and Department of Mechanical Engineering, University of Rochester); H. X. Vu (Electrical and Computer Engineering Department, University of California, San Diego); D. F. DuBois (LANL and Lodestar Research Corporation); D. A. Russell (Lodestar Research Corporation); and R. W. Short (LLE) report on the determination of linear stability for multiple coherent laser beams with respect to the two-plasmon–decay instability in an inhomogeneous plasma in three dimensions (p. 129). Cooperation between beams leads to absolute instability of long-wavelength decays, while shorter-wavelength shared waves are shown to saturate convectively. Nonlinear calculations using a three-dimensional extended Zakharov model show that Langmuir turbulence created by the absolute instability modifies the convective saturation of the shorter-wavelength modes, which are seen to dominate at late times.
- S. Papernov, A. A. Kozlov, J. B. Oliver, T. J. Kessler, and A. Shvydky (LLE); and B. Marozas (Cornell University) study the modification of the near-UV absorption of HfO₂ monolayer films subjected to irradiation by continuous-wave (cw) near-UV laser light (p. 135). Hafnium oxide is the most frequently used high-index material in multilayer thin-film coatings for high-power laser applications, and absorption in this high-index material is known to be responsible for nanosecond-pulse laser-damage initiation in multilayers. Irradiation by 355-nm or 351-nm laser light, focused to produce power densities of $\sim 100 \text{ kW/cm}^2$, is found to reduce absorption by up to 70% in the areas subjected to irradiation. Absorption maps generated by photothermal heterodyne imaging confirm the permanent character of the observed effect. Nanosecond-pulse, 351-nm and 600-fs, 1053-nm laser-damage tests performed on these cw laser–irradiated areas confirm a reduction of absorption by measuring up-to-25%-higher damage thresholds.
- S. X. Hu, and T. R. Boehly (LLE); and L. A. Collins (LANL) investigate the equation of state (EOS) and optical reflectivity of shock-compressed polystyrene (CH), a common ablator material for inertial confinement fusion targets, up to the unprecedented high pressure of 62 Mbar along the principal Hugoniot (p. 142). The results from a first-principles quantum molecular dynamics (QMD) method are compared with existing experimental measurements as well as the *SESAME* EOS model. The predicted pressure/temperature and optical reflectivity of shocked CH from QMD calculations agree well with experiments for pressures below 10 Mbar; while above 10 Mbar, the QMD-predicted polystyrene is stiffer than the *SESAME* model prediction.
- J. B. Oliver, T. J. Kessler, B. Charles, and C. Smith (LLE) demonstrate the utility of a new collimated ion-beam–sputtering process to conformally deposit a multilayer reflector over the surface relief of a sinusoidal diffraction grating (p. 148). The deposition of a corrugated multilayer reflector on a sinusoidal diffraction-grating surface is attractive for high-laser-damage-threshold applications, with each layer acting as a diffractive element that contributes to the overall diffraction efficiency of the component. By depositing hafnia and silica dielectric layers to enhance the reflectance of a silver film on a 1740-lines/mm sinusoidal grating, a diffraction efficiency of 93% has been achieved for *p*-polarized light incident from the air surface. A 1-on-1 laser-damage threshold of $2.66 \pm 0.15 \text{ J/cm}^2$ has been attained at 1053-nm, 65° incidence with a 10-ps pulse.

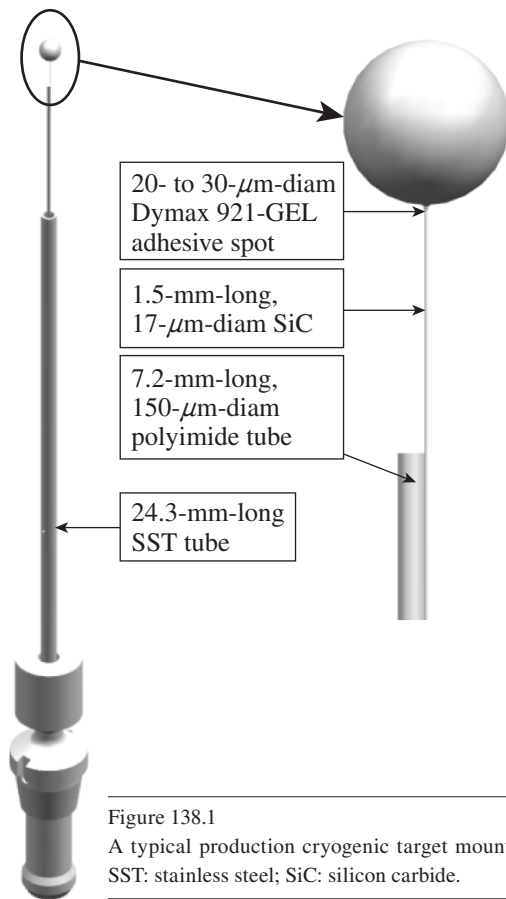
Matthew Barczys
Editor

Method to Measure Young's Modulus and Damping of Fibers at Cryogenic Temperatures

Introduction

The direct-drive laser approach to inertial confinement fusion (ICF) at the Laboratory for Laser Energetics (LLE) involves the use of high-power laser beams to uniformly compress a target capsule filled with hydrogen isotopes in a spherically symmetric implosion. The use of cryogenic (cryo) targets, filled with fuel and cooled to form an ice layer at ~ 20 K on the capsule's inner surface, results in higher fuel densities and, therefore, higher yields.¹

A typical production cryogenic target assembly is shown in Fig. 138.1. The target shell's outer diameter is ~ 875 μm and,



G10052JR

depending on ice thickness, has a filled mass of ~ 55 μg . The design of cryogenic targets must meet the stringent stability requirement of remaining within 10 μm of target chamber center (TCC) at the time of the shot. Target position is a superposition of static alignment and vibration caused by the retraction of the thermal shrouds that maintain the temperature of the target prior to a shot. When the target offset with respect to TCC is increased, a compression asymmetry is introduced, resulting in a reduction of observed neutron yield.²

Target mount assemblies must be designed with a fundamental mode of >300 Hz at ~ 20 K so that the capsule is minimally excited by the impulse created by the aforementioned shroud retraction. Designing a target mount with a specific natural frequency and transmissibility requires accurate values for Young's modulus and the critical damping ratio at cryogenic temperatures. Data for these material properties at cryogenic temperatures are not available in the literature for the materials of choice in target mount design. The materials of interest for this study are NicalonTM ceramic grade [silicon carbide (SiC)] (Ref. 3), Zylon[®]HM {poly[p-phenylene-2,6-benzobisoxazole] (PBO)} (Ref. 4), M5 {diimidazo-pyridinylene [dihydroxy] phenylene (PIPD)} (Ref. 5), and polyimide.⁶ Table 138.I lists the room-temperature values of Young's modulus taken from the literature for these materials of interest.

The method used in this study involves exciting a target mounted on a fiber of each of these materials over a range of temperatures from ~ 295 K to ~ 20 K. An SiC test target assembly is shown in Fig. 138.2. The experimental setup records the displacement of the target capsule's centroid, caused by an impulse load, with respect to time. From this data, the modulus and damping ratio can be calculated over a range of temperatures. Similar methods have been used to measure Young's modulus in other studies;⁷ however, these tests have not included fiber sample shapes or the materials of interest in this study.

Dynamic mechanical analysis (DMA) is another viable method used to find these parameters; however, the results

Table 138.I: Room-temperature material properties of test target mount materials from the literature.

	Material Form	Density (kg/m ³)	Young's Modulus (GPa)	Outside Diameter (μm)	Inside Diameter (μm)	Active Length of Fiber/Tube (mm)
Nicalon™ (Ref. 3)	fiber	2550	210	17	N/A	2.0
Zylon® HM (Ref. 4)	fiber	1560	270	12	N/A	1.3
M5 (Ref. 5)	fiber	1700	330	12	N/A	1.55
Polyimide (Ref. 6)	fiber	1430	2.5	168	122	7.62
304 Stainless	tube	8000	193	711	483	6.74
Dymax 921-GEL (Ref. 8)	adhesive	1000	2.2	N/A	N/A	N/A
CD strong plasma plastic (Ref. 9)	hollow sphere	1000	2.4	875	827	N/A

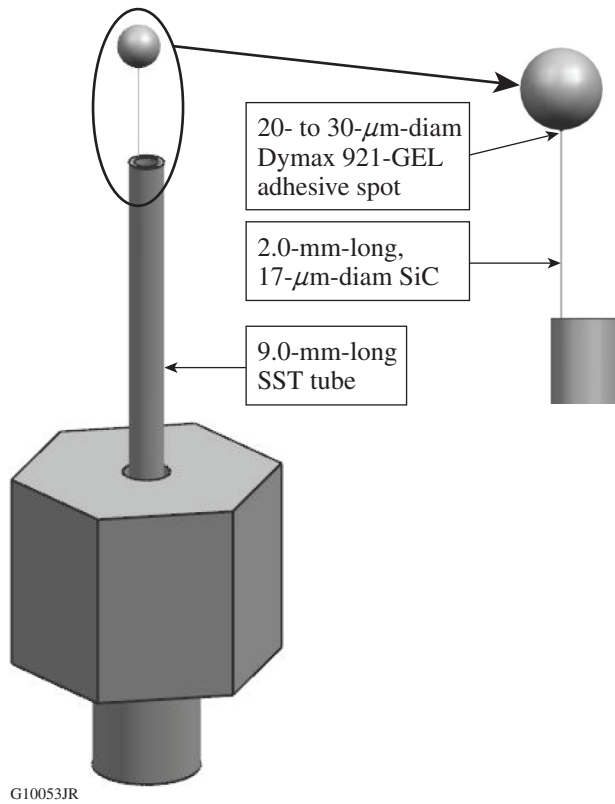


Figure 138.2
A SiC test target assembly used to measure Young's modulus and damping ratio.

are extremely sensitive to the setup and test procedures when measuring fibers <math><20 \mu\text{m}</math> in diameter. In addition, it is not possible to reach temperatures below $\sim 100\text{ K}$ (Ref. 10) with the equipment currently available. The method used here demonstrates that these properties can be accurately measured for fiber diameters as small as $12 \mu\text{m}$ at $\sim 20\text{ K}$. Targets with an $\sim 5\text{-}\mu\text{m}$ -diam carbon support have been manufactured at LLE. An extension of this method to these fibers should not present any unique challenges.

Experimental Methods

The Montana Instruments Cryostation¹¹ provides a selectable isothermal environment, from $\sim 295\text{ K}$ down to $\sim 20\text{ K}$, to conduct vibration tests on sample targets. The test setup is shown in Fig. 138.3. A target capsule without fuel is supported by a fiber of the material of interest and cooled in a helium environment to the desired test temperature. Figure 138.4 shows a test target mounted to the internal cryostation support structure. The entire support structure and target are shrouded in helium to maintain an isothermal environment among the support structure, target temperature sensor, and target assembly. The Montana Instruments Cryostation is designed to minimize steady-state target vibrations caused by the presence of its cold-head [$<25\text{-nm rms}$ (root-mean-square) background vibration]. The test target is excited by an impulse from a modal hammer hit on the body of the cryostation at a given temperature set point. The cryostation's low background vibration contributes to a high signal-to-noise ratio of the target's response to the applied impulse.

Two high-speed cameras with perpendicular viewing angles capture video of target vibrations at a sampling rate of 2000 frames per second. Post-processing software is used to record the displacement of the centroid of the target capsule in each frame, resulting in a displacement (along the x and y axes) versus time data set. Test targets were designed to have a fundamental frequency, at room temperature, of $\sim 3\times$ lower than the Nyquist frequency of the measurement system. The modulus of the fiber is calculated from the fundamental frequency of the target assembly, and damping is calculated from the logarithmic decay of the waveform in the time domain.

Modal hammer hits are aligned with the y axis, and target vibration data are recorded along the x and y axes by using both cameras. A typical vibration response to an impulse aligned

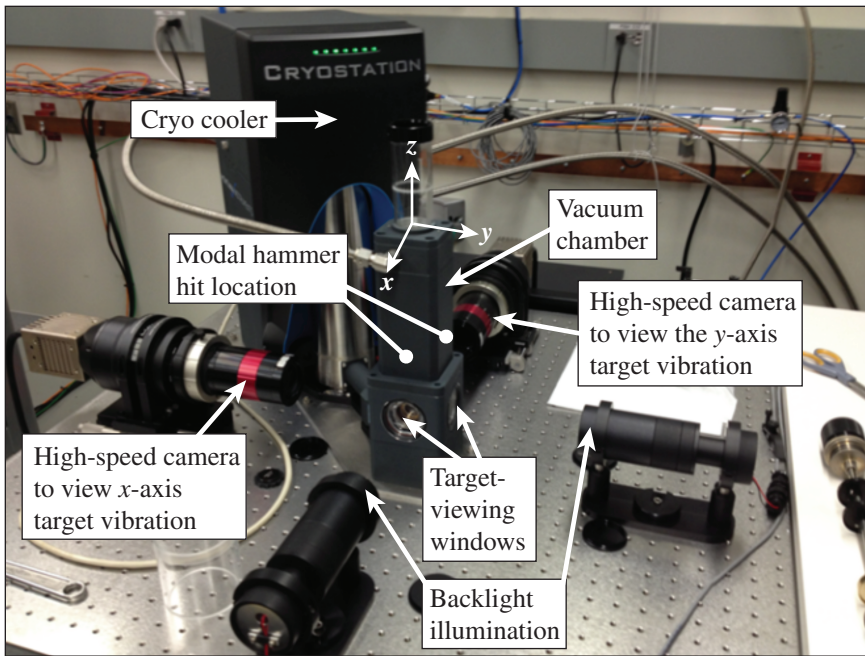
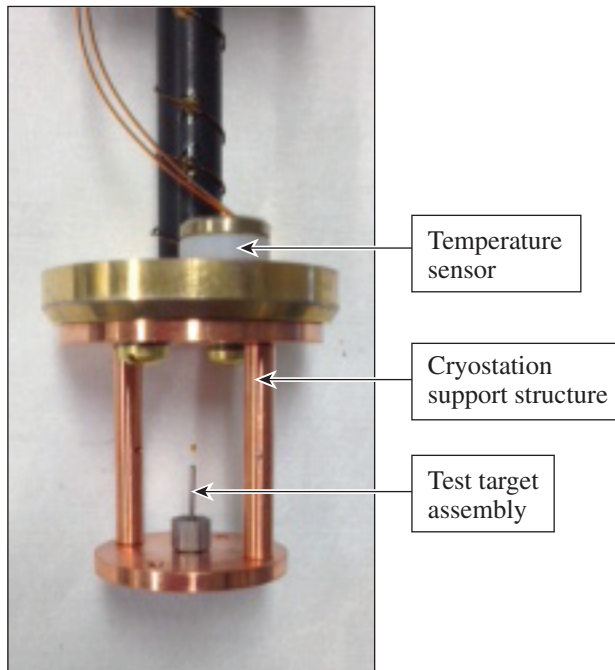


Figure 138.3
Test setup used in this study.

G10054JR



G10055JR

Figure 138.4
Image of a test target mounted to the internal cryostation support structure.

with the y axis is shown in Fig. 138.5 for a SiC fiber test target at 20 K. Damping is measured by the rate of vibration decay in the time domain [Fig. 138.5(a)]. The modulus of the fiber is calculated based on the fundamental vibration mode along the y axis [Fig. 138.5(b)]. The x-axis vibration amplitude is much

lower than the y-axis amplitude since the impulse is directed along the y axis. The x- and y-axes' fundamental modes are 283 Hz and 292 Hz, respectively. The difference is likely due to the fact that the fiber cross section is not perfectly circular. A subsequent impulse aligned with the x axis confirmed that the x-axis fundamental mode is 283 Hz.

Theory

The following equations describe the main theoretical concept of this experimental method: that the fundamental frequency of the test targets can be used to estimate Young's modulus. The natural frequency (f_n) of a cantilevered beam supporting a point mass at its end is proportional to the square root of its modulus (E):¹²

$$f_n = \frac{1}{2\pi} \left[\frac{3EI}{L^3 (M + 0.24 M_b)} \right]^{1/2}, \quad (1)$$

where I is the beam's second area moment of inertia, L is the length of the cantilever beam, M is the point mass supported by the free end of the beam, and M_b is the fiber mass.

Solving Eq. (1) for E yields

$$E = \frac{L^3 (M + 0.24 M_b) (2\pi f_n)^2}{3I}. \quad (2)$$

Using Eq. (2), the modulus can be estimated based on the measured fundamental mode of a cantilever beam structure.

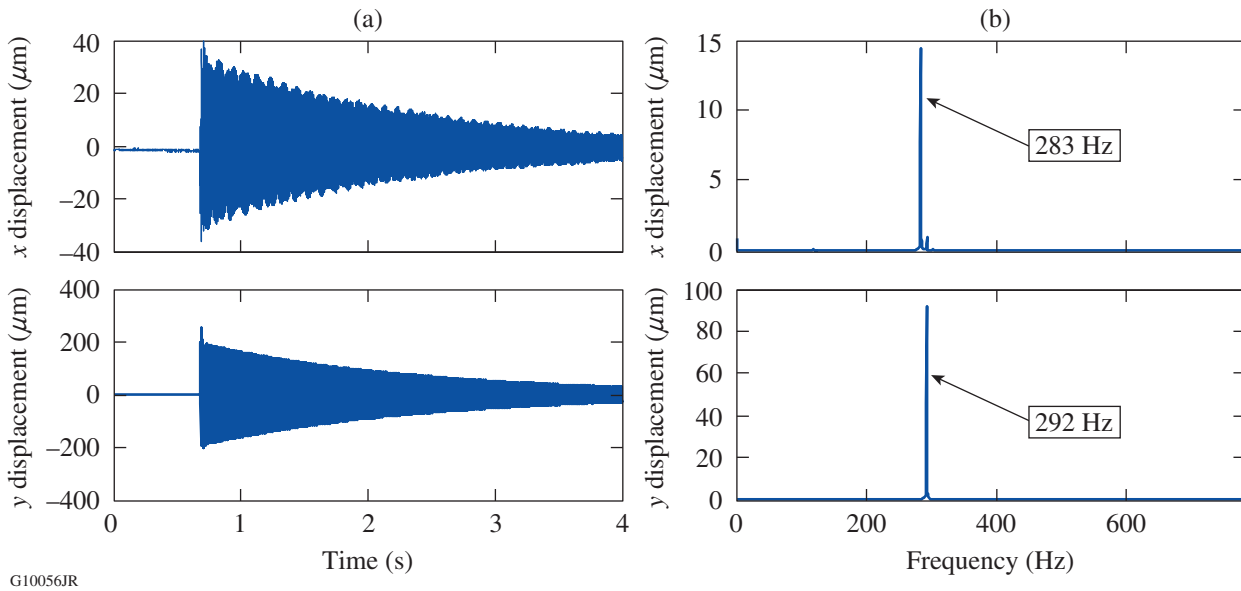


Figure 138.5

Typical target vibration response data collected in this study for a Niclon™ fiber test. In this case (a) shows target vibration with respect to time and (b) shows the fast Fourier transform (FFT) of target vibration.

As a result of the nature of accounting for only one degree of freedom, this equation does not account for the moment caused by the offset of the point mass at the end of the fiber and the stiffness of the capsule, glue joint, and stainless-steel support tube. Finite element (FE) models are used to account for the additional flexibilities of the studied test target assemblies.

An ANSYS™ one-dimensional (1-D) FE model (beam elements) was used to compute the fundamental mode of each test setup. The target shell was treated as rigid, and its mass and rotational inertia were included using a point mass element. A rigid link, from the end of the fiber to the target's centroid, accounts for the offset of the target's center of gravity. Results from these models show that because of its large cross section relative to the test fiber, the stainless-steel tube's effect on the resulting fundamental frequency is negligible (~0-Hz change) and can be treated as rigid.

An ANSYS™ three-dimensional (3-D) FE model (solid elements) was then created to investigate how the stiffness of the glue joint that connects the target capsule to the fiber and the stiffness of the capsule affect the fundamental frequency of the test target assembly. Figure 138.6 shows the model's mesh, including a detailed view of the glue spot. This model shows that increasing the room-temperature value of Young's modulus of the glue and target capsule by a factor of 10—much greater

than it would experience if cooled down to ~20 K—does not significantly change the fundamental frequency (<3-Hz change) of the system (see columns 3 and 4 of Table 138.II).

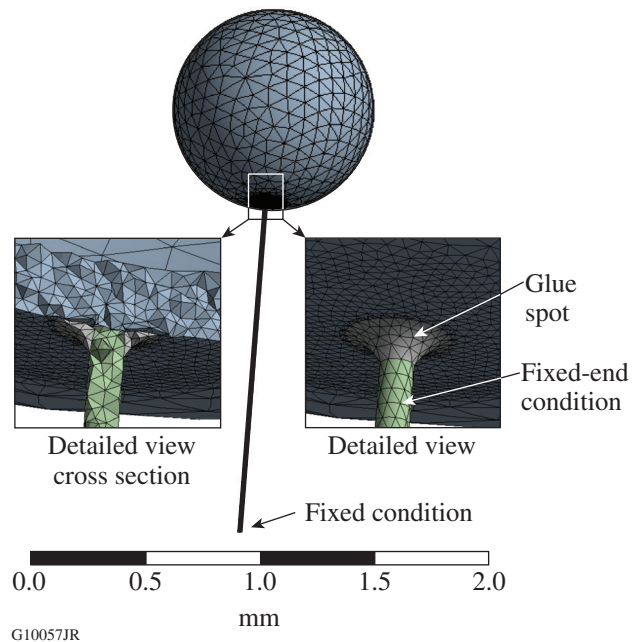


Figure 138.6

Three-dimensional finite element (FE) model mesh with details of the glue spot.

Table 138.II: Comparison of finite element (FE) results and test data.

1	First Natural Frequency				Young's Modulus		Fiber Dimensional Change to Match Literature Values	
	2	3	4	5	6	7	8	9
Fiber material	1-D model (Hz)	3-D model (Hz)	3-D model 10× stiffer (Hz)	Test at 295 K (Hz)	Predicted E at 295 K for the 3-D FE model (GPa)	Literature E at 295 K (GPa)	Delta diameter to match literature (μm)	Delta length to match literature (μm)
Nicalon™	287	280	282	288	222	210	0.2	-40
Zylon® HM	271	261	264	241	230	270	-0.4	90
M5	244	233	236	206	258	330	-0.7	150
Polyimide	363	361*	361*	370	2.6	2.5	2.0	-80

*Glue was not included in this model.

Based on the FE models, the stiffness of the stainless-steel tube, glue spot, and target capsule has a minimal effect on the test target's fundamental frequency. Therefore, it can be stated that any change in the test target's fundamental mode as a function of temperature is a result of a change in only the test fiber's modulus.

Columns 3 and 5 of Table 138.II compare 3-D FE model estimates of the test targets' fundamental frequency at room temperature [using modulus values (column 7) from the literature] with test results at room temperature. Column 6 of Table 138.II lists the values of Young's modulus of the test fiber that are required for the 3-D FE model to match test results. Note that the predicted value of the modulus can vary significantly from what is published in literature, especially for Zylon®HM (230 versus 270 GPa) and M5 (258 versus 330 GPa). Columns 8 and 9 provide insight into two possible causes. Fiber diameters used in this study are estimated from microscope images with a 200× magnification. Table 138.I lists the diameters of tested fibers; both Zylon®HM and M5 have a nominal diameter of ~12 μm . Column 8 of Table 138.II lists the change in fiber diameter required for the 3-D FE model to match the fundamental frequency test results. The inferred diameter differences are less than can be resolved by the fiber-diameter measurement technique used here. In addition, if the fiber diameter is left at its nominal value, column 9 lists the change in fiber length required for the 3-D FE model to match the fundamental frequency test results. The sensitivity of the fundamental mode to uncertainties in fiber diameter or length indicates that it is not possible to obtain accurate absolute measurements of Young's modulus with this experimental technique.

However, if an accurate measurement of a test fiber's Young's modulus is available at one test temperature (room temperature in this article) and fundamental frequencies have been measured at multiple temperatures, additional values of the modulus at the measured temperatures can be calculated. Equation (2) shows that for a cantilever beam of constant cross section and modulus, the modulus is proportional to the fundamental frequency squared. Assuming the test fiber's modulus and its test target's fundamental frequency are known at room temperature, the modulus at a different temperature is computed as follows:

$$E^T = E^{RT} \left(\frac{f_n^T}{f_n^{RT}} \right)^2, \tag{3}$$

where E^T is the estimated Young's modulus, E^{RT} is the measured Young's modulus at room temperature (RT), f_n^T is the measured fundamental frequency at temperature of interest, and f_n^{RT} is the measured fundamental frequency at room temperature.

Calculations

As stated in **Experimental Methods** (p. 104), data from the high-speed camera are post-processed, yielding a vibration waveform of the target capsule's centroid displacement. A fast Fourier transform (FFT) of this waveform gives the fundamental mode of the test fiber. Equation (3) is used to compute Young's modulus as a function of temperature. The logarithmic decrement (rate of decay of free vibration) is used to measure the critical damping ratio of the test fiber:¹³

$$\zeta = \frac{\ln(x_1/x_2)}{2\pi N}, \quad (4)$$

where x_1 and x_2 are the magnitudes of two peaks in the time domain and N is the number of cycles between these peaks.

Results

Figure 138.7(a) shows the minimum, equilibrium, and maximum displacements of an actual M5 target assembly vibrating at 20 K. The top of the stainless-steel tube in the images is a fixed reference point (i.e., it does not move). Figure 138.7(b) shows the corresponding images of a FE representation of an M5 target assembly vibrating at 20 K. The top of the stainless-steel tube is fixed to ground in all six degrees of freedom. The mode shape, as one would expect, is the first bending mode of a cantilever beam.

All four test assemblies were tested at multiple temperatures. At each temperature of interest, the target assembly was excited by a modal hammer hit on the exterior of the cryostat and the resulting target vibrations were recorded. Three measurements at each temperature were recorded. Using Eq. (3) and published values of Young's modulus at room temperature, the modulus at the test temperature was determined. Table 138.III lists the average (of the three measurements taken) fiber modulus at each temperature tested. Using Eq. (4), the critical damping ratio was calculated for each test point. The averages of the three measurements at each temperature are listed in Table 138.IV. Figures 138.8 and 138.9 show plots of the modulus and critical damping ratio, respectively, versus temperature.

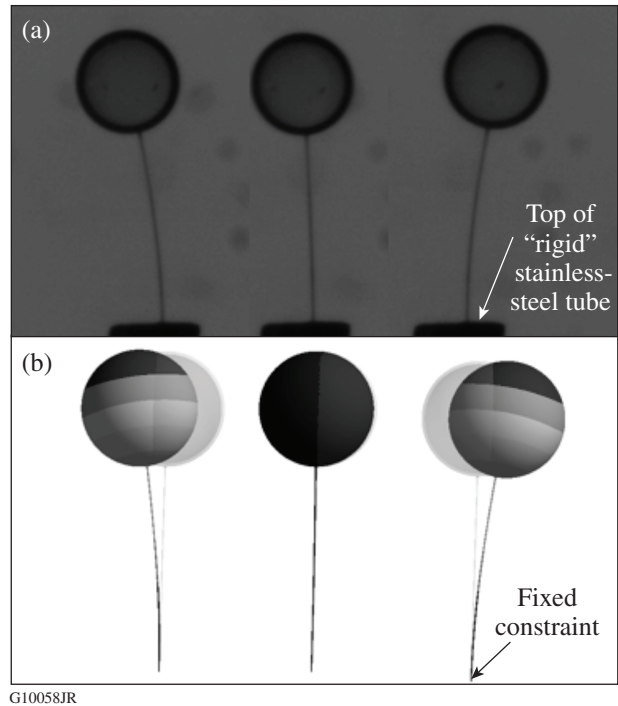


Figure 138.7 Comparison of (a) test image and (b) FE model mode shapes for the M5 target test assembly at 20 K.

In both figures, the markers represent the average value and the error bars represent the range of measurements. (Note that the modulus of polyimide is given by the right ordinate axis in Fig. 138.8.)

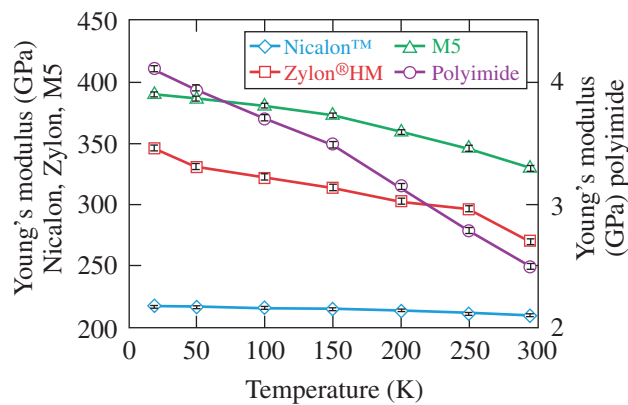
Table 138.III: Experimental values of Young's modulus for each fiber material in GPa measured at various temperatures.

	20 K	50 K	100 K	150 K	200 K	250 K	295 K*
Nicalon™	217	217	216	216	214	212	210
Zylon® HM	346	331	323	314	303	297	270
M5	390	387	381	373	359	346	330
Polyimide	4.1	3.9	3.7	3.5	3.1	2.8	2.5

*The modulus at 295 K taken from literature.³⁻⁶

Table 138.IV: Experimental values of the critical damping ratio for each fiber material in GPa measured at various temperatures.

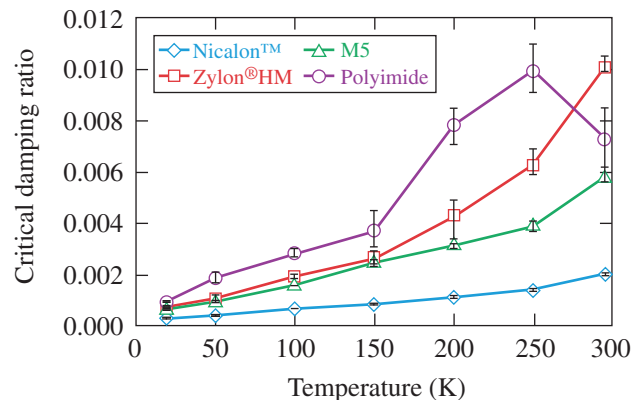
	20 K	50 K	100 K	150 K	200 K	250 K	295 K
Nicalon™	0.00031	0.00046	0.00070	0.00089	0.00113	0.00143	0.00207
Zylon®HM	0.00072	0.00107	0.00197	0.00263	0.00430	0.00630	0.01013
M5	0.00068	0.00099	0.00160	0.00253	0.00313	0.00390	0.00583
Polyimide	0.00096	0.00187	0.00280	0.00370	0.00783	0.00993	0.00730



G10059JR

Figure 138.8

Young's modulus of test fibers as a function of temperature (note the modulus of polyimide is given by the right ordinate axis).



G10060JR

Figure 138.9

Critical damping ratio of test fibers as a function of temperature.

Conclusions

The experimental method used in this article allows one to accurately measure Young's modulus and the critical damping ratio for fiber diameters as small as $12\ \mu\text{m}$ at $\sim 20\ \text{K}$. Significant changes are seen in Young's modulus—stiffer at lower temperatures—for the three polymeric fibers with respect to temperature, while Young's modulus is relatively invariant to temperature for the ceramic fiber. Significant changes in the critical damping ratio—less damping at lower temperatures—are seen for all four fibers with respect to temperature. Below 50 K, all four fibers have a critical damping ratio of less than 0.002. This low-damping level makes it extremely difficult to design low-vibration cryogenic targets because of their high transmissibility.

ACKNOWLEDGMENT

This material is based upon work supported by the Department of Energy National Nuclear Security Administration under Award Number DE-NA0001944, the University of Rochester, and the New York State Energy Research and Development Authority. The support of DOE does not constitute an endorsement by DOE of the views expressed in this article.

REFERENCES

1. P. W. McKenty, T. C. Sangster, M. Alexander, R. Betti, R. S. Craxton, J. A. Delettrez, L. Elasky, R. Epstein, A. Frank, V. Yu. Glebov, V. N. Goncharov, D. R. Harding, S. Jin, J. P. Knauer, R. L. Keck, S. J. Loucks, L. D. Lund, R. L. McCrory, F. J. Marshall, D. D. Meyerhofer, S. P. Regan, P. B. Radha, S. Roberts, W. Seka, S. Skupsky, V. A. Smalyuk, J. M. Soures, K. A. Thorp, M. Wozniak, J. A. Frenje, C. K. Li, R. D. Petrasso, F. H. Séguin, K. A. Fletcher, S. Padalino, C. Freeman, N. Izumi, J. A. Koch, R. A. Lerche, M. J. Moran, T. W. Phillips, G. J. Schmid, and C. Sorce, *Phys. Plasmas* **11**, 2790 (2004).
2. S. X. Hu, V. N. Goncharov, P. B. Radha, J. A. Marozas, S. Skupsky, T. R. Boehly, T. C. Sangster, D. D. Meyerhofer, and R. L. McCrory, *Phys. Plasmas* **17**, 102706 (2010).
3. NICALON™ Ceramic Fiber (Rev. 1/06), COI Ceramics, Inc. (an ATK Space Systems affiliate), Magna, UT 84044 (http://www.coiceramics.com/pdfs/Nicalon_1-17-06.pdf).
4. PBO Fiber Zylon®, Technical Information (Revised 2005.6), Toyobo Co., Ltd. (http://www.toyobo-global.com/seihin/kc/pbo/Technical_Information_2005.pdf), p. 3.
5. M. Afshari, R. Kotek, and P. Chen, in *High Performance Polymers and Engineering Plastics*, edited by V. Mittal (Scrivener Publishing, Salem, MA, 2011), Chap. 9, pp. 269–340.
6. Properties of DuPont VESPEL® Parts, DuPont Engineering Polymers, Newark, DE 19714-6100 (<http://www.craftechind.com/assets/Vespel-Dupont.pdf>), p. 6.
7. W.-H. Chuang *et al.*, *J. Microelectromech. Syst.* **13**, 870 (2004).
8. Dymax® 921-GEL Product Data Sheet (Rev. 06/27/12), Dymax Corporation, Torrington, CT 06790 (<http://www.dymax.com/images/pdf/pds/921-gel.pdf>).
9. A. Nikroo *et al.*, *Fusion Sci. Technol.* **45**, 229 (2004).
10. DMA 8000, PerkinElmer, Waltham, MA 02451 (http://www.perkinelmer.com/CMSResources/Images/44-74431BRO_DMA8000.pdf).
11. Cryostation, Montana Instruments, Bozeman, MT 59715 (<http://www.montanainstruments.com/docs/Cryostation-Catalog.pdf>).
12. R. D. Blevins, *Formulas for Natural Frequency and Mode Shape* (Van Nostrand Reinhold Co., New York, 1979).
13. W. T. Thomson, *Theory of Vibration with Applications*, 2nd ed. (Prentice-Hall, Englewood Cliffs, NJ, 1981).

Self-Generated Magnetic Fields in Direct-Drive–Implosion Experiments

Introduction

Self-generated magnetic fields in laser-produced plasma are developed by the rate $\partial \mathbf{B} / \partial t \sim \nabla T_e \times \nabla n_e$ (Ref. 1), where \mathbf{B} is the magnetic induction and n_e and T_e denote the electron number density and temperature, respectively. Such fields were first observed in experiments using high-power laser beams focused into a gas² and onto a solid target.^{3–5} In perfectly spherical direct-drive implosions,⁶ $\nabla T_e \times \nabla n_e = 0$; therefore, they cannot develop self-generated fields. Fields are expected in real implosions where various perturbations are present, resulting in noncollinear ∇T_e and ∇n_e . Such perturbations may be seeded by nonuniform laser irradiation (e.g., laser imprint), target defects (e.g., surface roughness and surface contaminations), target mounts, and other sources. The strong dependency on temperature makes the field-generation process most efficient in the hottest regions of implosion targets, such as the ablated corona during the laser drive and the target center at the moment of maximum compression. Self-generated magnetic fields cannot approach high, dynamically important values in laser-produced plasma because of the relatively low efficiency source (the energy density of the fields can be only a fraction of the thermal energy density) and typically significant resistive dissipations. Estimates show that the maximum energy density of the fields does not exceed a few percent of the plasma's thermal energy density (i.e., plasma $\beta \gtrsim 100$). Nevertheless, self-generated magnetic fields can alter implosions by suppressing and redirecting heat fluxes.⁷

Heat transport provided by electrons⁸ is an important mechanism in direct-drive implosions that delivers the laser energy deposited near the critical radius R_{cr} , in which $n_e = n_{cr}$, to the ablation front through a conduction zone.⁶ Here n_{cr} is the critical density when the laser frequency equals the plasma frequency. Self-generated magnetic fields in the conduction zone can affect heat fluxes and, therefore, affect target drive, symmetry, and implosion performance. Magnetic fields can considerably change the transport coefficients, such as the electron and thermal conductivity, when the Hall parameter $\omega_e \tau_e \gtrsim 0.3$ (Ref. 9), where $\omega_e = eB/m_e c$; c is the speed of light, m_e and

e are the electron mass and charge, respectively, and τ_e is the electron–ion collision time. Simulations predict that magnetic fields in direct-drive–implosion experiments on the OMEGA laser¹⁰ can grow up to several MG and the Hall parameter can approach ~ 0.3 near the ablation surface. This makes the field effects important in the conditions relevant to inertial confinement fusion (ICF) and requires experimental validation.

Magnetic fields in laser-produced plasma have been measured using coils,² Faraday rotation of optical probe beams,⁵ polarimetry measurements of self-generated laser harmonics,¹¹ and proton radiography.^{12,13} The latter method infers electromagnetic fields by measuring deflection and energy loss of protons while traversing the plasma. Two techniques are typically employed to generate probe protons. In the first technique, a glass microballoon with D^3He fuel is imploded to produce 14.7- and 3-MeV fusion monoenergetic protons.¹³ In the second technique, broad energy spectrum protons with an energy from zero up to several tens of MeV are generated via the target's normal sheath acceleration (TNSA) mechanism, where strong sheath electric fields are produced using a high-intensity ($\sim 10^{19}$ W/cm²) laser interaction with a solid target.¹⁴ Divergent proton flows generated by the TNSA technique have a small virtual source size (about several microns) and good laminarity, providing better spatial and temporal resolutions than those provided by the fusion-based technique.¹⁵

Protons in the range of ~ 10 to 60 MeV are suitable for probing \sim MG magnetic fields and electric fields of $\sim 10^7$ V/cm in experiments with laser-produced plasmas.^{16–18} Experiments on OMEGA using the fusion-based proton backlighter and plastic planar foils driven at an intensity of 10^{14} to 10^{15} W/cm² indicate the development of millimeter-scale magnetic loops¹⁹ localized at the edge of the laser spot, which have been predicted theoretically.²⁰ Rayleigh–Taylor-induced magnetic fields up to about 1 MG have been measured in accelerated foils during the linear growth for 120- μ m-wavelength perturbations.²¹ Planar-foil experiments on OMEGA using TNSA proton backlighters demonstrated about 10- μ m resolution of electromagnetic field

structures. This resolution allows one to investigate small-scale magnetic fields associated with Rayleigh–Taylor spikes and bubbles in laser-accelerated foils.^{22,23}

The first application of proton radiography to direct-drive implosions was demonstrated on the six-beam Vulcan laser.²⁴ Direct-drive-implosion experiments on OMEGA using fusion-based proton backlighters found a complex evolution of electromagnetic structures.²⁵ Imploding capsules develop radial electric fields of $\sim 10^7$ V/cm, reversing directions during the implosion following the evolution of the electron pressure gradient.²⁶ More-recent OMEGA direct-drive-implosion experiments employing TNSA proton backlighters found that proton images at late implosion times (after the end of the laser pulse) are dominated by random filamentary structures formed by small-scale electromagnetic fields in the outer corona.¹⁵ These fields screen the regular fields near the target surface and limit the applicability of the TNSA proton radiography.

This work focuses on measurements and simulations of electromagnetic fields in direct-drive OMEGA implosions during an early implosion time, when the screening effect of the fields in the corona is small. Various surface defects (wires, glue spots, and mount stalks) were imposed to enhance self-generated magnetic fields, which were measured by the TNSA proton backlighter technique. Measured proton radiographs were compared with synthetic radiographs produced using the two-dimensional (2-D) magnetohydrodynamic (MHD) ICF code *DRACO*²⁷ and a proton ray-trace code. The MHD model in *DRACO* is based on the Braginskii model¹ and includes the field source, Nernst convection,^{28,29} anisotropic resistivity, and field-modified heat fluxes.

This article describes the experimental setup and measurements; compares the measurements with *DRACO* simulations; and concludes with a discussion of the results of the experiment and simulations. Details of the MHD model in *DRACO* are presented in the Appendix.

Experiments

Figure 138.10 shows a schematic of the direct-drive-implosion experiment employing the TNSA proton radiography. A 860- μm -diam plastic-shell target was imploded using 60 OMEGA laser beams with a 1-ns square pulse delivering about 28 kJ on target. This corresponds to an on-target intensity of $I \approx 1.2 \times 10^{15}$ W/cm². Standard OMEGA SG4 distributed phase plates,³⁰ polarization smoothing,³¹ and smoothing by spectral dispersion³² were employed to uniformly illuminate the target. The implosion was backlit at a specified time with a proton beam, which was generated by the interaction of a 10-ps, high-intensity ($I \sim 2 \times 10^{19}$ W/cm²) OMEGA EP³³ beam with a 10- μm -thick Au foil. The protons had an energy range of 0 to ~ 60 MeV with an almost exponential distribution. They formed images on radiochromic films, which were arranged in packs that consisted of interleaved filters (Al or Ta) and films. Each film was sensitive to protons from a specific energy interval. More details of the employed radiography technique can be found in Ref. 15.

Four 27- μm -thick plastic-shell (CH) targets having different imposed surface defects were imploded. These targets were supported by mount stalks, each of which was an ~ 80 - μm -diam carbon–silicon fiber glued normally to the target surface (see Fig. 138.11). The glue at the stalk and target joint formed a 120- to 160- μm -diam circular spot on the target surface. These

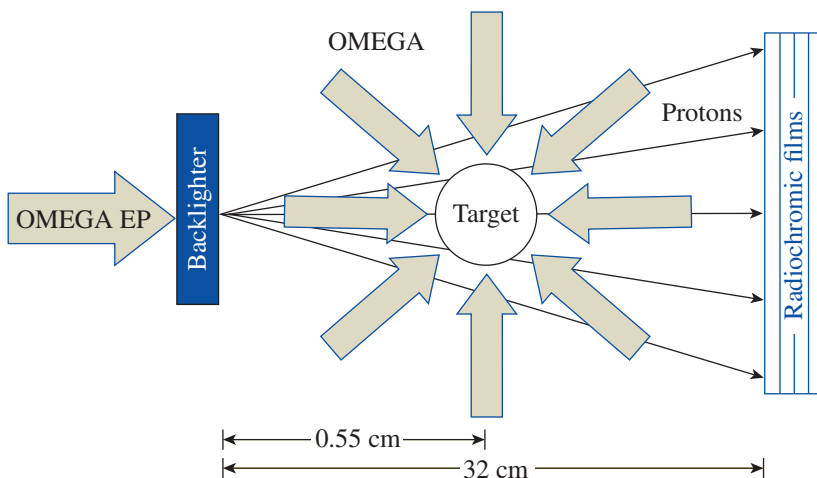


Figure 138.10

Schematic of the experiment. A plastic-shell target was imploded using 60 OMEGA laser beams and backlit by protons having an energy range of 0 to ~ 60 MeV. The protons were generated using a high-intensity OMEGA EP laser beam. Images from different energy protons were obtained using a radiochromic film pack.

glue spots and stalks introduced perturbations that were the source of electromagnetic fields. A piece of 20- μm -diam Cu wire was glued to the surface of three of the targets. Each wire encircled the target, covering half of the equator. These wires were located on the targets' hemispheres, which faced either the proton backlighter (source) or film pack (detector). One target had a 50- μm -diam glue spot located on the hemisphere, facing the detector. Figures 138.11(a) and 138.11(b) show pre-shot images of the targets with the wire and glue spot, respectively. The stalk mount forms a 42° angle with the imaging axis.

Figure 138.12 shows proton radiographs of the implosion targets from film #9 of the packs. These films are primarily sensitive to 36.8-MeV protons.¹⁵ The target center is projected in the center of the radiographs. The evolution times in Figs. 138.12(a)–138.12(d) are $t = 300, 525, 770,$ and 770 ps, respectively, where $t = 0$ corresponds to the beginning of the laser pulse. This timing was estimated by accounting for the proton time-of-flight delays and has an uncertainty of $\Delta t \approx 5$ ps.

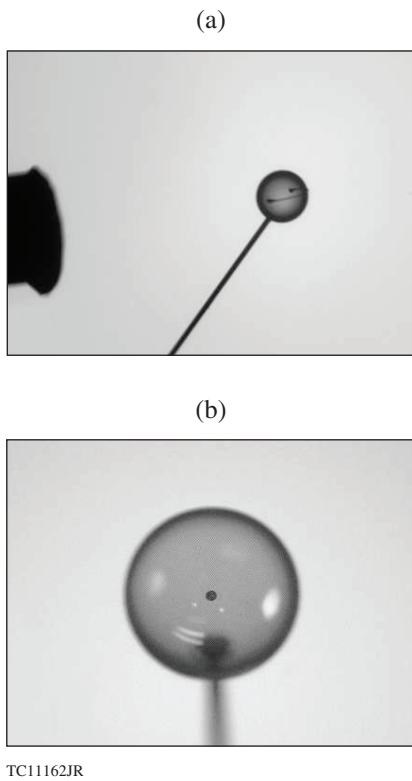


Figure 138.11

Pre-shot images of implosion targets. (a) An 860- μm -diam plastic-shell target on a stalk mount. The stalk axis forms a 42° angle with the imaging axis. A piece of Cu wire, 20 μm in diameter and half the target diameter in length, was glued to the target surface. The dark image on the left is a proton backlighter assembly. (b) Target with a 50- μm -diam glue spot viewed from the proton-detector side.

The targets with the wire on the side facing the detector are shown in Figs. 138.12(a) and 138.12(c), and the target with the wire facing the source is shown in Fig. 138.12(d). The target with the glue spot located on the side facing the detector is shown in Fig. 138.12(b).

The radiographs in Fig. 138.12 reveal multiple ring structures around the targets. Similar structures were reported in previous studies using the fusion-based backlighters.²⁵ The outer dark ring A appears only in Fig. 138.12(a) at the early implosion time $t = 300$ ps, while the white rings B are observed in the early and late time radiographs in Fig. 138.12. The radius of ring B is reduced with time, apparently following the reduction of the radius of the implosion targets. Simulations suggest (see **Simulation Results**, p. 114) that electric fields cause the observed ring structures to form. In particular, ring A is formed because of the fields localized at the front of the expanding corona. This front quickly moves, leaving the field of view of the proton diagnostics; therefore, the ring is not observed at the

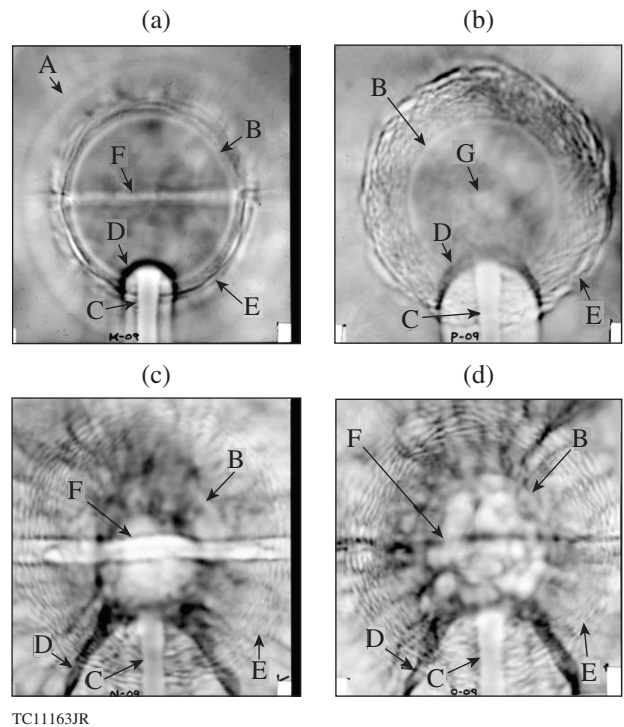


Figure 138.12

Radiographs of implosion targets from film #9 (primarily sensitive to 37-MeV protons). Darker regions correspond to higher fluence. (a) Target with a Cu wire on the side facing the proton detector at $t = 300$ ps (shot 63035). (b) Target with a glue spot on the side facing the proton detector at $t = 525$ ps (shot 63043). [(c) and (d)] Targets with Cu wires on the sides facing the proton detector and source, respectively, at $t = 770$ ps (shots 63037 and 63039, respectively).

later times. Rings B are associated with the critical radius R_{cr} , where n_e and T_e experience significant variations, resulting in large electric fields.

The radiographs in Fig. 138.12 also reveal quasi-spherically distributed ripple structures E observed outside of rings B. These structures consist of many dark and light filaments elongated in the azimuthal direction. The ripple structure in Fig. 138.12(a) is located inside ring A and occupies a relatively narrow radial range. At a later time, in Fig. 138.12(b), this structure increases the radial range and develops a sharp outer edge at $\sim 800 \mu\text{m}$ from target center. At an even later time, in Figs. 138.12(c) and 138.12(d), the structure E is still seen to occupy about the same radial range as in Fig. 138.12(b) but is missing the sharp outer edge.

The white rings B in the radiographs from the same film pack show different diameters, depending on the proton energy. Figure 138.13 illustrates this effect by comparing films #9 and #6 (sensitive to 36.8- and 15.3-MeV protons, respectively) from shot 63035. The diameter of the white ring is reduced by about 15% in film #6 with respect to that in film #9. This reduction is too significant to be explained by the variation of the image magnification factor because of the finite thickness of the film pack (this explains the less-than-1% difference) and by the difference of the evolution time between the films because of the proton time-of-flight difference. A plausible explanation of this effect is a negative charging of the target. The lower-energy protons are more susceptible to deflection by the force from the

charge and form a smaller ring, while the higher-energy protons are less susceptible and form a larger ring. The measured ring diameters can be explained if the target charge $Q \approx -7 \times 10^{10} e$, corresponding to an electric field $\approx 6 \times 10^6 \text{ V/cm}$ at the critical radius. A possible mechanism of this charging is presented in **Discussion and Conclusions**, p. 118.

Features from the stalk mount and related perturbations in the target corona can be seen in the lower part of the radiographs in Fig. 138.12. The vertical features denoted by C are projections of the stalk and do not significantly vary in time. The upper end of the stalk image in Figs. 138.12(a) and 138.12(b) is located inside the white ring B associated with the critical surface. This is because of the stalk inclination with respect to the imaging axis (see Fig. 138.11), so that the stalk end is projected inside the target radius. Electromagnetic fields developed at material interfaces resulting from the interactions of plasmas ablated from the stalk, glue, and target produce variously shaped structures denoted by D. These structures evolve taking bow- and cylinder-like shapes at an earlier time [see Figs. 138.12(a) and 138.12(b)] and cone-like shapes at a later time [see Figs. 138.12(c) and 138.12(d)].

The feature F in Figs. 138.12(a), 138.12(c), and 138.12(d) is an image of the Cu wires and consists of light and dark horizontal lines crossing the target images in the midplane. These lines are formed because of focusing or defocusing protons by electromagnetic fields near the wires. The lines in Figs. 138.12(a) and 138.12(c) are produced by the wires located on the target side facing the proton detector. These lines demonstrate a complicated internal structure, showing tiny dark lines located inside wide light lines. The latter light lines end between the two other dark lines. The observed line structures suggest [and simulations confirm (see **Simulation Results**, p. 114)] that the fields deflect at least a fraction of backlighting protons toward the wire (focusing the beams) and form the interleaved dark and light lines on the detector plane. The width of the line structures increases from Fig. 138.12(a) to 138.12(c), indicating that the fields become stronger or occupy a larger area at a later time. Figure 138.12(d) shows a line structure produced by the wire located on the target side facing the proton source. An apparent dark horizontal line is located a little above the target image's midplane and a less-apparent line just below that plane. The image of the latter line is probably obscured by electromagnetic fields developed in the corona and observed as "cloudy" structures in the central part of Fig. 138.12(d). Simulations suggest (see **Simulation Results**, p. 114) that the line structure in Fig. 138.12(d) is formed by protons deflected from the wire (defocused beams).

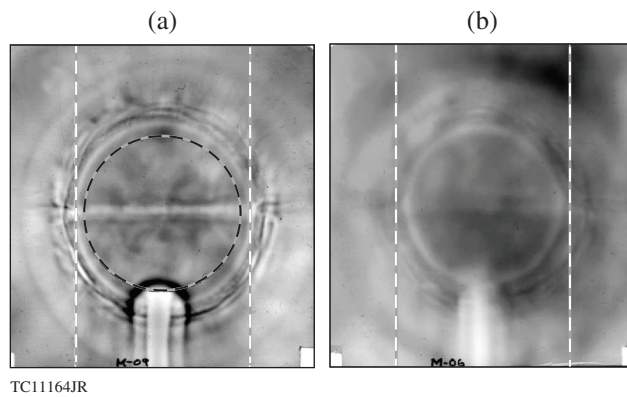


Figure 138.13
Comparison of radiographs from films (a) #9 and (b) #6 for shot 63035. These films are primarily sensitive to 36.8- and 15.3-MeV protons, respectively. The vertical white dashed lines [in (a) and (b)] mark the diameter of the white ring in (a). The diameter of the similar ring in (b) is reduced by about 15%, indicating negative charging of the target. The dashed black circle in (a) shows the projection of the initial target surface (within $\approx 5\%$ accuracy).

Figures 138.12(c) and 138.12(d) allow one to study almost identical plasma and field structures from the wires by probing them with protons from opposite directions. Changing the direction changes the sign of the Lorentz force acting on the protons, whereas the electric force is not changed. Therefore, the differences observed in Figs. 138.12(c) and 138.12(d) can be attributed to only the effects of magnetic fields.

Figure 138.12(b) shows the target with the glue spot on the side facing the detector at $t = 525$ ps. This spot produces the light spot G in the center of the radiograph. The diameter of spot G is about a factor of 2 larger than the projected diameter of the glue spot of an undriven target, indicating the effects of electromagnetic fields. The geometry of deflected proton beams (convergent or divergent) and, accordingly, the sign of the corresponding self-generated magnetic fields around the spot are difficult to determine using only this measurement. Both the convergent and divergent beams can form light spots on radiographs if deflection angles are large enough. Numerical simulations suggest (see the next section) that the light spot is produced by divergent (defocused) proton beams.

Simulation Results

The experiments were simulated using the 2-D hydrodynamic code *DRACO*.²⁷ *DRACO* solves the induction equation in the form based on the Braginskii MHD model.¹

The code includes the effects of magnetic fields on the heat transport: the modified Spitzer flux, cross-gradient heat flux, and heat flux caused by electron currents.¹ The induction equation and field-modified heat flux are described in the **Appendix** (p. 119). The simulations assume the axial symmetry and start from a zero-field condition. Self-generated fields, therefore, develop only the azimuthal component $\mathbf{B} = (0, 0, B_\phi)$.

Measured proton radiographs were compared with synthetic radiographs that were calculated using a proton ray-trace code. The code employs the equation of motion for protons, which includes the effect of magnetic and electric fields,

$$M_p \frac{d\mathbf{V}}{dt} = \frac{e}{c} \mathbf{V} \times \mathbf{B} - \frac{1}{n_e} (\nabla P_e - \mathbf{R}_T), \quad (1)$$

where M_p and \mathbf{V} are the proton mass and velocity, respectively, P_e is the electron pressure, and \mathbf{R}_T is the thermoelectric force (see **Appendix**, p. 119). The first and second terms on the right-hand side of Eq. (1) represent the Lorentz and electric forces, respectively. The calculations assume the same proton backlighting geometry as in the experiment (Fig. 138.10). The proton source is approximated by a monoenergetic point

source. Images are constructed by collecting all protons crossing the detector plane. The change in proton energy caused by interactions with electric fields is small and neglected. The effects of the scattering and stopping of protons caused by elastic and nonelastic collisions with background ions are small and also neglected.²²

Figure 138.14 shows simulation results of the target with a stalk at $t = 770$ ps. This time corresponds to that in Figs. 138.12(c) and 138.12(d). The density distribution in Fig. 138.14(a) shows that the stalk and target shell are compressed by shocks. The shock in the shell has already experienced a breakout, and the shell has moved about $40 \mu\text{m}$ inward from the initial position. The flows ablated from the stalk and glue interact with the spherical outflow from the

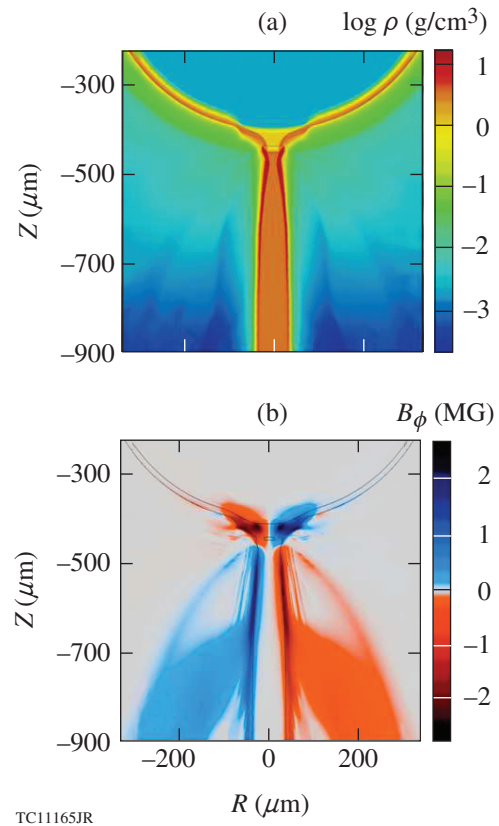


Figure 138.14

Snapshots from axisymmetric *DRACO* simulations of the target with a stalk at $t = 770$ ps. (a) Density distribution. The region around the target and stalk joint is shown. The target center is at $(0, 0)$. (b) Distribution of the magnetic induction B_ϕ . The negative sign of B_ϕ corresponds to magnetic fields directed toward the reader and the positive sign away from the reader. The black contours represent a density of 1.2 g/cm^3 .

target, forming cone-like interfaces between the materials. This produces nonuniform electron density and temperature distributions, which result in the self-generated magnetic fields shown in Fig. 138.14(b). These fields grow to ~ 3 MG and are mainly generated near the ablation and critical surfaces, where the source term ($\sim \nabla T_e \times \nabla n_e$) takes the maximum value. The fields are concentrated near the ablation surfaces and not convected outward by the ablation flows as one can expect in the case of the ideal MHD. This concentration and the absence of the flow convection are caused by the Nernst convection, which compresses the fields toward the ablation surfaces and significantly overcomes the flow convection. The fields around the stalk produce cross-gradient heat fluxes, which are directed outward and convect (by the Nernst convection) several magnetic fields. This explains the concentration of fields around the stalk at $Z \approx -600 \mu\text{m}$ in Fig. 138.14(b). Other magnetic fields that are localized at the material interfaces in the corona form cone-like structures. The field structure around the target with the stalk is schematically illustrated in Fig. 138.15.

Figures 138.16(a)–138.16(c) show synthetic radiographs of the implosion target with the stalk at $t = 300, 525,$ and

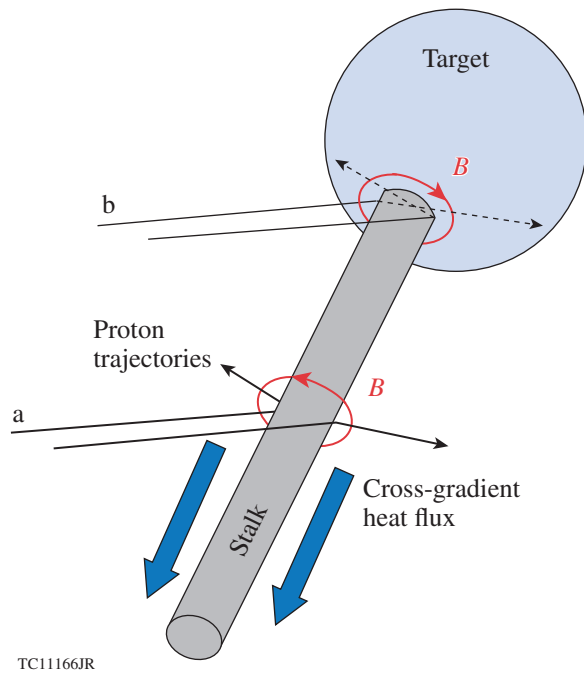


Figure 138.15

Schematic view of self-generated magnetic fields (in red) near the target and stalk joint and around the stalk. Backlighting protons (black lines) are deflected by the fields, causing trajectories “a” to diverge and “b” to converge. The fields around the stalk produce a cross-gradient heat flux, which is directed away from the target.

770 ps, respectively. The center of the target is projected in the center of the radiographs, and the stalk is inclined at the same 42° angle with respect to the imaging axis as in the experiment. Features C and D from the stalk are observed in the lower part of the radiographs. These features closely resemble the similar features of C and D in the measured radiographs in Fig. 138.12. An analysis of the simulations shows that the vertical feature C is formed because of protons deflected by the fields at the ablation surface around the stalk (the trajectories “a” in Fig. 138.15). The fields at the material interfaces in the corona produce the feature D. The change of the measured shapes of these features in time [compare Figs. 138.12(a)–138.12(c) and Figs. 138.16(a)–138.16(c), respectively] is well produced in the simulations.

In Fig. 138.16, features C and D result from protons deflected by magnetic fields while the effects of electric fields are not significant. As an example, the radiograph in Fig. 138.16(d) was calculated without the Lorentz force term in Eq. (1) and does not show these features. Instead, this radiograph reveals the feature H, which is not clearly seen in Fig. 138.16(c) and was developed as a result of electric fields at the standing shock in the plasma ablated from the stalk.

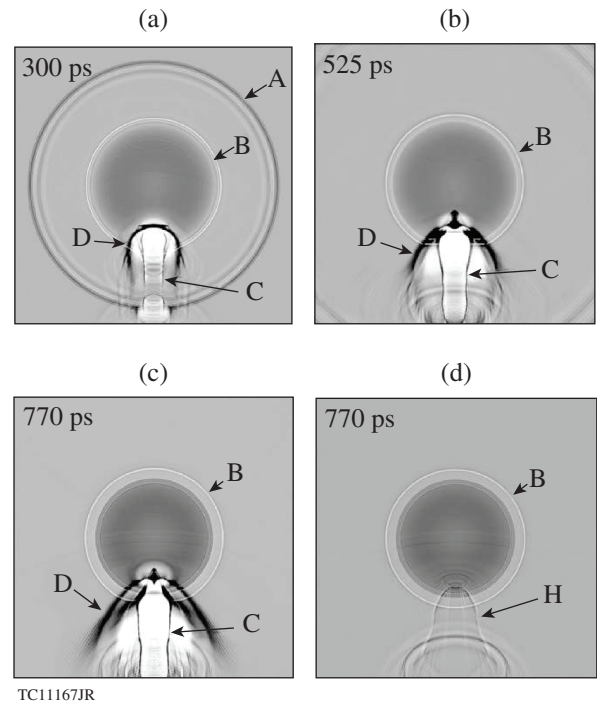


Figure 138.16

Synthetic proton radiographs of the target with a stalk at (a) $t = 300$ ps, (b) 525 ps, and [(c) and (d)] 770 ps. Radiographs (a)–(c) were simulated using both the electric and magnetic terms in Eq. (1); radiograph (d) was simulated using only the electric term.

The radiographs in Fig. 138.16 reveal rings A and B, which are similar to those in the measured radiographs in Fig. 138.12. The simulations suggest that ring A develops because of protons deflected by electric fields at the front of the expanding plasma corona and rings B develop because of protons deflected at the critical surface. Magnetic fields are insignificant here because the corona front and critical surface are almost spherically symmetric, resulting in a small magnetic source.

Figure 138.17(a) shows the radial distribution of the electric force acting on protons in the radial direction from the *DRACO* model shown in Fig. 138.14, but at $t = 300$ ps; Fig. 138.17(b) shows the corresponding distributions of P_e , T_e , and n_e/n_{cr} . The plotted distributions are for the upper (not perturbed by the stalk) hemisphere. The vertical dashed lines 1, 2, and 3 show the location of the ablation, critical, and corona fronts, respectively. The electric force has a negative sign between lines 1 and 2 and a positive sign between lines 2 and 3. As a result, protons flying at the radius range between lines 1 and 2 are deflected toward the target center, whereas protons flying at the range between lines 2 and 3 are deflected outward. This causes the white ring B in Fig. 138.16(a) to appear at the critical surface along with two dark rings: one just inside the white ring in the place of the ablation surface and another, ring A, in the corona front. It should be noted that the MHD model in *DRACO* is inaccurate when the free path of charged particles is larger than the characteristic scale lengths, which follow from the model. This could happen in the corona and, in particular, at the corona's front. Nevertheless, *DRACO* simulations reproduce well the measurements of ring A (Fig. 138.12).

The density [Figs. 138.18(a) and 138.18(c)] and magnetic induction [Figs. 138.18(b) and 138.18(d)] are shown at two

consecutive times, $t = 300$ and 770 ps, from simulations of the target with the Cu wire. The $20\text{-}\mu\text{m}$ -diam wire is located near the equatorial plane. At $t = 300$ ps, the wire has been compressed by the shock, and perturbations have been introduced at the target ablation surface and in the corona [Fig. 138.18(a)]. Self-generated magnetic fields [Fig. 138.18(b)] are localized around the wire and end somewhere between the ablation and critical surfaces because of the Nernst convection. These fields

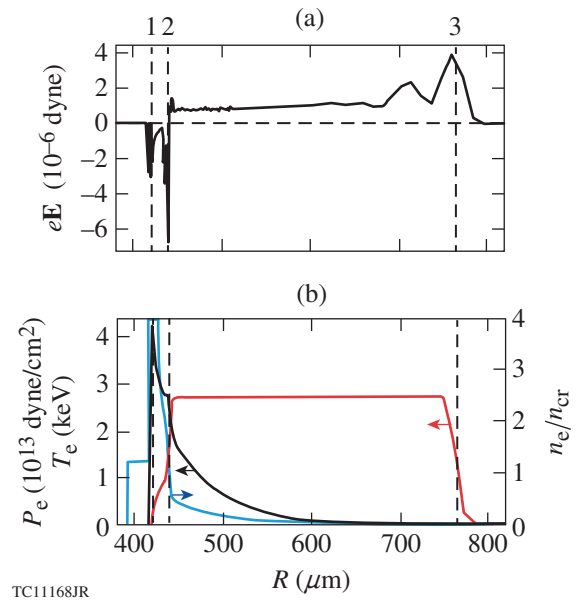


Figure 138.17

Radial profiles of selected quantities from the implosion simulation at $t = 300$ ps. (a) Radial component of the electric force acting on protons, $eE = -(\nabla P_e - \mathbf{R}_T)/n_e$. The vertical dashed lines 1, 2, and 3 indicate the locations of the ablation, critical density, and outer plasma fronts, respectively. (b) Electron pressure (black), number density (blue), and temperature (red).

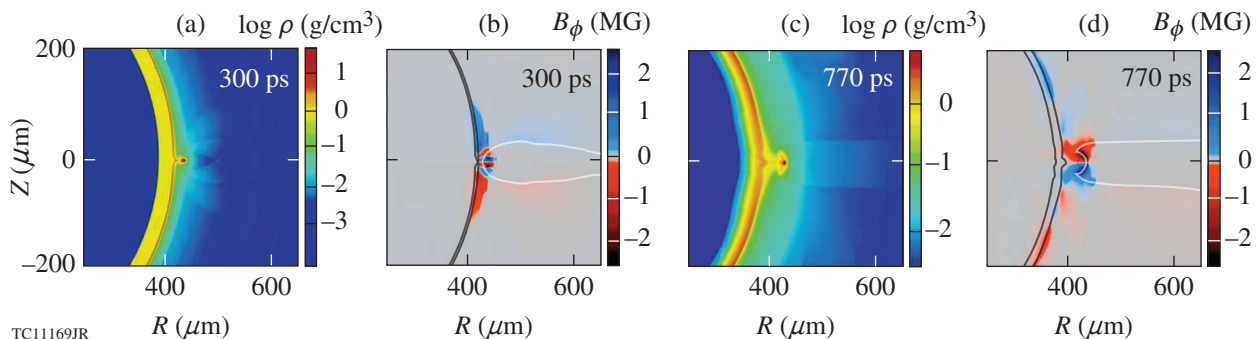


Figure 138.18

Snapshots from axisymmetric *DRACO* simulations of the target with a Cu wire. [(a) and (c)] Distributions of the density at $t = 300$ and 770 ps, respectively. The wire is located near the equatorial plane. Laser light comes from the right. [(b) and (d)] Distributions of B_ϕ at the same moments as in (a) and (c). The black contours represent a density of 1.2 g/cm^3 , and the white contours show the interface between the Cu and CH plasmas in the corona.

grow to ~ 2 MG and change their sign several times in the polar direction. Magnetic fields of small value also develop at the Cu and CH material interface in the corona [the interface is shown by the white line in Fig. 138.18(b)]. At the later time, $t = 770$ ps, the remnant of the wire is located at a larger offset from the shell [Fig. 138.18(c)], and the fields, about 2 MG, are more evenly distributed around the wire and occupy the relatively large volume [Fig. 138.18(d)]. The largest fields at this time end again between the ablation and critical surfaces, which are more radially separated. As in the early time, there are small fields at the material interface in the corona. Note that the fields immediately around the wire change their sign during the evolution [compare Figs. 138.18(b) and 138.18(d)]. Figure 138.19 schematically illustrates the field topology around the wire at $t = 770$ ps.

Synthetic radiographs in Figs. 138.20(a), 138.20(c), and 138.20(d) show the target with the wire at $t = 300$, 770, and 770 ps, respectively. The wire is located on the target side facing the proton detector in Figs. 138.20(a) and 138.20(c) and the source in Fig. 138.20(d). The feature F in the images is from the wire and can be compared with the analogous feature F in the measured radiographs in Fig. 138.12. At $t = 300$ ps, the synthetic image consists of a white line that ends between two dark lines [Fig. 138.20(a)]. This white line is not uniform and includes two tiny dark lines inside of it. A similar, but not identical, line structure was observed in Fig. 138.12(a). The differences between the measured and simulated images could be attributed to the experimental blurring, which can wash out fine structures and was not considered in the ray-trace code. The synthetic image of the wire at $t = 770$ ps in Fig. 138.20(c) reproduces the thin dark line in the middle of the wide light line similar to the one measured [see Fig. 138.12(c)]. This dark line, however, is much clearer in the synthetic image. An analysis of the simulations shows that the white and black lines in Figs. 138.20(a) and 138.20(c) are formed by deflect-

ing (focusing) the protons (which traverse the regions with the fields immediately adjacent to the wire) toward the wire [Fig. 138.19(b)]. When the target is probed by protons from the opposite direction, the proton trajectories are defocused by the fields [Fig. 138.19(a)] forming the two dark lines F in Fig. 138.20(d). The corresponding measured radiograph in Fig. 138.12(d) shows the clear image of only one (upper) dark line, while the other (lower) dark line is represented unclearly, probably because of scattering backlighting protons by electromagnetic fields in the corona.

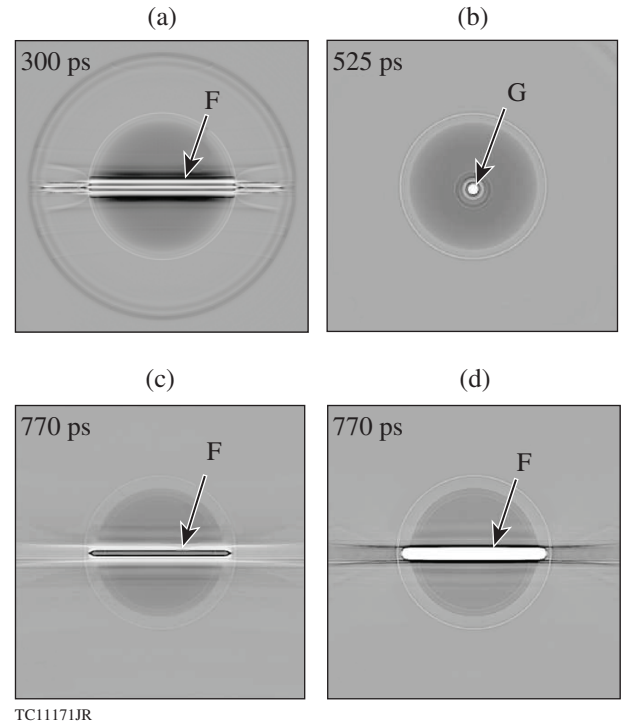


Figure 138.20 Synthetic proton radiographs of the targets with a wire [(a), (c), and (d)] and a glue spot (b). The backlighting geometry corresponds to that for the measured radiographs in Fig. 138.12.

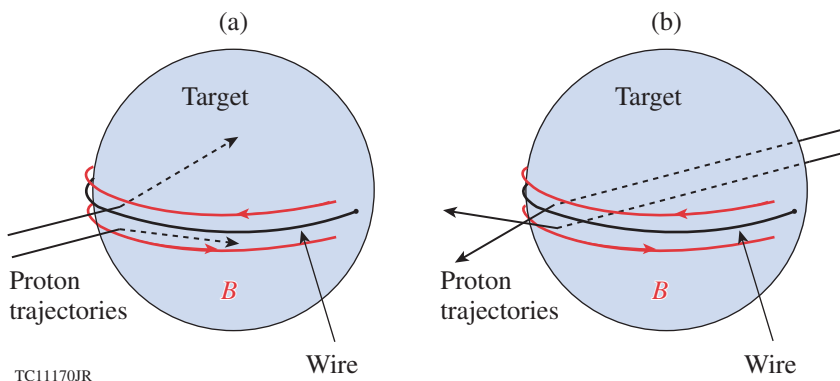


Figure 138.19 Schematic view of self-generated magnetic fields (in red) near the wire. (a) Backlighting protons come from the left (black lines), illustrating the experimental conditions when the wire is located on the target side facing the proton source. The proton trajectories are deflected by the fields and diverge. (b) The proton trajectories coming from the opposite direction (the wire on the side facing the proton detector) converge.

Figure 138.21 shows simulation results of the target with a 50- μm -diam glue spot at $t = 525$ ps. Perturbations introduced by the spot [Fig. 138.21(a)] result in self-generated fields up to ~ 4 MG that are localized at the ablation surface around the spot [Fig. 138.21(b)]. As mentioned earlier, this localization is caused by the Nernst convection. It is worth noting that the field around the spot has the opposite sign to that of the wire in Fig. 138.18(d) and the same sign as the field near the target and stalk joint in Fig. 138.14(b). Figure 138.22 illustrates the topology of the fields around the glue spot.

Figure 138.20(b) shows a synthetic radiograph of the target with the glue spot. The radiograph was calculated assuming the same spot location as in the experiment (facing the detector). The image G of the spot consists of a white circle surrounded by a sequence of fine dark and white rings. The measured radiograph confirms the development of the white

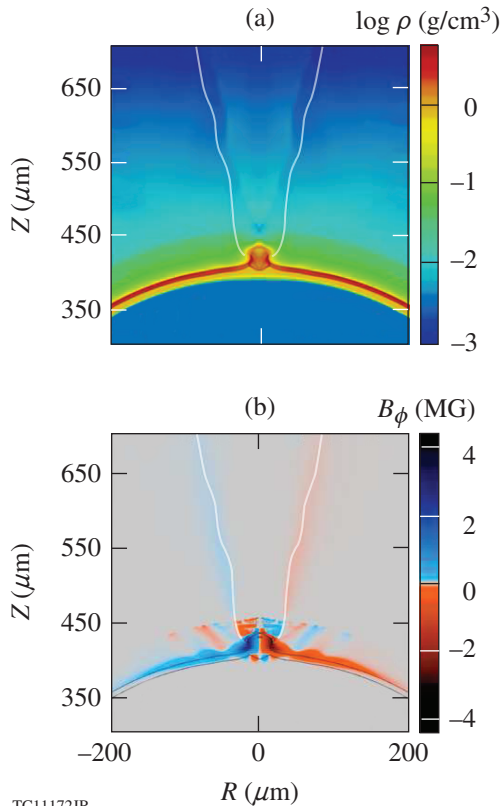


Figure 138.21 Snapshots from axisymmetric *DRACO* simulations of the target with the glue spot at $t = 525$ ps. Distributions of the (a) density and (b) B_ϕ . The glue spot is located at the pole. Laser light comes from the top. The black contours in (b) represent a density of 1.2 g/cm³ and the white contours in (a) and (b) show the interface between the glue and CH plasmas in the corona.

circle showing the light spot in the center of Fig. 138.12(b); however, there is no signature of the ring structures around the spot. The lack of these structures could be a result of either an inaccuracy in modeling or experimental blurring. The origin of the white circle is illustrated in Fig. 138.22, which shows that protons traversing the region near the glue spot are deflected off (defocused), producing a circle of reduced proton fluence on the detector plane.

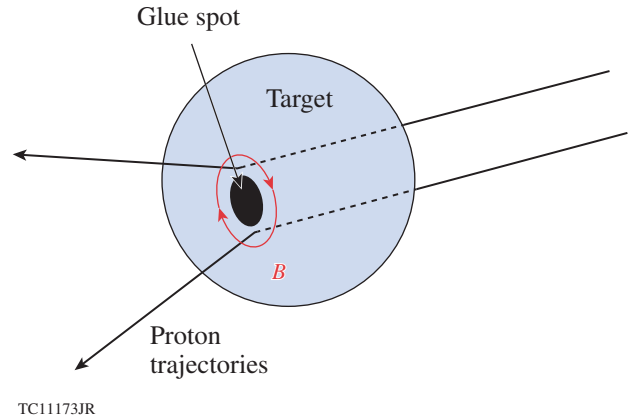


Figure 138.22 Schematic view of self-generated magnetic fields (in red) around the glue spot. The experimental conditions (the spot on the target side facing the proton detector) are illustrated by showing protons coming from the right (black lines). These protons diverge after interacting with the fields.

Discussion and Conclusions

Electric and self-generated magnetic fields have been measured in implosion experiments on the OMEGA laser using plastic-shell targets. The self-generated fields developed as a result of perturbations from the mount stalk and imposing surface defects: Cu wires and glue spots (Fig. 138.11). The electric and magnetic fields were measured using the TNSA radiography, in which a proton beam was produced by employing a high-intensity OMEGA EP laser beam. Good-quality radiographs were obtained using 37-MeV backlighting protons. These radiographs show clear features from the stalk, wire, and glue spot in different times and different backlighting geometries (Fig. 138.12).

Synthetic proton radiographs (Figs. 138.16 and 138.20) were calculated by post-processing 2-D MHD *DRACO* simulations and, when compared with the measured radiographs, demonstrated good agreement. The inclusion of the $\nabla T_e \times \nabla n_e$ source, Nernst convection, and anisotropic resistivity in the induction equation and the field-modified heat fluxes in the electron energy equation is essential to obtaining this agreement. The ring-like features in the measured and synthetic radiographs

(Figs. 138.12, 138.16, and 138.20) are explained by protons deflected by electric fields up to $\sim 10^7$ V/cm at the critical surface (white rings) and the plasma corona front (outer dark rings). The features from the defects (stalks, wires, and glue spots) are developed mostly by protons deflected by magnetic fields up to ~ 3 MG. This was demonstrated by calculating the radiographs with and without magnetic fields (but with electric fields in both cases). The features from the defects disappeared in the calculations without magnetic fields, while the ring-like features were not changed with or without the fields.

The white rings in the radiographs in Figs. 138.12 and 138.13 are explained by scattering protons off at the critical radius by electric fields (Fig. 138.17). An alternative explanation of such rings could be that protons are scattered through Coulomb collisions with ions in the dense shell.²⁵ The TNSA radiography of undriven targets using the lowest-energy protons indeed demonstrated this possibility.¹⁵ Coulomb collisions are unlikely responsible, however, for the observation of the rings in the present experiment for at least two reasons: (1) Trajectories of 37-MeV protons used in the experiment are not significantly affected by Coulomb collisions.²² (2) The measured radius of the white rings is larger than the target radius (see the dashed black circle in Fig. 138.13) and consistent with numerical estimates of the critical radius.

Proton radiographs reveal a reduction in the white-ring radii, which are associated with the target's critical surface, for the lower-energy protons (Fig. 138.13). This reduction can be explained by the negative charging of the target within the critical surface with the charge $Q \approx -7 \times 10^{10} e$. Electrostatic charging of targets has been studied using fusion-based proton radiography²⁵ and measuring energetic (≥ 1 -MeV) fast protons and ions^{34,35} in direct-drive implosions. This charging is likely provided by hot electrons (~ 10 to 100 keV) generated by the two-plasmon-decay (TPD) instability developed near the radius of the quarter-critical density.³⁶ The charging observed in the present experiment probably comes from the same source: a fraction of the hot TPD electrons moves inward and creates an electrostatic potential difference between the quarter-critical-density region (positively charged) and the target shell (negatively charged). The energy needed to produce the inferred charge is a very small fraction of the incident laser energy $E \sim Q^2/R_t \sim 2 \times 10^{-3}$ J. The energy to support this charging during the implosion, however, could be significantly larger because of dissipations in the associated return currents.

Electromagnetic fields around mount stalks supporting laser-irradiated targets have been measured using monoener-

getic (~ 3.3 -MeV) proton radiography.³⁷ A source of the fields in this experiment was believed to be a return current of up to ~ 7 kA driven through the stalk from positively charged targets. This current created toroidal magnetic fields of $\sim 10^4$ G. Considering the inferred magnitude of magnetic fields from the return currents versus the magnitude of self-generated fields around the stalk in the present experiment [\sim MG (see Fig. 138.14)], one concludes that it is unlikely these currents make a significant contribution to image C of the stalks in Fig. 138.12.

The measured radiographs show ripple structures quasi-spherically distributed around the targets (feature E in Fig. 138.12). These structures were not reproduced in simulations and apparently were caused by small-scale electromagnetic fields in the corona. The nature of these fields is unclear. Numerical models suggest that the ripples are localized near the radius of the quarter-critical density. It is known that various laser-plasma instabilities can develop near this radius, including stimulated Brillouin and Raman scatterings and TPD instability.³⁶ It is plausible that the observed ripples are related to electromagnetic fields caused by these instabilities.

The simulations have demonstrated the effect of self-generated magnetic fields on the dynamics of laser-ablated plasma. This effect occurs as a result of changing heat fluxes by the fields in the conduction zone, when $\omega_e \tau_e \geq 0.3$. In this case, the fluxes are suppressed in one direction and, being redirected, amplified in another direction. Such a redirection of the fluxes causes the change in the ablation pressure near the perturbations, which, in turn, causes the change in the perturbations. The dynamic effect of the field-modified heat fluxes, however, was found to be not significant enough to be observed in the present experiment.

ACKNOWLEDGMENT

This material is based upon work supported by the Department of Energy National Nuclear Security Administration under Award Number DE-NA0001944, the University of Rochester, and the New York State Energy Research and Development Authority. The support of DOE does not constitute an endorsement by DOE of the views expressed in this article.

Appendix: MHD Numerical Method

Electric and self-generated magnetic fields in implosion targets are simulated by employing the 2-D hydrodynamic ICF code *DRACO*,²⁷ which uses the Eulerian hydrodynamics and has been modified to solve the induction equation and include the effects of magnetic fields on the heat transport and plasma dynamics. The flow is assumed to be axisymmetric and the magnetic field has only the azimuthal component $\mathbf{B} = (0, 0, B_\phi)$. The induction equation is used in the Braginskii's form¹

$$\frac{\partial \mathbf{B}}{\partial t} = \nabla \times (\mathbf{V} \times \mathbf{B}) + \frac{c}{e} \nabla \times \frac{\nabla P_e}{n_e} - \nabla \times \frac{\mathbf{j} \times \mathbf{B}}{en_e} - \frac{c}{e} \nabla \times \frac{\mathbf{R}}{n_e}, \quad (\text{A1})$$

where $\mathbf{V} = V_r, V_\theta, 0$ is the flow velocity and $\mathbf{j} = (c/4\pi)\nabla \times \mathbf{B}$ is the current density. The force \mathbf{R} acts on electrons and consists of two components: $\mathbf{R} = \mathbf{R}_u + \mathbf{R}_T$, where

$$\mathbf{R}_u = -\alpha_\perp u_\perp + \alpha_\Lambda (\mathbf{h} \times \mathbf{u}) \quad (\text{A2})$$

is the friction force and

$$\mathbf{R}_T = -\beta_\perp^{uT} \nabla_\perp T_e - \beta_\perp^{uT} (\mathbf{h} \times \nabla T_e) \quad (\text{A3})$$

is the thermal force, $\mathbf{u} = -\mathbf{j}/en_e$ is the electron-ion relative velocity, and \mathbf{h} is the unit vector in the ϕ direction. The subscript “ \perp ” in Eqs. (A3) and (A4) refers to vector components tangential to \mathbf{B} .

The electron heat flux is represented by two components: $\mathbf{q}_e = \mathbf{q}_T^e + \mathbf{q}_u^e$, where

$$\mathbf{q}_T^e = -\kappa_\perp^e \nabla_\perp T_e - \kappa_\Lambda^e (\mathbf{h} \times \nabla T_e) \quad (\text{A4})$$

is the thermal component, which consists of the modified Spitzer flux⁸ and lateral (cross-gradient) flux (the first and second terms on the right-hand side, respectively), and

$$\mathbf{q}_u^e = -\beta_\perp^{Tu} u_\perp + \beta_\Lambda^{Tu} (\mathbf{h} \times \mathbf{u}) \quad (\text{A5})$$

is the friction component. The coefficients $\beta_\perp^{uT}, \beta_\Lambda^{uT}, \beta_\perp^{Tu}, \beta_\Lambda^{Tu}, \alpha_\perp, \alpha_\Lambda, \kappa_\perp^e$, and κ_Λ^e in Eqs. (A3)–(A6) are defined in Ref. 1 as functions of the Hall parameter $\omega_e \tau_e$ and the ion charge Z . The standard flux limitation³⁸ (with the flux-limiter parameter $f = 0.06$) of the thermal component \mathbf{q}_T^e is applied to mimic energy losses because of cross-beam energy transfer.³⁹

The release of energy caused by magnetic dissipation is accounted for by adding the term

$$Q_e = -\mathbf{R} \cdot \mathbf{u} \quad (\text{A6})$$

in the energy equation for electrons. The dynamic effects of magnetic fields are described by the magnetic force term

$$\mathbf{F}_m = \frac{1}{c} (\mathbf{j} \times \mathbf{B}) \quad (\text{A7})$$

in the equation of motion.

The MHD approximation fails when the free path of charged particles exceeds the characteristic scale lengths of a problem. In implosion simulations, such conditions, for example, can appear at the front of plasma, expanding into vacuum. A simple application of Eq. (A1) in these conditions can result in a significant overestimation of self-generated magnetic fields. To prevent such an unphysical behavior, calculations of spatial derivatives in the source and pinch terms of Eq. (A1) (the second and fourth, and third terms, respectively, on the right-hand side of this equation) should use limited scale lengths: they cannot be smaller than the electron free path ℓ_e . In practice, the limitation is implemented by substituting the grid size Δx by $\max(\Delta x, \epsilon \ell_e)$ when calculating the derivative $\partial f / \partial x \approx \Delta f / \Delta x$. Here, ϵ is a parameter of an order of unity.

REFERENCES

1. S. I. Braginskii, in *Reviews of Plasma Physics*, edited by Acad. M. A. Leontovich (Consultants Bureau, New York, 1965), Vol. 1, p. 205.
2. V. V. Korobkin and R. V. Serov, *JETP Lett.* **4**, 70 (1966).
3. G. A. Askar'yan *et al.*, *JETP Lett.* **5**, 93 (1967).
4. J. A. Stamper *et al.*, *Phys. Rev. Lett.* **26**, 1012 (1971).
5. A. Raven, O. Willi, and P. T. Rumsby, *Phys. Rev. Lett.* **41**, 554 (1978).
6. S. Atzeni and J. Meyer-ter-Vehn, *The Physics of Inertial Fusion: Beam Plasma Interaction, Hydrodynamics, Hot Dense Matter*, International Series of Monographs on Physics (Clarendon Press, Oxford, 2004), pp. 47–50.
7. B. H. Ripin *et al.*, *Phys. Rev. Lett.* **34**, 1313 (1975).
8. L. Spitzer, Jr. and R. Härm, *Phys. Rev.* **89**, 977 (1953).
9. A. Nishiguchi, *Jpn. J. Appl. Phys.* **41**, 326 (2002).
10. T. R. Boehly, D. L. Brown, R. S. Craxton, R. L. Keck, J. P. Knauer, J. H. Kelly, T. J. Kessler, S. A. Kumpan, S. J. Loucks, S. A. Letzring, F. J. Marshall, R. L. McCrory, S. F. B. Morse, W. Seka, J. M. Soares, and C. P. Verdon, *Opt. Commun.* **133**, 495 (1997).
11. M. Tatarakis *et al.*, *Nature* **415**, 280 (2002).
12. M. Borghesi *et al.*, *Laser Part. Beams* **20**, 269 (2002).
13. C. K. Li, F. H. Séguin, J. A. Frenje, J. R. Rygg, R. D. Petrasso, R. P. J. Town, P. A. Amendt, S. P. Hatchett, O. L. Landen, A. J. Mackinnon, P. K. Patel, V. Smalyuk, J. P. Knauer, T. C. Sangster, and C. Stoeckl, *Rev. Sci. Instrum.* **77**, 10E725 (2006).
14. E. L. Clark *et al.*, *Phys. Rev. Lett.* **84**, 670 (2000).
15. A. Zylstra, C. K. Li, H. G. Rinderknecht, F. H. Séguin, R. D. Petrasso, C. Stoeckl, D. D. Meyerhofer, P. Nilson, T. C. Sangster, S. Le Pape, A. Mackinnon, and P. Patel, *Rev. Sci. Instrum.* **83**, 013511 (2012).

16. A. J. Mackinnon, P. K. Patel, R. P. Town, M. J. Edwards, T. Phillips, S. C. Lerner, D. W. Price, D. Hicks, M. H. Key, S. Hatchett, S. C. Wilks, M. Borghesi, L. Romagnani, S. Kar, T. Toncian, G. Pretzler, O. Willi, M. Koenig, E. Martinolli, S. Lepape, A. Benuzzi-Mounaix, P. Audebert, J. C. Gauthier, J. King, R. Snavely, R. R. Freeman, and T. Boehly, *Rev. Sci. Instrum.* **75**, 3531 (2004).
17. J. R. Rygg, F. H. Séguin, C. K. Li, J. A. Frenje, M. J.-E. Manuel, R. D. Petrasso, R. Betti, J. A. Delettrez, O. V. Gotchev, J. P. Knauer, D. D. Meyerhofer, F. J. Marshall, C. Stoeckl, and W. Theobald, *Science* **319**, 1223 (2008).
18. C. K. Li, F. H. Séguin, J. A. Frenje, M. Manuel, D. Casey, N. Sinenian, R. D. Petrasso, P. A. Amendt, O. L. Landen, J. R. Rygg, R. P. J. Town, R. Betti, J. Delettrez, J. P. Knauer, F. Marshall, D. D. Meyerhofer, T. C. Sangster, D. Shvarts, V. A. Smalyuk, J. M. Soures, C. A. Back, J. D. Kilkenny, and A. Nikroo, *Phys. Plasmas* **16**, 056304 (2009).
19. C. K. Li, F. H. Séguin, J. A. Frenje, J. R. Rygg, R. D. Petrasso, R. P. J. Town, P. A. Amendt, S. P. Hatchett, O. L. Landen, A. J. Mackinnon, P. K. Patel, V. A. Smalyuk, T. C. Sangster, and J. P. Knauer, *Phys. Rev. Lett.* **97**, 135003 (2006).
20. P. Nicolai *et al.*, *Phys. Plasmas* **7**, 4250 (2000).
21. M. J.-E. Manuel, C. K. Li, F. H. Séguin, J. Frenje, D. T. Casey, R. D. Petrasso, S. X. Hu, R. Betti, J. D. Hager, D. D. Meyerhofer, and V. A. Smalyuk, *Phys. Rev. Lett.* **108**, 255006 (2012); M. J.-E. Manuel, C. K. Li, F. H. Séguin, J. A. Frenje, D. T. Casey, R. D. Petrasso, S. X. Hu, R. Betti, J. D. Hager, D. D. Meyerhofer, and V. Smalyuk, *Phys. Plasmas* **19**, 082710 (2012).
22. L. Gao, P. M. Nilson, I. V. Igumenshchev, S. X. Hu, J. R. Davies, C. Stoeckl, M. G. Haines, D. H. Froula, R. Betti, and D. D. Meyerhofer, *Phys. Rev. Lett.* **109**, 115001 (2012).
23. L. Gao, P. M. Nilson, I. V. Igumenshchev, G. Fiksel, R. Yan, J. R. Davies, D. Martinez, V. Smalyuk, M. G. Haines, E. G. Blackman, D. H. Froula, R. Betti, and D. D. Meyerhofer, *Phys. Rev. Lett.* **110**, 185003 (2013).
24. A. J. Mackinnon *et al.*, *Phys. Rev. Lett.* **97**, 045001 (2006).
25. F. H. Séguin, C. K. Li, M. J.-E. Manuel, H. G. Rinderknecht, N. Sinenian, J. A. Frenje, J. R. Rygg, D. G. Hicks, R. D. Petrasso, J. Delettrez, R. Betti, F. J. Marshall, and V. A. Smalyuk, *Phys. Plasmas* **19**, 012701 (2012).
26. C. K. Li, F. H. Séguin, J. R. Rygg, J. A. Frenje, M. Manuel, R. D. Petrasso, R. Betti, J. Delettrez, J. P. Knauer, F. Marshall, D. D. Meyerhofer, D. Shvarts, V. A. Smalyuk, C. Stoeckl, O. L. Landen, R. P. J. Town, C. A. Back, and J. D. Kilkenny, *Phys. Rev. Lett.* **100**, 225001 (2008).
27. D. Keller, T. J. B. Collins, J. A. Delettrez, P. W. McKenty, P. B. Radha, B. Whitney, and G. A. Moses, *Bull. Am. Phys. Soc.* **44**, 37 (1999); I. V. Igumenshchev, F. J. Marshall, J. A. Marozas, V. A. Smalyuk, R. Epstein, V. N. Goncharov, T. J. B. Collins, T. C. Sangster, and S. Skupsky, *Phys. Plasmas* **16**, 082701 (2009).
28. A. Z. Dolginov and V. A. Urpin, *Sov. Phys.-JETP* **50**, 912 (1979).
29. A. Nishiguchi *et al.*, *Phys. Rev. Lett.* **53**, 262 (1984).
30. Y. Lin, T. J. Kessler, and G. N. Lawrence, *Opt. Lett.* **20**, 764 (1995).
31. T. R. Boehly, V. A. Smalyuk, D. D. Meyerhofer, J. P. Knauer, D. K. Bradley, R. S. Craxton, M. J. Guardalben, S. Skupsky, and T. J. Kessler, *J. Appl. Phys.* **85**, 3444 (1999).
32. S. Skupsky and R. S. Craxton, *Phys. Plasmas* **6**, 2157 (1999).
33. L. J. Waxer, D. N. Maywar, J. H. Kelly, T. J. Kessler, B. E. Kruschwitz, S. J. Loucks, R. L. McCrory, D. D. Meyerhofer, S. F. B. Morse, C. Stoeckl, and J. D. Zuegel, *Opt. Photonics News* **16**, 30 (2005).
34. D. G. Hicks, C. K. Li, F. H. Séguin, J. D. Schnittman, A. K. Ram, J. A. Frenje, R. D. Petrasso, J. M. Soures, D. D. Meyerhofer, S. Roberts, C. Sorce, C. Stoeckl, T. C. Sangster, and T. W. Phillips, *Phys. Plasmas* **8**, 606 (2001).
35. N. Sinenian, A. B. Zylstra, M. J. E. Manuel, H. G. Rinderknecht, J. A. Frenje, F. H. Séguin, C. K. Li, R. D. Petrasso, V. Goncharov, J. Delettrez, I. V. Igumenshchev, D. H. Froula, C. Stoeckl, T. C. Sangster, D. D. Meyerhofer, J. A. Cobble, and D. G. Hicks, *Appl. Phys. Lett.* **101**, 114102 (2012).
36. W. L. Kruer, in *The Physics of Laser Plasma Interactions*, *Frontiers in Physics*, Vol. 73, edited by D. Pines (Addison-Wesley, Redwood City, CA, 1988).
37. M. J.-E. Manuel *et al.*, *Appl. Phys. Lett.* **100**, 203505 (2012).
38. R. C. Malone, R. L. McCrory, and R. L. Morse, *Phys. Rev. Lett.* **34**, 721 (1975).
39. I. V. Igumenshchev, D. H. Edgell, V. N. Goncharov, J. A. Delettrez, A. V. Maximov, J. F. Myatt, W. Seka, A. Shvydky, S. Skupsky, and C. Stoeckl, *Phys. Plasmas* **17**, 122708 (2010).

Absolute Calibration of the OMEGA Streaked Optical Pyrometer for Laser-Driven Shock Waves

Introduction

Equation-of-state (EOS) physics at extreme pressures and temperatures is important in inertial confinement fusion (ICF),^{1,2} astrophysics,³ material sciences,⁴ and other areas of high-energy-density physics (HEDP).^{5,6} Of particular importance is the relation of a material's thermal-state variables to its mechanical-state variables. A typical EOS study entails an impedance-matching experiment to determine the kinematic properties (pressure, density, and internal energy) of a material coupled with a simultaneous temperature measurement to provide its thermal behavior (temperature and entropy).⁷ Laser-driven shock-wave experiments produce extremely high pressures and enable one to measure a material's behavior at extreme conditions ($P > 1$ Mbar; $T > 1$ eV) (Ref. 8). The Omega Laser Facility⁹ readily produces these conditions over nano-second time scales and millimeter-scale areas. Diagnosis of these experiments requires relatively high spatial and temporal resolution. A line-imaging velocity interferometer system for any reflector (VISAR)¹⁰ is used to determine the material's mechanical-state variables by measuring shock velocities with ~ 50 -ps and < 10 - μm resolution. A streaked optical pyrometer (SOP) simultaneously records the space/time history of the material's thermal self-emission between 590 and 850 nm with similar temporal and spatial resolution.¹⁰ Self-emission from the shock-compressed material is converted to a brightness temperature by comparing its emission to that of a black-body radiator.¹¹ Together these measurements provide temperature as a function of pressure or density.

By absolutely calibrating the SOP over its wavelength range, one is able to measure the spectral radiance of an emitting shock front and assign it a brightness temperature. This article presents the technique and results of the absolute calibration of the OMEGA SOP. The details of recent design changes to the SOP, upgraded in 2011, are also presented.

Experimental Configuration

In a typical laser-driven shock-wave experiment, a target is irradiated by lasers (direct drive) or by x rays from a laser-driven hohlraum (indirect drive).¹ These drivers cause the outer

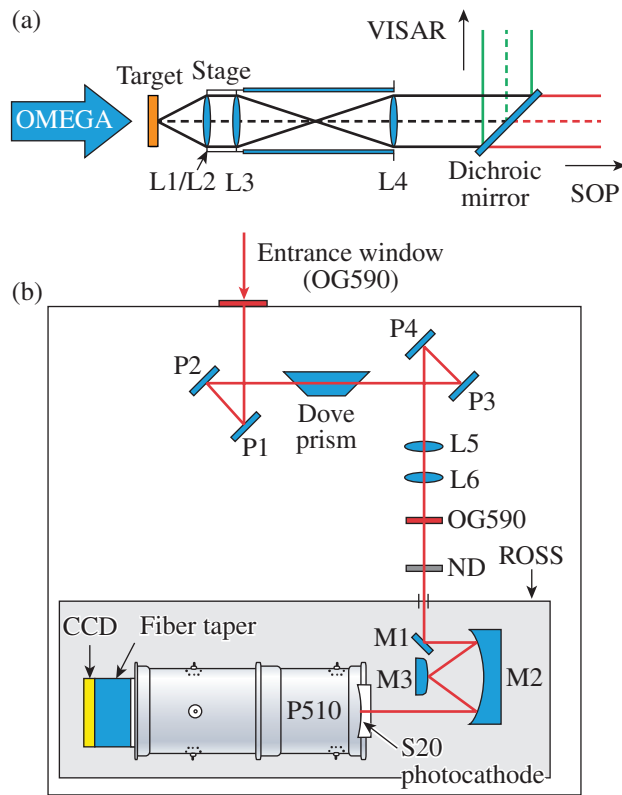
layer of the target (the ablator) to blow off and expand outward, launching a forward-moving shock wave through the target material. The shock compresses the material and induces high temperature, pressure, and internal energy.

Opposite the drive beams, the reflected VISAR probe beam and the self-emission from the shock are collected by an $f/3.3$ telescope. As shown in Fig. 138.23(a), the telescope, mounted on a mechanical stage, consists of a two-lens objective (L1/L2) followed by a planoconvex singlet (L3). The combined signal (reflected probe and self-emission) first encounters the meniscus lens (L1) that also acts as a disposable blast shield that prevents debris from hitting the next optic, a collimating achromat (L2). After L2, the signal passes through a planoconvex singlet (L3) and is recollimated by a second achromat (L4) at the rear of the ten-inch manipulator (TIM) that houses the telescope. The signal is then relayed toward a dichroic mirror that reflects the 532-nm probe beam. The self-emission passes through the dichroic mirror toward the SOP diagnostic shown in Fig. 138.23(b). Details of the optical telescope and the VISAR design can be found in Ref. 10.

The entrance to the SOP cabinet is an OG590 long-pass filter that transmits only light with a wavelength greater than 590 nm. Inside, the target emission is imaged onto the external slit of a Rochester Optical Streak System¹² (ROSS) camera by a series of periscopes and turning mirrors. A dove prism is used to rotate the target image on the slit, making it possible for the SOP to spatially resolve along any orientation on the target. To compensate for the refractive optics in the telescope (optimized for the 532-nm VISAR probe beam), the signal passes through a 300-mm planoconvex singlet (L5) and a 200-mm planoconcave singlet (L6) to focus the light onto the ROSS camera's external slit. Ahead of the slit are a second OG590 filter and any neutral density (ND) filters used for the experiment.

Inside the ROSS camera [bottom of Fig. 138.23(b)], the self-emission signal is focused by an Offner triplet system (M1–M3) onto the S20 photocathode with a sapphire window. Photoelectrons are accelerated through the streak tube toward

the phosphor screen. Photons emitted by the phosphor screen are transmitted through a 1:1 fiber-optic taper directly onto the charged-coupled-device (CCD) camera. The CCD is regularly binned 2×2 for an 1100×1100 -pixel output. The data are spatially resolved in one dimension (along the slit length) and “streaked” in the other dimension to provide temporal resolution transverse to the slit. Data are recorded using 6-, 17-, 46-, or 96-ns sweep windows. The spectral range of the SOP (~ 590 to 850 nm) is defined by the OG590 filters at shorter wavelengths and the photocathode’s insensitivity to infrared wavelengths.



E22695JR

Figure 138.23

(a) OMEGA drivers launch a forward-moving shock wave through the target. The reflected VISAR (velocity interferometer for any reflector) probe beam and the self-emission of the material directly behind the shock front are simultaneously relayed outside the target chamber by the $f/3.3$ telescope. The 532-nm probe beam is reflected off the dichroic mirror and self-emission in the near-infrared passes through to (b) the SOP (streaked optical pyrometer) diagnostic. Self-emission enters the SOP diagnostic through an OG590 long-pass filter and is relayed by the SOP optics to the external slit of the Rochester Optical Streak System (ROSS) camera. The image of the slit is focused onto the S20 photocathode in the P510 streak tube by an Offner triplet, a 1:1 all-reflective image relay. Photons emitted by the phosphor screen are transmitted through a fiber-optic taper directly onto the charged-coupled-device (CCD) camera.

In 2011 the SOP was upgraded from the version described in Ref. 11 to that described above.¹³ Most notably, the detector was upgraded from a Hamamatsu C4187 streak camera¹⁴ to a ROSS camera.^{12,15} The new streak camera contains a Photonis P510 streak tube¹⁶ and an SI-800 TE cooled CCD camera¹⁷ with an E2V CCD chip.¹⁸ In addition, enhancements were made to the SOP optical relay.¹³ These upgrades required an absolute calibration of the new system. The calibration method was similar to that of the previous SOP system as described in Ref. 11.

Calibration Method

The SOP was absolutely calibrated using a light source with a known spectral radiance: an Optronic Laboratories (OL550) Standard of Spectral Radiance, which is a modified GE Type 18A/T10/2P lamp having a tungsten ribbon filament fitted with a sapphire window.¹⁹ This lamp, driven by a constant-current (15-A) power supply, has a National Institute of Standards and Technology (NIST)–traceable calibrated spectral radiance that is accurate to 1% (Ref. 19). The lamp was placed at the center of the OMEGA target chamber, and the telescope was adjusted until the tungsten ribbon filament was imaged onto the external slit of the SOP ROSS. Care was taken to ensure that the filament image was centered on the photocathode. Prior to the calibration, the photocathode’s spatial profile was measured by scanning the external slit image across the photocathode by tilting the secondary mirror [M3 in Fig. 138.23(b)] of the Offner triplet system within the ROSS camera. The center and full width at half maximum (FWHM) of the photocathode were determined using the measured profile. These procedures ensured that the internal optics of the streak camera, which are motorized and adjusted remotely, were aligned consistently during calibrations and experiments.

During the calibration, the SOP was operated with a 5-s sweep window to produce sufficient intensity for the detector since the spectral radiance of the lamp ($T \sim 0.24$ eV) is considerably lower than that of a shock ($T > 1$ eV). To calibrate the spectral system response function of the SOP, seven 40-nm-wide bandpass filters were individually inserted to isolate narrow regions of the lamp’s emission spectrum. The spectral system response of the SOP was determined by correcting an estimated response function using these narrowband measurements.

The SOP camera output in analog-to-digital units (ADU’s) of a single pixel is given by

$$I = \frac{\Delta t}{G} \int_{\text{all } \lambda} d\lambda \Phi_s(\lambda) T_x(\lambda) \text{SR}(\lambda), \quad (1)$$

where Δt is the dwell time of a single pixel, G is the streak camera gain of photoelectrons to ADU's, $\Phi_s(\lambda)$ is the spectral radiant power from the light source, $T_x(\lambda)$ is the transmission of any removable ND or bandpass filters introduced to the system, and $SR(\lambda)$ is the SOP's spectral system response. The system response includes the S20 photocathode sensitivity and the transmission of all optical elements comprising the SOP. The transmission spectra of the ND and bandpass filters were measured using a Perkin-Elmer Lambda 900 spectrometer to 0.1% accuracy.²⁰ The dwell time,

$$\Delta t = \frac{W_{\text{LSF}}}{B\Delta x\eta}, \quad (2)$$

is the amount of time that a given "streak" spends at a single pixel. B is the binning of the CCD (e.g., two for 2×2 binning), Δx is the length of one (square) pixel, η is the sweep rate given in pixels/ns, and W_{LSF} is the apparent slit width defined as the FWHM of the streak camera's line spread function (LSF). The ROSS camera optics provide a virtual cathode, resulting in an apparent external slit width that is considerably narrower than the actual slit width [Fig. 138.24(a)], enabling higher temporal resolution.

The spectral radiant power from the lamp's filament that maps to a single pixel is given by

$$\Phi_s(\lambda) = \int_{A_{\text{pixel}}} dA \int_{\Omega_{\text{lens}}} d\Omega L_s(\lambda), \quad (3)$$

where $L_s(\lambda)$ is the source radiance, A_{pixel} is the filament area that maps to a single pixel, and Ω_{lens} is the solid angle of the $f/3.3$ telescope. The amount of light that is recorded onto one pixel originates from a portion of the tungsten filament with the area

$$A_{\text{pixel}} = \left(\frac{B\Delta x}{MM_{\text{EO}}} \right) \left(\frac{B\Delta x W_s}{MW_{\text{LSF}}} \right), \quad (4)$$

where W_s is the external slit width, M is the magnification from the light source to the photocathode, and M_{EO} is the magnification in the spatial direction (along the slit) of the electron optics within the streak tube.

An estimate for the wideband (590- to 850-nm) system response function was developed by combining the estimated sensitivity of the S20 photocathode and the measured transmission spectra of the SOP optics. This estimate was corrected using data taken in seven narrow wavelength regions using 40-nm-wide bandpass filters. Neutral-density (ND) filters were used as needed to limit the photocathode current. A series of three to five streaks were acquired with each bandpass filter in place, and the average of their measured intensities defined the SOP response in that wavelength range. For each of the seven wavelength ranges, the theoretical camera output I in ADU's was modeled using Eqs. (1)–(4) as

$$I = \frac{B\Delta x\Omega_{\text{lens}}W_s}{GM^2M_{\text{EO}}\eta} \int_{\text{all } \lambda} d\lambda L_s(\lambda)T_x(\lambda)SR(\lambda) \quad (5)$$

with the estimate for $SR(\lambda)$ and the measured transmission spectra $T_x(\lambda)$ of the relevant bandpass and ND filters. The estimated system response was iteratively corrected until the model predicted the measured camera output in the seven narrowband regions. The validity of the corrected system response function was verified by calculating the camera output when observing the tungsten-filament source over the entire wavelength range of the SOP. The model correctly predicted the wideband measurements within 4%. The dashed line in Fig. 138.25 shows the calibrated spectral system response, and the solid line shows the spectral radiance of the calibrated tungsten-filament lamp over the SOP's wavelength range. The lamp's spectral radiance is NIST traceable and is characteristic of a 0.239-eV gray body with an emissivity of 0.215 (Ref. 19).

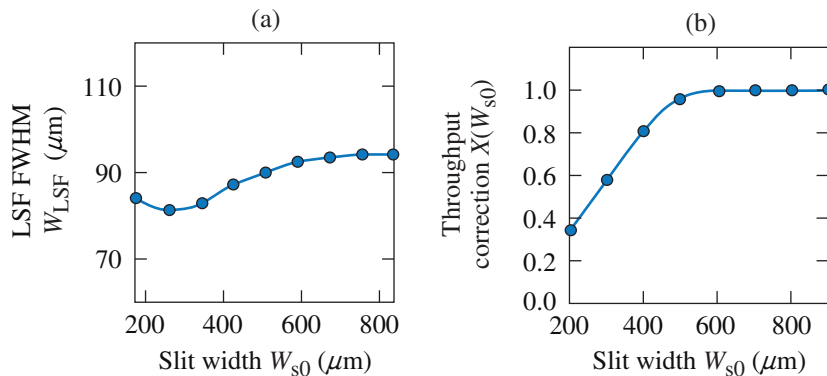
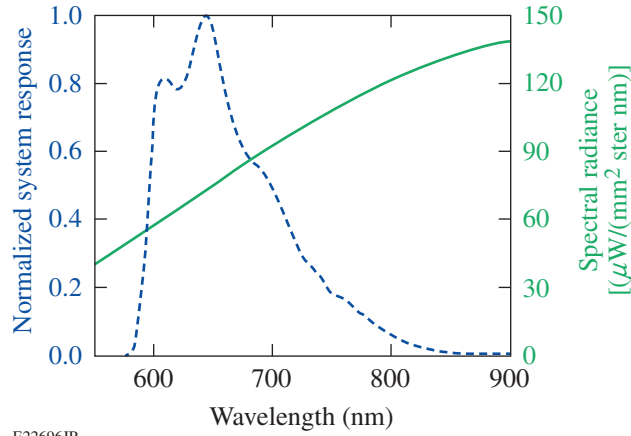


Figure 138.24

(a) The line spread function (LSF) full width at half maximum (FWHM) and (b) throughput correction vary with slit width. (a) The apparent slit width (W_{LSF}) is narrower than the actual slit width (W_{s0}) and remains fairly constant close to 90 μm for all slit widths. (b) Throughput correction [$X(W_{s0})$] in Eq. (8) is defined as the ratio of camera output at the experimental slit width (W_{s0}) to camera output at the calibration slit width (W_s) of 800 μm .



E22696JR

Figure 138.25

The SOP system response (dashed line) was determined using the individual spectral responses measured in each narrow wavelength region. A NIST-traceable tungsten-filament lamp with known spectral radiance (solid line) was used as the calibrated light source for the SOP calibration.

Brightness temperature is inferred from the SOP camera output by relating the spectral radiance $L_s(\lambda)$ of the observed source to that of an equivalent blackbody through Planck's law. The predicted SOP signal for such a source is given by

$$I = \frac{B\Delta x\Omega_{\text{lens}}W_sX(W_{s0})2hc^2}{GM^2M_{\text{EO}}\eta} \int_{\text{all } \lambda} d\lambda \frac{T_x(\lambda)SR(\lambda)}{\lambda^5 \left[\exp\left(\frac{hc}{\lambda T}\right) - 1 \right]}, \quad (6)$$

where h is Planck's constant, c is the speed of light, and $X(W_{s0})$ is the throughput correction defined as the ratio of the camera throughput at the experimental slit width W_{s0} to the camera throughput at the calibration slit width W_s . There is a nonlinear relationship between throughput and slit width as shown in Fig. 138.24(b). Since $SR(\lambda)$ was determined at W_s and not necessarily W_{s0} , $X(W_{s0})$ adjusts for the difference in throughput. The throughput corrections for the slit widths of 200 to 800 μm are presented in Table 138.V. The adjustable parameters for an experiment include the experimental slit width W_{s0} , the sweep rate η , and the transmission spectra of the ND filters $T_x(\lambda)$. The first two parameters change the effective

sensitivity of the camera for all wavelengths, whereas $T_x(\lambda)$ can have wavelength dependence and, therefore, must be included within the integral in Eq. (6). For a given experimental configuration [i.e., W_{s0} , η , and $T_x(\lambda)$], the camera output is calculated for a range of temperatures using Eq. (6). By approximating the wavelength dependence of the SOP as a δ function at the centroid wavelength of the integrand in Eq. (6), the predicted T versus I data are then fit to the relationship

$$T = \frac{T_0}{\ln\left(1 + \frac{A}{I}\right)}, \quad (7)$$

where A and T_0 are calibration parameters determined by a least-squares fit. This approximation is valid since the spectral band of the SOP is narrow compared to the spectral band of a Planckian source with a temperature above 5000 K. Parameter A can be rewritten as

$$A = \frac{A_0X(W_{s0})}{\eta}. \quad (8)$$

The system gain and binning ($B = 2$ for 1100×1100 -pixel output) are fixed for all shots and are included in the calibration parameter A_0 . Seven independent calibrations were performed to provide calibration parameters for SOP experiments beginning with shot 68276. The calibration parameters A_0 and T_0 (Table 138.VI) depend only on the shot number and ND filter used. There was an increase in the internal voltages of the streak camera that increased the values of A_0 beginning with shot 71573. There was also a subsequent decrease in SOP output caused by the accumulation of debris on the rear window of the TIM that houses the telescope. Because of these two effects, the values for A_0 must be scaled by the amounts specified in Table 138.VI for shots 71573 to 72436. Calibration parameter A_0 can be taken directly from Table 138.VI for shots 68276 to 71552 and shots 72437 to present.

To calculate brightness temperature from camera output in ADU's, one must first find the appropriate calibration parameters A_0 and T_0 from Table 138.VI; then use A_0 to calculate parameter A from Eq. (8) and both A and T_0 to calculate

Table 138.V: Throughput correction as a function of experimental slit width $X(W_{s0})$. There are two sets of values for the throughput correction because of a change in the external slit mechanism that occurred between shots 70551 and 70552. The throughput correction for shots 70552 and later is plotted in Fig. 138.24(b).

Experimental slit width W_{s0} (μm)	200	300	400	500	600	700	800
Shot 68276 to 70551	0.400	0.529	0.731	0.910	—	—	—
Shot 70552 to present	0.354	0.587	0.811	0.959	0.996	0.999	1.000

Table 138.VI: Brightness temperature is calculated using calibration parameters A_0 and T_0 in Eqs. (7) and (8). The calibration parameters are specified depending on the shot number and ND filter used in the experiment. ND filters are specified by their optical densities ranging from 0.1 to 2.5. For shots 71573 to 71875 multiply A_0 by 1.09. For shots 71876 to 72436 multiply A_0 by 1.05.

ND	T_0 (eV)	$A_0 = \text{ADU/ns}$
0	1.911	403,740
0.1	1.913	332,310
0.15	1.914	281,030
0.2	1.910	257,770
0.3	1.910	204,550
0.4	1.909	163,800
0.5	1.912	121,840
0.6	1.912	93,097
0.7	1.911	79,434
0.9	1.898	51,987
1.0	1.870	48,363
1.3	1.854	26,062
1.5	1.844	17,091
2.0	1.818	6,521
2.5	1.790	2,497

brightness temperature from Eq. (7). An example of inferred brightness temperature from SOP camera output for a typical experiment is shown in Fig. 138.26.

For experiments where a gray-body approximation is applicable, the intensity I is replaced by I/ε , where ε is the emissivity. Following Kirchoff's law for a body in thermal equilibrium,⁶ the emissivity is equal to the absorptivity, i.e., $\varepsilon = 1 - R$, where R is the reflectivity. If the dynamically compressed material is optically thick and reflects the 532-nm VISAR probe beam, one can extract R from the VISAR data. Temperatures for a gray body are then calculated using

$$T = \frac{T_0}{\ln \left[1 + \frac{(1-R)A}{I} \right]} \quad (9)$$

VISAR/SOP Example

Gray-body temperatures were inferred from the SOP and the VISAR data obtained in experiments designed to study the EOS of quartz. These experiments used unsupported shocks that slowly decayed as they traversed the sample. Since the

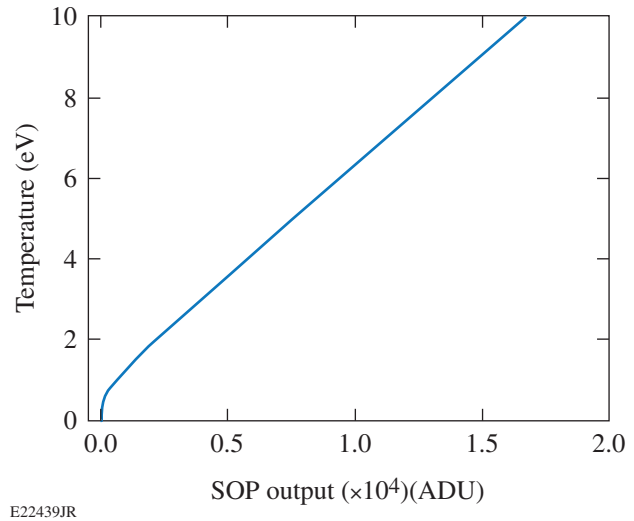


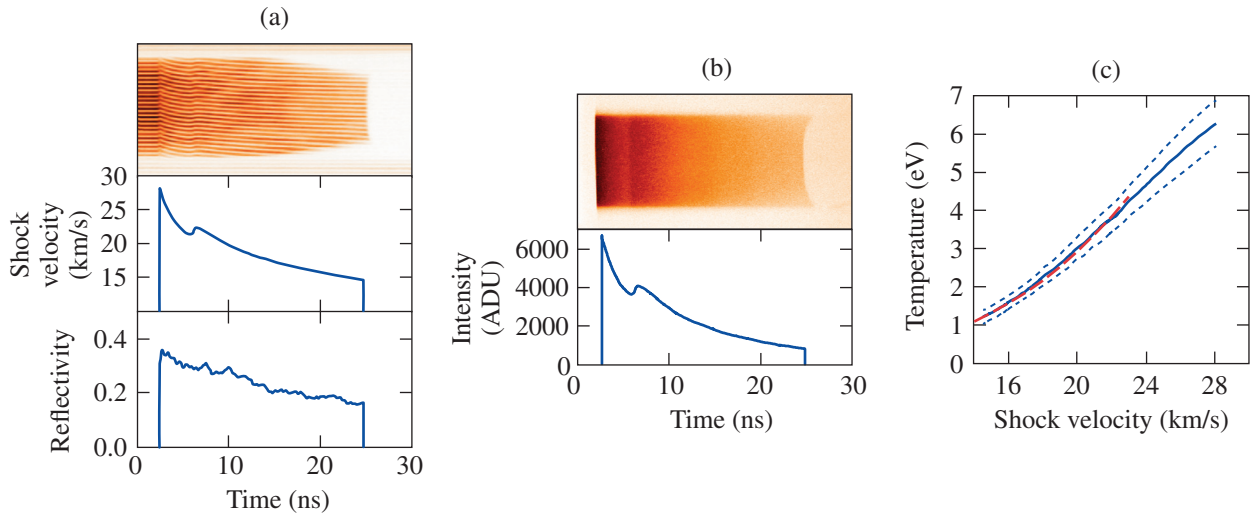
Figure 138.26

Inferred temperature dependence of the SOP signal for an experiment using a 17-ns sweep window, $W_{s0} = 800 \mu\text{m}$, and ND 0.3. This curve was generated using Eq. (7) with calibration constants $A_0 = 204550 \text{ ADU/ns}$ and $T_0 = 1.910 \text{ eV}$ calculated for data taken with an ND 0.3 filter.

α -quartz target samples were transparent, VISAR recorded the shock velocity and reflectivity of the decaying shock front as a function of time [Fig. 138.27(a)], while the SOP simultaneously recorded the self-emission intensity [Fig. 138.27(b)]. The emission of the α -quartz sample at each time was converted to a gray-body temperature using Eq. (9) with the appropriate calibration parameters A and T_0 and the reflectivity inferred from VISAR. This temperature is plotted versus the VISAR velocity at that time [solid blue line in Fig. 138.27(c)], providing temperature versus shock velocity (pressure). These data are compared to a power law fit for temperature as a function of shock velocity in α quartz [dashed red line in Fig. 138.27(c)]. The power law fit was created using α -quartz data obtained by Hicks⁵ and has the form $T = 1400 + 4.3 U_s^{2.98}$, where U_s is the shock velocity in km/s and T is the temperature in Kelvin.

Error Analysis

A Monte Carlo routine was used to estimate the errors in this calibration method. Contributions include uncertainties in the filter transmissions T_x (0.1%), spectral radiance of the lamp L_s (1%), calibration slit width W_s (1%), sweep rate η (0.5% for slow sweeps used in calibrations and 2% for fast sweeps used in experiments), gain G (2%), throughput correction $X(W_{s0})$ (0.5% for an 800- μm -wide slit), and magnifications M (0.2%) and M_{EO} (0.5%). Uncertainties of 4% in parameter A_0 and 0.1% in parameter T_0 were estimated using 10,000 Monte Carlo runs that mimicked the calibration procedure and used the uncertainties in the narrowband measurements from the seven



E22697JR

Figure 138.27

Sample VISAR and SOP data for an experiment using decaying shock waves in α -quartz targets for equation-of-state (EOS) studies. (a) The VISAR records temporally resolved shock velocity and reflectivity and (b) the SOP simultaneously records temporally resolved self-emission intensity. (c) Gray-body temperatures (solid blue line) were inferred from the SOP self-emission intensities using the SOP calibration and the VISAR reflectivity. The one-sigma standard deviations in temperature are represented by the dotted blue lines. These data are compared to a power law fit for temperature as a function of shock velocity in α quartz (dashed red line), which was created using α -quartz data obtained by D. Hicks (Ref. 5).

independent calibrations. For each routine, all parameters were varied within their error estimates, which produced 10,000 possible system responses, A_0 's and T_0 's. The narrowband responses measured in five of the calibrations agreed within 3%. The other two calibrations yielded narrowband intensities that were 9% and 5% higher as a result of the initial increase in streak camera voltages and the subsequent accumulation of debris on the rear window of the TIM. These two calibrations reflect the state of the diagnostic during shots 71573 to 72436 where the additional scaling of parameter A_0 is required. The estimated uncertainty of 4% for parameter A_0 is still valid for these shots, provided that the appropriate scaling specified by Table 138.VI is used.

The uncertainty in temperature for the data presented in Fig. 138.27(c) was 10.5% between 2 and 6 eV and increased to 14% at 1.2 eV. The SOP intensity data for this shot were particularly noisy in the low-intensity region, which resulted in 25% uncertainty in the lower intensities. This led to a larger uncertainty (~14%) in temperatures below 2 eV. A typical experiment with a 7% uncertainty in intensity, 4% uncertainty in A_0 , 2% uncertainty in η , 0.5% uncertainty in $X(W_{s0})$, and 0.1% uncertainty in T_0 generates a total uncertainty in brightness temperature of 6.8% at 5 eV. This same experiment with a 20% uncertainty in reflectivity gives a 10% uncertainty in gray-body temperature at 5 eV.

Discussion and Conclusions

The streaked optical pyrometer on the OMEGA Laser System was absolutely calibrated using a NIST-traceable tungsten-filament lamp. Brightness temperatures of dynamically compressed materials are inferred from self-emission intensities using the spectral system response determined by the calibration. Gray-body temperature is calculated using the emissivity of the shock front determined by the VISAR measurement of its reflectivity.

Characterization of the streak camera throughput and LSF (Fig. 138.24) led to a recommendation of an 800- μm -wide slit for maximum throughput while maintaining temporal performance and providing some insensitivity to minor misalignments. Electron optics within the streak tube produce a virtual cathode, resulting in an apparent slit width that is considerably narrower than the actual slit width. The FWHM of the LSF (always $<100 \mu\text{m}$) is $\sim 8.5\times$ narrower than the actual slit width at 800 μm when the focus voltage of the streak tube is optimized for that slit width. When using the standard 2×2 binning for 1100×1100 -pixel output and an 800- μm -wide slit, the temporal integration time is 155 ps for the 46-ns sweep window and 60 ps for the 17-ns sweep window. During experiments and calibrations, the image of the external slit is aligned to the center of the photocathode. The photocathode has varying sensitivity across its profile; therefore, narrow slit widths

are sensitive to alignment. Wide slit widths [i.e., greater than the FWHM of the photocathode ($\sim 550 \mu\text{m}$)] are recommended to mitigate any slight misalignments, thereby minimizing shot-to-shot variations in camera performance. Uncertainty in the throughput correction [Fig. 138.24(b)] caused by a slight misalignment or inconsistency in the slit width is much lower for wide external slits. Uncertainty in $X(W_{s0})$ is 0.5% for slits greater than $600 \mu\text{m}$ and increases to 5% for narrow slit widths less than $600 \mu\text{m}$. For these reasons, an $800\text{-}\mu\text{m}$ slit is recommended as a balance that optimizes throughput and temporal resolution while minimizing sensitivity to minor misalignment to the photocathode. The SOP calibration is performed using an $800\text{-}\mu\text{m}$ -wide slit.

To obtain brightness temperature from SOP intensity, one must first obtain the appropriate calibration constants A_0 and T_0 from Table 138.VI based on the ND filter used in the experiment. One then calculates parameter A from A_0 and the adjustable system parameters η and W_{s0} using Eq. (8). After acquiring A and T_0 , one uses Eq. (7) to calculate brightness temperature or Eq. (9) to calculate gray-body temperature.

ACKNOWLEDGMENT

This material is based upon work supported by the Department of Energy National Nuclear Security Administration under Award Number DE-NA0001944, the University of Rochester, and the New York State Energy Research and Development Authority. The support of DOE does not constitute an endorsement by DOE of the views expressed in this article. We acknowledge R. Paguio, M. Farrell, and A. Nikroo (General Atomics) as well as D. R. Harding and M. J. Bonino for target preparation.

REFERENCES

1. J. D. Lindl, *Inertial Confinement Fusion: The Quest for Ignition and Energy Gain Using Indirect Drive* (Springer-Verlag, New York, 1998).
2. S. Hamel, L. X. Benedict, P. M. Celliers, M. A. Barrios, T. R. Boehly, G. W. Collins, T. Döppner, J. H. Eggert, D. R. Farley, D. G. Hicks, J. L. Kline, A. Lazicki, S. LePape, A. J. Mackinnon, J. D. Moody, H. F. Robey, E. Schwegler, and P. A. Sterne, *Phys. Rev. B* **86**, 094113 (2012).
3. R. P. Drake, *High-Energy-Density Physics: Fundamentals, Inertial Fusion, and Experimental Astrophysics*, Shock Wave and High Pressure Phenomena (Springer, Berlin, 2006).
4. A. Sawaoka, ed. *Shock Waves in Materials Science* (Springer-Verlag, Tokyo, 1993).
5. D. G. Hicks, T. R. Boehly, J. H. Eggert, J. E. Miller, P. M. Celliers, and G. W. Collins, *Phys. Rev. Lett.* **97**, 025502 (2006).
6. Ya. B. Zel'dovich and Yu. P. Raizer, in *Physics of Shock Waves and High-Temperature Hydrodynamic Phenomena*, edited by W. D. Hayes and R. F. Probstein (Dover Publications, Mineola, NY, 2002).
7. M. A. Barrios, D. G. Hicks, T. R. Boehly, D. E. Fratanduono, J. H. Eggert, P. M. Celliers, G. W. Collins, and D. D. Meyerhofer, *Phys. Plasmas* **17**, 056307 (2010).
8. J. H. Eggert, D. G. Hicks, P. M. Celliers, D. K. Bradley, R. S. McWilliams, R. Jeanloz, J. E. Miller, T. R. Boehly, and G. W. Collins, *Nature Phys.* **6**, 40 (2010).
9. T. R. Boehly, D. L. Brown, R. S. Craxton, R. L. Keck, J. P. Knauer, J. H. Kelly, T. J. Kessler, S. A. Kumpan, S. J. Loucks, S. A. Letzring, F. J. Marshall, R. L. McCrory, S. F. B. Morse, W. Seka, J. M. Soures, and C. P. Verdon, *Opt. Commun.* **133**, 495 (1997).
10. P. M. Celliers, D. K. Bradley, G. W. Collins, D. G. Hicks, T. R. Boehly, and W. J. Armstrong, *Rev. Sci. Instrum.* **75**, 4916 (2004).
11. J. E. Miller, T. R. Boehly, A. Melchior, D. D. Meyerhofer, P. M. Celliers, J. H. Eggert, D. G. Hicks, C. M. Sorce, J. A. Oertel, and P. M. Emmel, *Rev. Sci. Instrum.* **78**, 034903 (2007).
12. P. A. Jaanimagi, R. Boni, D. Butler, S. Ghosh, W. R. Donaldson, and R. L. Keck, in *26th International Congress on High-Speed Photography and Photonics*, edited by D. L. Paisley *et al.* (SPIE, Bellingham, WA, 2005), Vol. 5580, pp. 408–415.
13. *November 2011 Progress Report on the Laboratory for Laser Energetics, Inertial Confinement Fusion Program Activities*, University of Rochester, Rochester, NY (2011).
14. Framing Streak Camera C4187, *Hamamatsu Specification Manual*, Hamamatsu Photonics K.K., Electron Tube Center, Japan.
15. Sydor ROSS 5100 Specification Manual, Sydor Instruments, LLC, Rochester, NY 14624.
16. PHOTONIS P510 Streak Tube Specification Manual, PHOTONIS, 19106 Brive, France.
17. Spectral Instruments 800S CCD Camera Specification Manual, Spectral Instruments, Tucson, AZ 85745 (http://www.specinst.com/Products/800s_datasheet.pdf).
18. e2v technologies, Elmsford, NY 10523-1482.
19. *OL Series 550 Standards of Spectral Radiance with Sapphire Windows Specification Manual*, Optronic Laboratories, Inc., Orlando, FL 32811.
20. Lambda900 Spectrophotometer, PerkinElmer, Waltham, MA 02451.

Multibeam Two-Plasmon Decay in Three Dimensions: Thresholds and Saturation

The parametric resonance of oscillators or waves is an effect that exists in areas of physics as diverse as geophysical fluid dynamics and galactic dynamics. Instabilities caused by the parametric excitation of waves in plasmas resulting from the presence of large-amplitude electromagnetic waves are of immediate concern to inertial confinement fusion (ICF),^{1,2} high-energy-density physics (HEDP),³ and ionospheric modification experiments.⁴ Most theoretical and numerical works to date have assumed that instability is driven by a single electromagnetic (EM) pump wave, despite the fact that almost all ICF and HEDP experiments overlap many beams. How instability is modified when multiple pump waves are present is an issue of practical and theoretical interest. Recent indirect-drive experiments at the National Ignition Facility (NIF) (where 96 beams overlap near each of the two laser entrance holes of a plasma-filled hohlraum) are examples that highlight the importance of cooperative, multibeam parametric instability. In these experiments a multibeam parametric instability known as cross-beam energy transfer (CBET) was shown to have a dramatic effect on implosion symmetry and target performance.^{5,6} In direct-drive ICF, where the fusion target is directly irradiated by many overlapping laser beams, two-plasmon decay (TPD) can occur. This problem has been studied for 40+ years, but there has been a strong resurgence of interest because of ignition-scale experiments on the NIF. TPD is important because it can generate hot electrons, which represent a preheat risk to the target.⁷ TPD is a three-wave decay instability in which an EM wave of frequency ω_0 and wave vector \vec{k}_0 decays into two electrostatic Langmuir waves (LW's), satisfying the resonance conditions $\omega_0 = \omega + \omega'$ and $\vec{k}_0 = \vec{k} + \vec{k}'$, where ω , ω' , and \vec{k} , \vec{k}' are the frequencies and wave vectors of the decay LW's, respectively. This instability can occur in the coronal plasma at electron densities close to the quarter-critical density $n_c/4$, where $n_c [= m_e \omega_0^2 / (4\pi e^2)]$ is the electron density at which EM waves are reflected. Here, e and m_e are the electron charge and mass, respectively.

In this article we present a linear three-dimensional (3-D) numerical stability analysis of TPD in an inhomogeneous plasma driven by multiple laser beams. This is followed by an investigation of the subsequent nonlinear evolution, where non-

linearity enters by the coupling of the LW's to low-frequency density perturbations. This model was in part motivated by a favorable comparison of the results with more-detailed, fully kinetic calculations in regimes where they can be compared (i.e., in two spatial dimensions).⁸ The existence of two forms of cooperative multibeam TPD instability is demonstrated. One form shares short-wavelength, high-group-velocity, collective (or common) LW's that convectively saturate (i.e., the waves undergo a finite spatial amplification),⁶ while the other is associated with shared long-wavelength, small-group-velocity LW's and is absolutely unstable (i.e., the waves grow in time). The identification of an absolutely unstable collective mode of instability is a new discovery. Furthermore, it is shown to have the lowest threshold in most cases. The presence of absolute instability with a low threshold renders the TPD an inherently nonlinear problem.

The linear stability of multibeam TPD can be investigated by solving a linearized equation for the envelope of the electrostatic field:^{9,10}

$$\begin{aligned} & \nabla \cdot \left[2i\omega_{pe}(D_t + \nu_e \circ) + 3v_e^2 \nabla^2 - \omega_{pe}^2 \delta N / n_0 \right] \vec{E}_1 \\ & = \frac{e}{4m_e} \nabla \cdot \left[\nabla (\vec{E}_0 \cdot \vec{E}_1^*) - \vec{E}_0 \nabla \cdot \vec{E}_1^* \right] e^{-i\Omega t} + S_E. \end{aligned} \quad (1)$$

The quantity \vec{E}_1 is the complex temporal envelope of the real electrostatic field $\vec{E} = 1/2 [\vec{E}_1(\vec{x}, t) \exp(-i\omega_{pe}t) + \text{c.c.}]$, where enveloping is carried out at the plasma frequency $\omega_{pe} = (4\pi n_0 e^2 / m_e)^{1/2}$ evaluated at the density $n_0 = 0.23 n_c$. In Eq. (1), $D_t \equiv (\partial_t + \vec{u}_0 \cdot \nabla)$ is the convective derivative for a plasma with the flow velocity \vec{u}_0 ($= 0$ here). In the absence of EM pump waves, the free solutions to Eq. (1) are LW's that propagate in a density profile whose deviation from n_0 is given by δN ($\delta N \ll n_0$). [It has been assumed that the inhomogeneity is linear ($\delta N = n_0 x / L_n$) and the direction of its gradient defines the x axis.] LW's of wave number k have the group velocity $V_g = 3k v_e^2 / \omega_{pe}$, where $v_e = \sqrt{T_e / m_e}$ is the electron thermal velocity, and their amplitudes damp at the rate $\nu_e = \nu_{\text{coll}} + \gamma_L$, which is the sum of the collisional ν_{coll} and Landau-damping

γ_L contributions. The EM field corresponding to the incident laser light is enveloped around twice ω_{pe} and further decomposed into N , coherent, linearly polarized plane waves $\vec{E}_0 = \sum_{i=1}^N \vec{E}_{0,i} \exp i(\vec{k}_{0,i} \cdot \vec{x} - \Omega_i t)$ having frequencies $\omega_{0,i}$, wave vectors $\vec{k}_{0,i}$, and vacuum intensities $I_i = c |\vec{E}_{0,i}|^2 / (8\pi)$. The quantity $\Omega_i = \omega_{0,i} - 2\omega_{pe}$ represents the mismatch for each beam, where $\max(|\Omega_i|) \ll 2\omega_{pe}$. The first term on the right-hand side of Eq. (1) is the longitudinal part of the nonlinear current, which is the origin of TPD. The term S_E is a time-random-phase Čerenkov noise source that has been described in Russell *et al.*¹⁰

A series of numerical calculations were carried out to solve Eq. (1) on a uniform $1024 \times 512 \times 512$ Cartesian grid (in the x , y , and z directions, respectively) using a 3-D generalization of the pseudospectral method that has been described previously.^{9,10} In these calculations, the electron temperature and density scale length were held constant ($T_e = 2$ keV, $L_n = 150 \mu\text{m}$), while the total overlapped intensities $I_{\text{tot}} (\equiv \sum_{i=1}^N I_i)$ was varied for various configurations of $N = 1, 2, 4$, and 6 beams of $0.351\text{-}\mu\text{m}$ -wavelength light. For each beam configuration, the single-beam intensities I_i and frequencies $\omega_{0,i}$ were taken to be equal to one another, and the beam wave vectors were distributed symmetrically to fall on the surface of a right circular cone with a 27° half-angle whose cone axis defines the x direction (see e.g., inset to Fig. 138.29). This choice of wave vectors was made because beams are distributed in well-defined cones on large laser systems such as OMEGA¹¹ and the NIF.¹² The simulation box length in the density-gradient direction (x) was chosen to include densities in the range of 0.19 to $0.27 n_c$ ($L_x = 52 \mu\text{m}$). The length in the two transverse dimensions was chosen to be $L_y = L_z = 26 \mu\text{m}$.

Figure 138.28 shows a two-dimensional (2-D) slice of the LW intensity spectrum $|E_1(\vec{k}, t)|^2$ in the $k_z = 0$ plane during the linear growth phase (averaged over times $t = 2.4$ to 4.2 ps) for a two-beam ($N = 2$) calculation. The EM wave vectors and electric-field vectors (polarization) of the two beams lie in this plane, which is the plane of maximum growth. The overlapped intensity $I_{\text{tot}} = 6 \times 10^{14} \text{ W/cm}^2$ was chosen to be above the numerically determined threshold for absolute growth. In Fig. 138.28, the bright “doublets” at the spectral locations centered on wave vectors $\vec{k} \approx (0.8, \pm 0.4, 0)k_0$ and $\vec{k} \sim (0, 0, 0)$ correspond to temporally unstable (growing) decay modes that are resonant at $n_e = 0.238 n_c$. This occurs even though each beam is individually below the threshold for absolute growth.¹³ This cooperative mode of absolutely unstable TPD is analogous to the absolutely unstable modes seen in single-beam TPD, where the pump decays into one LW with $\vec{k} \sim \vec{k}_0$

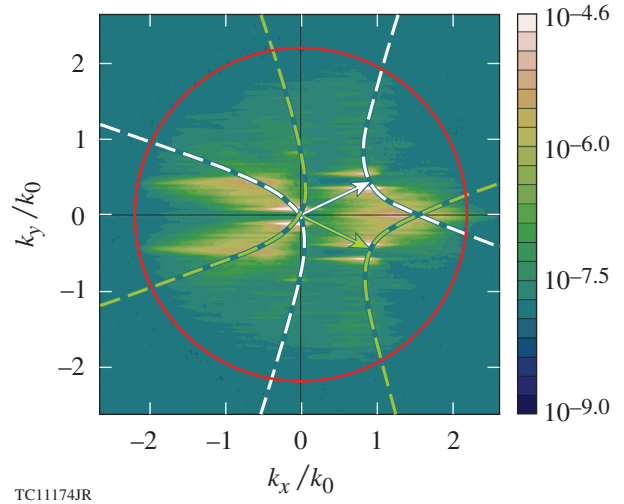
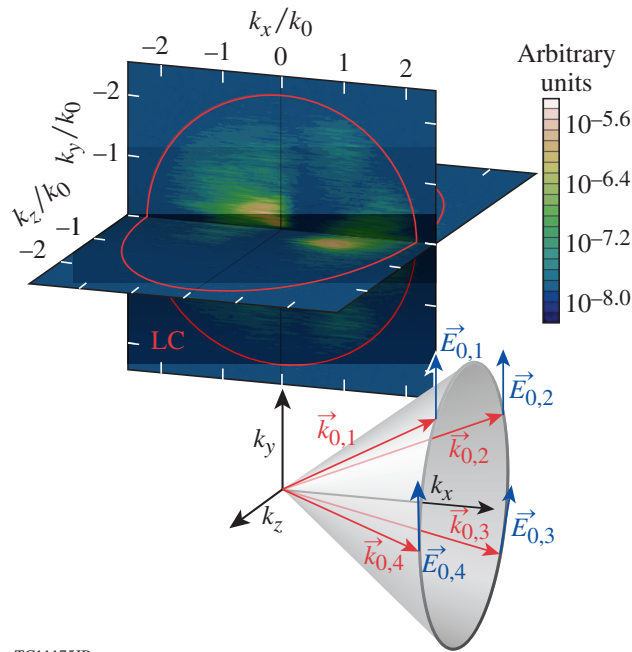


Figure 138.28

The Langmuir wave (LW) spectrum $\langle |E_1(k_x, k_y, k_z = 0, t)|^2 \rangle_t$ averaged over times $t = 2.4$ to 4.2 ps. The two electromagnetic (EM) wave vectors $\vec{k}_{0,1}$ (green arrow) and $\vec{k}_{0,2}$ (white arrow) and their polarization vectors lie in the plane shown ($k_z = 0$) (i.e., p polarization). The dashed green (white) hyperbolas correspond to the maximum single-beam homogeneous growth rate for Beam 1 (2) and the red circle is the Landau cutoff $|\vec{k}| \lambda_{De} = 0.25$ (see the text for the remaining parameters).

and another with $\vec{k} = \pm \vec{k}_\perp$, where $\vec{k}_\perp \ll \vec{k}_0$. In the two-beam case, cooperation occurs because the long-wavelength decays near $\vec{k} \approx (0, 0, 0)$ can be shared between beams. The other local maxima in $|E_1(\vec{k}, t)|^2$ located near $\vec{k} = (1.5, 0, 0)k_0$ and $\vec{k} = (-0.6, \pm 0.4, 0)k_0$ are convectively saturated (i.e., not growing) decays that are resonant at $n_e = 0.245 n_c$. These correspond to convective multibeam common waves that have been described previously^{6,14} and the “triad” modes discussed in Refs. 10, 15, and 16. The convective gain is greatest for spectral locations where the single-beam homogeneous growth-rate curves (dashed hyperbolas in Fig. 138.28) intersect [the maxima at $\vec{k} = (-0.6, \pm 0.4, 0)k_0$ correspond to the daughter waves that are not shared]. The maximum convective gain at the absolute threshold intensity has been computed numerically by estimating the enhancement of the saturated wave intensity above the steady-state noise level supported by S_E in Eq. (1). The behavior described above for two beams is quite generic. Figure 138.29 shows $|E_1(\vec{k}, t)|^2$ on the planes $k_y = 0$ and $k_z = 0$ for a four-beam calculation for the same plasma conditions as in Fig. 138.28. The beams are polarized predominantly in the y direction (signified by the symbol “ \parallel ”) as shown in the inset. The absolutely unstable modes are not restricted to a single plane. The bright spectral features near $\vec{k} = (1.0, 0 \pm 0.4)k_0$ and $\vec{k} = (-0.2, \pm 0.2, 0)k_0$ are temporally unstable and are again absolute multibeam modes. The other features in the

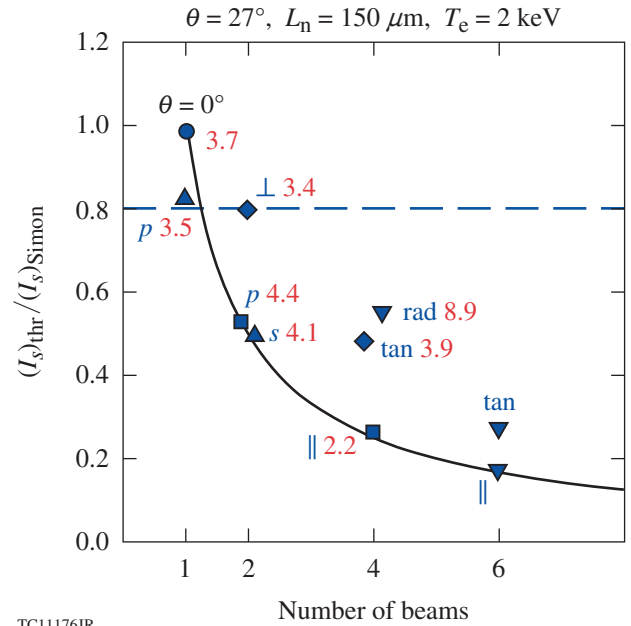


TC11175JR

Figure 138.29 Slices of the LW spectrum $\langle |E_1(\vec{k}, t)|^2 \rangle_t$ (averaged over times $t = 1.0$ to 2.0 ps) in the planes $k_y = 0$ and $k_z = 0$ for a four-beam calculation (\parallel polarization). The beam geometry and polarization are shown in the inset.

spectrum are convectively saturated. The red circles indicate the Landau cutoff.

The threshold intensity for the onset of absolute instability is found by first extracting the growth rate of the most-unstable mode, which does not saturate convectively, for a range of intensities and then finding the intensity corresponding to zero growth by extrapolation. The thresholds for collective absolute TPD instability for various configurations of $N = 1, 2, 4,$ and 6 beams are summarized in Fig. 138.30. For each configuration, there are multiple possibilities for the polarization state: “ p ” and “ s ” correspond to the one- and two-beam configurations, where the polarization is in, or out of, the plane of incidence, respectively; “ rad ” and “ tan ” refer to polarizations where the electric-field vectors are either radially or tangentially oriented with respect to the circle that forms the base of the cone containing the beam wave vectors (see inset to Fig. 138.29); the state signified as “ \parallel ” has been defined above. The thresholds have been quantified by normalizing the intensity of an individual beam for a given configuration $I_s = I_{tot}/N$ by the independent (single) beam absolute threshold given by Simon *et al.*¹³ For one beam ($N = 1$) at normal incidence ($\theta = 0^\circ$), the Simon threshold¹³ is recovered (as expected). [Notice that the threshold is lowered when the angle of incidence is increased to $\theta = 27^\circ$ (triangular marker for $N = 1$ in Fig. 138.30). The effect of



TC11176JR

Figure 138.30 Normalized single-beam threshold intensities $(I_s)_{thr}$ for absolute instability with irradiation by N beams of incidence angle $\theta_s = 27^\circ$ (except where indicated) for various polarization states (see text). The red numbers are the maximum convective gains evaluated at the absolute threshold.

oblique incidence was not described in Ref. 13 and we defer a discussion of this effect to a future publication.] The cooperative nature of the instability is revealed for $N = 2$: for both s and p polarizations, the individual (single) beam intensity at threshold $(I_s)_{thr}$ is significantly lower than the expected independent beam value (dashed line)—the importance of the effect increasing with the number of beams. Rotating the polarizations of the two beams so as to be orthogonal (“ \perp ” in Fig. 138.30) eliminates the cooperation. *The overlapping beams are parametrically unstable (absolutely) even though the threshold intensity for individual beams is not exceeded.* The solid curve indicates maximum cooperation (where the collection of beams effectively acts as a single beam with the combined intensity). The numerically estimated maximum gains of the convectively saturated common modes (cf., e.g., Fig. 138.28) at the onset of absolute instability are shown in red. These gains are consistent with earlier work.^{6,17,18} In most cases, this gain G is small ($G \lesssim 2\pi$), meaning that *the threshold for the collective absolute instability is lower than that for the convective common waves.* The regime of linear spatial amplification is therefore very restricted. Above the absolute threshold there exists a competition between the two modes of cooperative instability, which can be addressed by only a nonlinear theory.

The dominant mechanisms thought to be responsible for the nonlinear saturation of TPD [weak turbulence effects such as the Langmuir decay instability (LDI),^{8,19} profile modification,⁸ and the strong turbulence effects of cavitation and LW collapse¹⁰] are accounted for by the substitution $\delta N \rightarrow \delta N + \delta n$ in Eq. (1), where the low-frequency plasma response δn evolves according to

$$(D_t^2 + 2\nu_i \circ D_t - c_s^2 \nabla^2) \delta n = \frac{Z}{16\pi m_i} \nabla^2 \left(|\vec{E}_1|^2 + \frac{1}{4} |\vec{E}_0|^2 \right). \quad (2)$$

Here $c_s = (ZT_e/m_i)^{1/2} (1 + 3T_i/ZT_e)^{1/2}$ is the speed of ion-acoustic waves that damp with the rate ν_i , where m_i , T_i , and Z are the ion mass, temperature, and charge, respectively. The first term on the right-hand side describes the low-frequency ponderomotive forces of Langmuir and electromagnetic fluctuations. Together, Eq. (1), the substitution $\delta N \rightarrow \delta N + \delta n$, and Eq. (2) constitute the extended Zakharov model of TPD, previously described in Refs. 9, 10, 16, and 20, and are now generalized to three dimensions. In the context of this turbulence model where the initial ion-acoustic noise is negligible [i.e., no noise term in Eq. (2)], three regimes of cooperative TPD behavior have been identified: (1) $\tilde{I} [\equiv I_s/(I_s)_{\text{thr}}] < \tilde{I}_{\text{abs}}$ [\tilde{I}_{abs} is the threshold for collective absolute instability (Fig. 138.30)], where the LW spectrum is dominated by large- k common waves whose intensities are amplified spatially by a gain, which is numerically determined to be small $G \lesssim 3$ to 5 (red numbers in Fig. 138.30) and consistent with the standard Rosenbluth expression;⁶ (2) $\tilde{I} \gg \tilde{I}_{\text{abs}}$ —all unstable modes grow and saturate nonlinearly (the nonlinear development in this case has been described in terms of cavitating Langmuir turbulence and investigated in Ref. 16); and (3) the intermediate regime $\tilde{I} \gtrsim \tilde{I}_{\text{abs}}$. The intermediate regime is of direct relevance to spherical and planar target experiments at the Omega Laser Facility,^{6,21,22} and it displays interesting physical effects.

Figure 138.31 shows the nonlinear temporal development of the LW intensity for the two-beam p -polarized case in the intermediate regime ($\tilde{I} \gtrsim 1$) (same parameters as Fig. 138.28). The other cases shown in Fig. 138.30 exhibit very similar behavior and are not shown. The transverse (y,z) average of the LW intensity $\langle |\vec{E}_1|^2 \rangle_{y,z}(x,t)$ is shown as a function of the x coordinate and time. At early times, growth is linear. The LW Fourier spectrum during this phase (indicated by the lower shaded region) is shown in Fig. 138.28. The previously identified absolute and convective cooperative modes occur at different spatial locations (densities), as indicated by the blue and red dashed lines, are $n_e/n_c = 0.283, 0.245$ in the figure, respectively. The blue (red) dashed vertical lines indicate the evolution of the absolute (convective) modes as a function of time (see inset). At

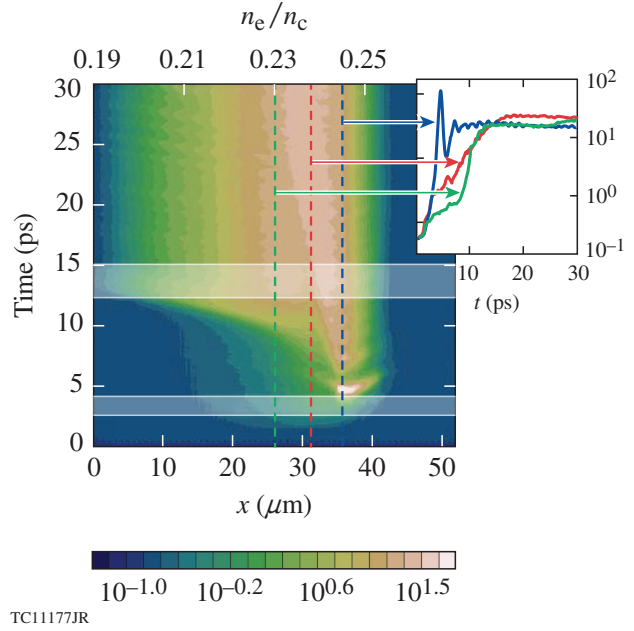
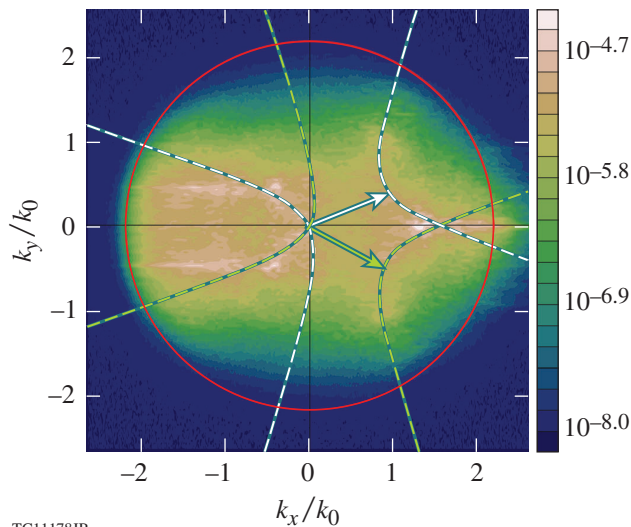


Figure 138.31

The transverse averaged LW intensity $\langle |\vec{E}_1|^2 \rangle_{y,z}(x,t)$ as a function of the x coordinate (initial density, upper axis) and time. The inset shows the temporal dependence of $\langle |\vec{E}_1|^2 \rangle_{\perp}(x,t)$ at the locations $x = 26 \mu\text{m}$ (dashed green line), $x = 31 \mu\text{m}$ (dashed red line), and $x = 36 \mu\text{m}$ (dashed blue line).

approximately $t = 5$ ps, the absolutely unstable modes saturate nonlinearly, producing large density-profile modifications and radiating large-amplitude LW's. These waves propagate down the density profile [toward lower densities (smaller x)] with time, generating a wave of turbulence (consistent with previous studies) whose effects can be seen in the figure. When this turbulence reaches a particular location, growth is restored to the modes that were previously convectively saturated (for $x = 26 \mu\text{m}$, this occurs at $t \sim 10$ ps). This was verified by performing a linear analysis on the perturbed profiles. The restoration of absolute growth in a convectively unstable parametric instability (i.e., fragility of the Rosenbluth result) caused by noise or turbulence has been noted previously (cf., e.g., Ref. 23). Here, it is triggered by the nonlinearity of the absolute instability. The result is that, at late times (e.g., the upper shaded region in the figure), the LW spectrum is much broader and more intense (see Fig. 138.32) than during the linear phase (Fig. 138.28). *The late-time turbulent spectrum is dominated by large- k shared (common) modes with intensities that are greatly in excess of those predicted by the linear analysis.*

These results will be of fundamental importance to direct-drive ICF experiments on the NIF, where many laser beams overlap on the target (and a knowledge of TPD stability prop-



TC11178JR

Figure 138.32

The electric-field spectrum $|E_1(\vec{k}, t)|^2$ (averaged over $t = 12$ to 15 ps) shown in the $k_z = 0$ plane for the parameters of Fig. 138.28.

erties is essential) and are an important contribution to understanding cooperative parametric instabilities in general. The results obtained with this model may provide an interpretation of experiments that infer the coexistence of large- and small-wave-number TPD LW's via half- and three-halves-harmonic emission.^{22,24} They might also explain the observation of strong TPD hot-electron production in multibeam OMEGA EP experiments, even though the predicted common-wave convective gains are small.^{6,25}

ACKNOWLEDGMENT

This material is based upon work supported by the Department of Energy National Nuclear Security Administration under Award Number DE-NA0001944, the University of Rochester, and the New York State Energy Research and Development Authority. The support of DOE does not constitute an endorsement by DOE of the views expressed in this article.

REFERENCES

1. J. Nuckolls *et al.*, *Nature* **239**, 139 (1972).
2. J. D. Lindl, *Inertial Confinement Fusion: The Quest for Ignition and Energy Gain Using Indirect Drive* (Springer-Verlag, New York, 1998).
3. R. P. Drake, *High-Energy-Density Physics: Fundamentals, Inertial Fusion, and Experimental Astrophysics*, Shock Wave and High Pressure Phenomena (Springer, Berlin, 2006).
4. D. F. DuBois *et al.*, *Phys. Plasmas* **8**, 791 (2001); P. Y. Cheung *et al.*, *Phys. Plasmas* **8**, 802 (2001).
5. M. J. Edwards, P. K. Patel, J. D. Lindl, L. J. Atherton, S. H. Glenzer, S. W. Haan, J. D. Kilkenny, O. L. Landen, E. I. Moses, A. Nikroo, R. Petrasso, T. C. Sangster, P. T. Springer, S. Batha, R. Benedetti, L. Bernstein, R. Betti, D. L. Bleuel, T. R. Boehly, D. K. Bradley, J. A. Caggiano, D. A. Callahan, P. M. Celliers, C. J. Cerjan, K. C. Chen, D. S. Clark, G. W. Collins, E. L. Dewald, L. Divol, S. Dixit, T. Doeppner, D. H. Edgell, J. E. Fair, M. Farrell, R. J. Fortner, J. Frenje, M. G. Gatu Johnson, E. Giraldez, V. Yu. Glebov, G. Grim, B. A. Hammel, A. V. Hamza, D. R. Harding, S. P. Hatchett, N. Hein, H. W. Herrmann, D. Hicks, D. E. Hinkel, M. Hoppe, W. W. Hsing, N. Izumi, B. Jacoby, O. S. Jones, D. Kalantar, R. Kauffman, J. L. Kline, J. P. Knauer, J. A. Koch, B. J. Kozioziemski, G. Kyrala, K. N. LaFortune, S. Le Pape, R. J. Leeper, R. Lerche, T. Ma, B. J. MacGowan, A. J. MacKinnon, A. Macphee, E. R. Mapoles, M. M. Marinak, M. Mauldin, P. W. McKenty, M. Meezan, P. A. Michel, J. Milovich, J. D. Moody, M. Moran, D. H. Munro, C. L. Olson, K. Opachich, A. E. Pak, T. Parham, H.-S. Park, J. E. Ralph, S. P. Regan, B. Remington, H. Rinderknecht, H. F. Robey, M. Rosen, S. Ross, J. D. Salmonson, J. Sater, D. H. Schneider, F. H. Séguin, S. M. Sepke, D. A. Shaughnessy, V. A. Smalyuk, B. K. Spears, C. Stoeckl, W. Stoeffl, L. Suter, C. A. Thomas, R. Tommasini, R. P. Town, S. V. Weber, P. J. Wegner, K. Widman, M. Wilke, D. C. Wilson, C. B. Yeaman and A. Zylstra, *Phys. Plasmas* **20**, 070501 (2013).
6. D. T. Michel, A. V. Maximov, R. W. Short, S. X. Hu, J. F. Myatt, W. Seka, A. A. Solodov, B. Yaakobi, and D. H. Froula, *Phys. Rev. Lett.* **109**, 155007 (2012).
7. V. A. Smalyuk, D. Shvarts, R. Betti, J. A. Delettrez, D. H. Edgell, V. Yu. Glebov, V. N. Goncharov, R. L. McCrory, D. D. Meyerhofer, P. B. Radha, S. P. Regan, T. C. Sangster, W. Seka, S. Skupsky, C. Stoeckl, B. Yaakobi, J. A. Frenje, C. K. Li, R. D. Petrasso, and F. H. Séguin, *Phys. Rev. Lett.* **100**, 185005 (2008); V. N. Goncharov, T. C. Sangster, P. B. Radha, R. Betti, T. R. Boehly, T. J. B. Collins, R. S. Craxton, J. A. Delettrez, R. Epstein, V. Yu. Glebov, S. X. Hu, I. V. Igumenshchev, J. P. Knauer, S. J. Loucks, J. A. Marozas, F. J. Marshall, R. L. McCrory, P. W. McKenty, D. D. Meyerhofer, S. P. Regan, W. Seka, S. Skupsky, V. A. Smalyuk, J. M. Soures, C. Stoeckl, D. Shvarts, J. A. Frenje, R. D. Petrasso, C. K. Li, F. Séguin, W. Manheimer, and D. G. Colombant, *Phys. Plasmas* **15**, 056310 (2008).
8. H. X. Vu, D. F. DuBois, J. F. Myatt, and D. A. Russell, *Phys. Plasmas* **19**, 102703 (2012).
9. D. F. DuBois, D. A. Russell, and H. A. Rose, *Phys. Rev. Lett.* **74**, 3983 (1995).
10. D. A. Russell and D. F. DuBois, *Phys. Rev. Lett.* **86**, 428 (2001).
11. T. R. Boehly, D. L. Brown, R. S. Craxton, R. L. Keck, J. P. Knauer, J. H. Kelly, T. J. Kessler, S. A. Kumpan, S. J. Loucks, S. A. Letzring, F. J. Marshall, R. L. McCrory, S. F. B. Morse, W. Seka, J. M. Soures, and C. P. Verdon, *Opt. Commun.* **133**, 495 (1997).
12. E. I. Moses *et al.*, *Phys. Plasmas* **16**, 041006 (2009); E. I. Moses, *Fusion Sci. Technol.* **54**, 361 (2008); W. J. Hogan, E. I. Moses, B. E. Warner, M. S. Sorem, and J. M. Soures, *Nucl. Fusion* **41**, 567 (2001); J. A. Paisner, E. M. Campbell, and W. J. Hogan, *Fusion Technol.* **26**, 755 (1994).
13. A. Simon, R. W. Short, E. A. Williams, and T. Dewandre, *Phys. Fluids* **26**, 3107 (1983).
14. D. T. Michel, A. V. Maximov, R. W. Short, J. A. Delettrez, D. Edgell, S. X. Hu, I. V. Igumenshchev, J. F. Myatt, A. A. Solodov, C. Stoeckl, B. Yaakobi, and D. H. Froula, *Phys. Plasmas* **20**, 055703 (2013).

15. H. X. Vu, D. F. DuBois, D. A. Russell, and J. F. Myatt, *Phys. Plasmas* **19**, 102708 (2012).
16. H. X. Vu, D. F. DuBois, D. A. Russell, J. F. Myatt, and J. Zhang, "Nonlinear Development of the Two-Plasmon Decay Instability in Three Dimensions," to be published in *Physics of Plasmas*.
17. R. Yan, A. V. Maximov, and C. Ren, *Phys. Plasmas* **17**, 052701 (2010).
18. M. N. Rosenbluth, *Phys. Rev. Lett.* **29**, 565 (1972).
19. D. F. DuBois and M. V. Goldman, *Phys. Rev.* **164**, 207 (1967).
20. J. F. Myatt, H. X. Vu, D. F. DuBois, D. A. Russell, J. Zhang, R. W. Short, and A. V. Maximov, *Phys. Plasmas* **20**, 052705 (2013).
21. C. Stoeckl, R. E. Bahr, B. Yaakobi, W. Seka, S. P. Regan, R. S. Craxton, J. A. Delettrez, R. W. Short, J. Myatt, A. V. Maximov, and H. Baldis, *Phys. Rev. Lett.* **90**, 235002 (2003).
22. W. Seka, D. H. Edgell, J. F. Myatt, A. V. Maximov, R. W. Short, V. N. Goncharov, and H. A. Baldis, *Phys. Plasmas* **16**, 052701 (2009).
23. D. R. Nicholson and A. N. Kaufman, *Phys. Rev. Lett.* **33**, 1207 (1974); G. Laval, R. Pellat, and D. Pesme, *Phys. Rev. Lett.* **36**, 192 (1976); E. A. Williams, J. R. Albritton, and M. N. Rosenbluth, *Phys. Fluids* **22**, 139 (1979).
24. W. Seka, J. F. Myatt, R. W. Short, D. H. Froula, J. Katz, V. N. Goncharov, and I. V. Igumenshchev, "Nonuniformly Driven Two-Plasmon-Decay Instability in Direct-Drive Implosions," to be published in *Physical Review Letters*.
25. P. Michel *et al.*, *Phys. Plasmas* **20**, 056308 (2013).

Near-Ultraviolet Absorption Annealing in HfO₂ Thin Films Subjected to Continuous-Wave Laser Irradiation

Introduction

Hafnium oxide is used in numerous applications as a high-index component in optical coatings for high-power lasers ranging from a near-infrared (IR) to near-ultraviolet (UV) light spectrum. It is also known that for the most frequently used film-pair combination of HfO₂/SiO₂, HfO₂ is the material in which nanosecond-pulse laser damage is initiated.¹ In this context, reduction of absorption in this material is crucial to improving damage performance of the coatings used in mirrors and other laser components. Previous studies² have shown that near-UV absorption in HfO₂ thin films is generated by high-spatial-density (an average separation of 100 nm or less) nanoscale absorbers whose nature is attributed to the agglomeration of electronic defects. Electronic defects exist even in high-quality optical bulk materials, such as crystals and glasses. In thin films, additional absorbing states might exist because of the presence of interfaces and grain boundaries. There are very limited ways to influence the concentration of the absorbing states once the thin film is deposited. Thermal annealing^{3,4} is the process most frequently used as a research tool, but there are obvious practical limitations for optical parts used in large-scale lasers. Irradiation by pulsed laser radiation at fluences below damage threshold (also called laser conditioning) is another widely used method.

In this work we explore the possibility of using continuous-wave (cw)-laser radiation with power densities in the range of 50 kW/cm² to >1 MW/cm² to anneal absorption in HfO₂ monolayer films in the near-UV spectral range. We also investigate the absorption-annealing impact on pulsed-laser-damage behavior of HfO₂ monolayers subjected to irradiation by 351-nm, 0.9-ns pulses and 1053-nm, 600-fs pulses.

Experimental

A HfO₂ monolayer film with a 180-nm physical thickness (one wave at 351 nm) was e-beam deposited on a fused-silica substrate on top of a 500-nm-thick SiO₂ film, isolating the HfO₂ film from the substrate defects introduced by the polishing process. The deposition rate was 1.2 Å/s and the oxygen pressure was 8×10^{-5} Torr. For monolayer absorption charac-

terization, we used a photothermal heterodyne imaging (PHI) technique, utilizing pump and probe laser beams focused onto a submicrometer spot on a sample having the same objective. Modulated pump-light absorption inside the sample produces a locally modulated refractive-index variation, which causes probe-light scattering amplified by far-field interference. Using the nanopositioning stage for the sample translation allows one to map absorption of the film sample with a better-than-0.4- μ m spatial resolution. A detailed description of the PHI technique principle and the setup used in this work are given in Refs. 2 and 5.

Near-UV, cw-laser-absorption annealing was studied using either a 351-nm, 1-W Ar⁺ laser or a 355-nm, diode-pumped semiconductor laser that works as a pump laser for PHI and delivers up to 6 mW on the sample. The latter, after being focused into a ≤ 0.7 - μ m [full width at half maximum (FWHM)] spot by a 40 \times /0.95 numerical-aperture (N.A.) objective, produced power densities of up to 1 MW/cm², and the former was focused into a 50- μ m spot ($1/e^2$), resulting in a 46-kW/cm² power density. A sample exposure, in the case of a small laser spot (PHI pump laser), was accomplished by using two different methods. In the first method, the sample position and laser power were fixed and the sample was exposed for some period of time, typically up to 15 min. In this manner, several sample sites were irradiated at a different cw-laser power. The second method consisted of raster-scanning the sample with typical velocities of 1 to 10 μ m/s, producing different exposures by varying the sample velocity and laser power. To quantify the exposure effect at a particular location, another raster scan of the larger area, including the exposed area, was performed with high sample velocity and low laser power to minimize additional energy deposition. In the case of a large laser spot (Ar⁺ laser), the sample was translated in one direction with 1- μ m/s velocity, creating a 50- μ m-wide, several-mm-long exposed area.

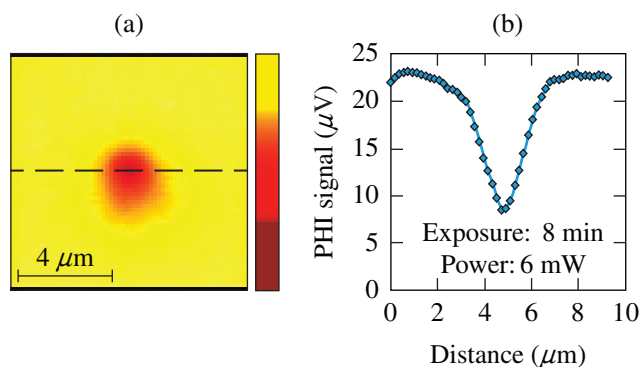
Laser-damage testing of cw-laser exposed and unexposed sample areas was performed in a 1-on-1 regime, using 351-nm, 0.9-ns pulses of a Nd:YLF diode-pumped laser⁶ and 1053-nm, 600-fs, best-compression pulses from a laser using the standard

chirped-pulse–amplification scheme.⁷ Damage testing using 0.9-ns pulses was conducted in an ambient environment and laser testing with 600-fs pulses was performed in a 10^{-7} -Torr vacuum environment to avoid self-focusing in air. The laser-beam spot size ($1/e^2$) on the sample was $400\ \mu\text{m}$ and $270\ \mu\text{m}$ for 0.9-ns and 600-fs beams, respectively. Laser-damage morphology was investigated by means of atomic force microscopy (AFM).

Results and Discussion

1. Absorption-Annealing Effects

Figure 138.33 shows the result of irradiating HfO_2 film for 8 min at a fixed location using a 355-nm, 6-mW beam focused into a submicrometer spot ($\leq 0.7\text{-}\mu\text{m}$, $\sim 1\text{-MW}/\text{cm}^2$ power density). Figure 138.33(a) is a PHI scan of a $10 \times 10\text{-}\mu\text{m}^2$ film area centered around the location of the laser spot. A cross-sectional profile of the PHI signal [Fig. 138.33(b)] shows up to a 70% reduction in absorption within the irradiated spot, which appeared to be permanent when confirmed by PHI scans performed after one week and then one month later. Next, absorption annealing was investigated as a function of laser power and exposure time. Figure 138.34 plots a PHI signal's dependence on exposure time for three different values of laser-beam power: 0.7 mW, 3 mW, and 6 mW. One can see that the main drop in signal takes place during the first minute and is then followed by a slow decline on an ~ 10 - to 15-min time scale. The initial signal drop becomes faster and deeper with increasing laser power. Nevertheless, the temporal behavior of the 6-mW and 3-mW curves shows that at long exposures, the signal can eventually be stabilized at the same level. It suggests that within some range of power densities, overall absorption reduction is proportional to both power density and exposure time or, in different terms, locally deposited energy.

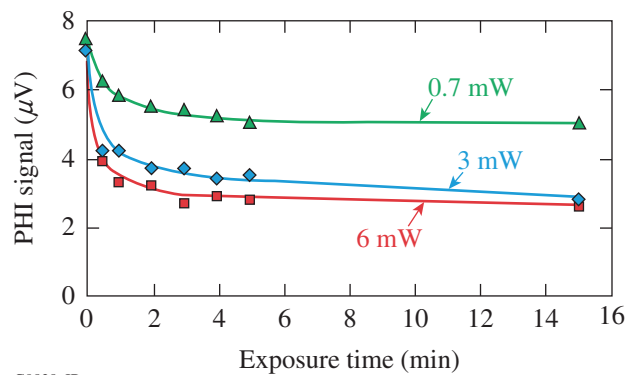


G9829aJR

Figure 138.33

(a) A photothermal heterodyne imaging (PHI) map of a $10 \times 10\text{-}\mu\text{m}^2$ film area and (b) the signal horizontal profile through the central spot irradiated by a 355-nm, 6-mW cw laser for 8 min.

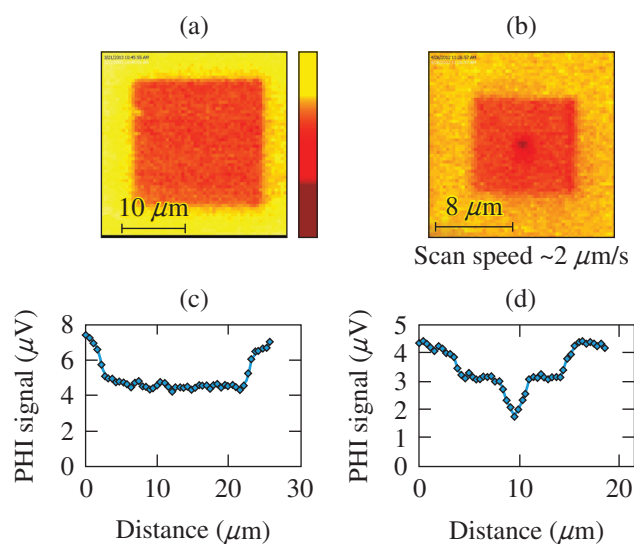
In an attempt to demonstrate the possibility of annealing absorption within a sample area larger than the laser spot, we performed square raster scans with linear dimensions of several tens of micrometers. Figure 138.35 shows corresponding PHI images, each obtained as a result of two scans. In the first image [Fig. 138.35(a)] the central $20 \times 20\text{-}\mu\text{m}$ part was initially scanned with a high laser power of 4.5 mW and a low



G9828aJR

Figure 138.34

Temporal behavior of absorption as a function of cw-laser power on sample.



G9830aJR

Figure 138.35

PHI maps resulting from 355-nm cw-laser annealing by means of raster-scanning with a low, $1\text{-}\mu\text{m}/\text{s}$ sample velocity: (a) a $30 \times 30\text{-}\mu\text{m}^2$ area with the central $20 \times 20\text{-}\mu\text{m}^2$ part exposed using 4.5-mW laser power; (b) a $20 \times 20\text{-}\mu\text{m}^2$ area with the central $10 \times 10\text{-}\mu\text{m}^2$ part raster-scan exposed, using 6 mW and, in addition, the central spot exposed for 8 min with 6-mW power; [(c) and (d)] horizontal signal profiles taken through the central part of the (a) and (b) maps, respectively.

scan velocity of $\sim 1 \mu\text{m/s}$ to achieve the annealing effect. Subsequently, the larger square area ($30 \times 30 \mu\text{m}^2$), with the same center coordinate, was imaged using a much lower laser power of 1.5 mW and a several-times-higher speed velocity, such that no, or very little, annealing effect was produced by the second scan. A cross-section horizontal-signal profile revealed at least a 40% reduction in absorption within the initially scanned area. A similar procedure was used for the $20 \times 20\text{-}\mu\text{m}$ image shown in Fig. 138.35(b), with the only difference being that the central spot was exposed for an additional 8 min using 6 mW of laser power. In this case, the horizontal signal profile shows a 70% reduction in absorption in the central spot. From a practical point of view, it should be noted that because of the scan-velocity and beam-size limitations (the latter defines the maximum separation between two consecutive scan lines, or minimum number of lines per scan), raster-scanning for annealing purposes is very time consuming. For example, it takes at least 2 h to complete a $60 \times 60\text{-}\mu\text{m}$ scan using a $1\text{-}\mu\text{m/s}$ scan velocity.

The question to be addressed is the possibility of scaling up the absorption-annealing process for HfO_2 films used in optical parts for laser applications. In this work, we explored the possibility of producing absorption annealing in a mm^2 -scale area using a cw Ar^+ laser having a maximum 351-nm output power of 1 W. In this case, a laser beam having a power of ~ 900 mW was focused onto a $50\text{-}\mu\text{m}$ -diam ($1/e^2$) spot on the sample, which was slowly ($\sim 1 \mu\text{m/s}$) linearly translated for a distance of 3.6 mm. Despite a much lower power maximum density of 46 kW/cm^2 , as compared to $\sim 1 \text{ MW/cm}^2$ in the case of a small PHI pump laser spot, a much longer (at least $50\times$) exposure time allowed us to achieve an almost 50% absorption reduction (see Fig. 138.36) in the film area of $\sim 0.2 \text{ mm}^2$.

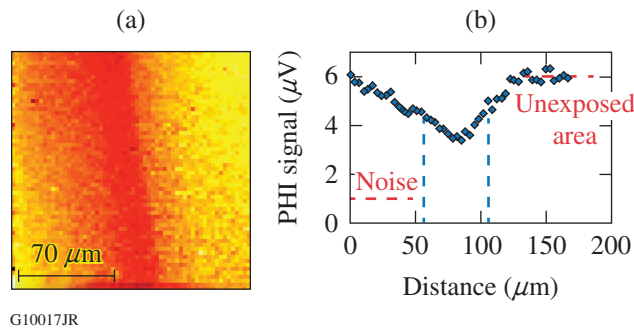


Figure 138.36
(a) A $180\text{-}\mu\text{m}$ PHI scan and (b) corresponding horizontal signal profile of the HfO_2 film area irradiated by a 900-mW Ar^+ laser. The sample vertical travel velocity was $1 \mu\text{m/s}$.

2. Laser-Damage Performance of Annealed HfO_2 Films

a. Nanosecond-pulse damage. Laser-damage performance of thin films is usually strongly linked to the absorption properties of the film material and, therefore, can provide a true measure of absorption annealing. In this work, damage thresholds and damage morphology were investigated for cw-laser-annealed film areas and then compared to the damage behavior of unexposed, as-produced film areas. As a starting point, we conducted AFM imaging of the cw-laser-annealed film columnar structure, which was then compared to the columnar structure of the unexposed film. High-resolution ($\sim 7\text{-nm}$) AFM images of these two areas (see Fig. 138.37) revealed no modification caused by the near-UV, cw-laser exposure with power densities up to $\sim 1 \text{ MW/cm}^2$, implying that local heating of the material produced temperatures well below the HfO_2 melting point.

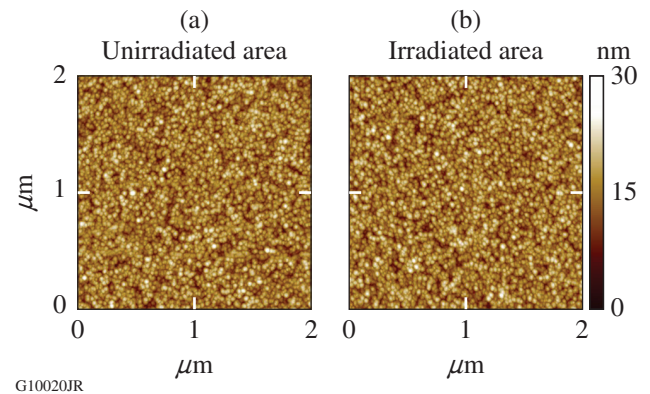


Figure 138.37
Atomic force microscopy (AFM) images ($2 \times 2 \mu\text{m}$) of cw-laser (a) unirradiated and (b) irradiated HfO_2 film areas.

To evaluate the effect of absorption annealing on HfO_2 film-damage resistance, a series of $20 \times 20\text{-}\mu\text{m}$ cw-laser-exposed areas were produced on a sample and then irradiated by a pulsed laser (351 nm, 0.9 ns) at fluences exceeding damage threshold. Figure 138.38 depicts an optical micrograph of such a film area irradiated by a 351-nm, 0.9-ns pulse with a peak fluence $\sim 30\%$ above the threshold. A square-shaped unaffected area where cw-laser exposure was carried out is clearly visible inside the damaged zone. Laser-fluence estimates show an $\sim 25\%$ increase in damage threshold within the film area subjected to annealing, which unambiguously proves that absorption is reduced in cw-laser-exposed film.

A high-resolution AFM map (see Fig. 138.39) of the sample site, shown earlier in Fig. 138.38, provides additional information on annealing's impact on absorption sources in film material. Taking into account that damage morphology is rep-

resented by isolated craters, crater-depth distribution provides a rough approximation for the localized absorber distribution within the sample material. The crater-depth distribution was measured for the damage-site area adjacent to the exposed area [Fig. 138.39(b)], which should provide a reasonable estimate of the initial absorber distribution within the exposed material.

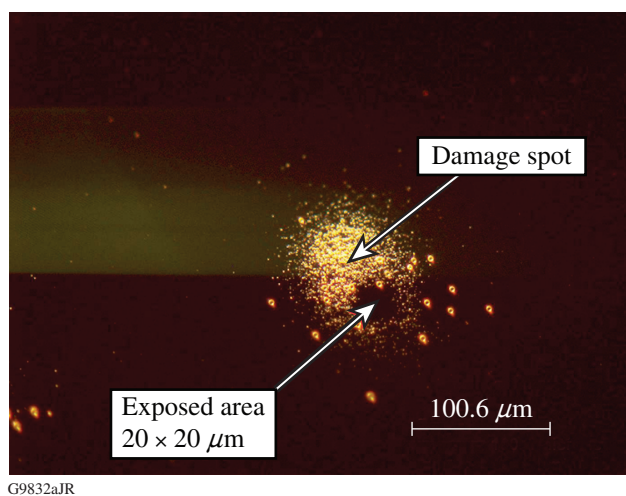
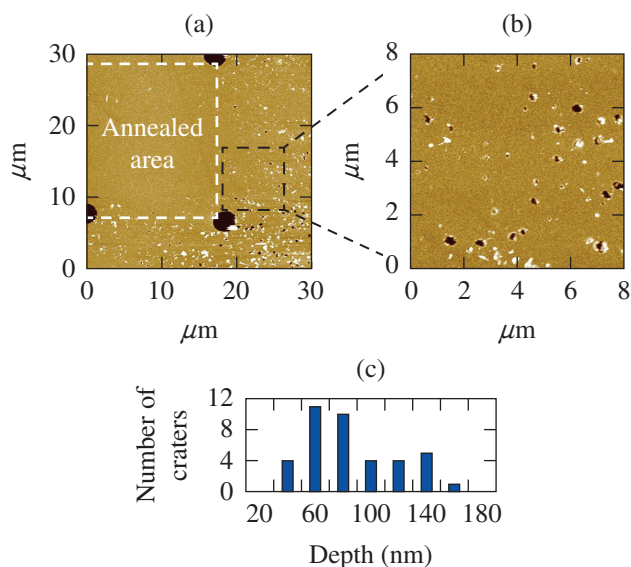


Figure 138.38

An optical micrograph of an HfO_2 film site damaged by a 351-nm, 0.9-ns single pulse. Damage morphology clearly shows a damage-free, $\sim 20 \times 20\text{-}\mu\text{m}^2$ square area subjected to exposure by a 6-mW, 355-nm cw laser.



G10016JR

Figure 138.39

(a) A $30 \times 30\text{-}\mu\text{m}$ AFM scan of a nanosecond-pulse damaged film site, including part of a cw-laser-exposed area. (b) A higher-resolution, $8 \times 8\text{-}\mu\text{m}$ scan showing damage craters bordering an undamaged cw-laser-irradiated area. (c) Crater-depth distribution confirming the location of absorption sources inside the 180-nm-thick HfO_2 film.

One can see that the crater depth does not exceed the 180-nm depth that equals the thickness of the HfO_2 layer. This result indicates that annealed absorption precursors are indeed located inside HfO_2 film and not in SiO_2 film or the substrate.

b. Short-pulse (600-fs) damage. Previous studies⁸ suggest that electronic defects might also play a role for short-pulse (picosecond, femtosecond) laser damage. In this context, the possible impact of the cw-laser annealing of the absorption precursors on short-pulse damage performance is of interest. Similar to the nanosecond-pulse study, near-UV, cw-laser irradiation of HfO_2 film was conducted utilizing both a small spot ($\leq 0.7\ \mu\text{m}$) of a PHI laser and a $50\text{-}\mu\text{m}$ spot of an Ar^+ laser. The results of 1053-nm, 600-fs-pulse damage testing of exposed (sites 1 and 2) and unexposed (sites 3 and 4) film areas are presented in Fig. 138.40, showing damage morphologies as recorded by an optical microscope. It is evident that the exposed sites show no damage at all while being irradiated by pulses with fluences above the unexposed film threshold of $3.45\ \text{J}/\text{cm}^2$ (compare sites 1 and 3) or show a smaller extent of damage (site 2 versus site 4) as compared to the unexposed sites. Moreover, as evidenced by the PHI image of damaged site 2 [see Fig. 138.40(b)], the damaging pulse has partially missed the exposed area, which, in the case of a better overlap, could show an even larger difference in the damage scale for sites 2 and 4.

To summarize, near-UV, cw-laser annealing improves the damage resistance of e-beam-deposited HfO_2 films to pulsed laser radiation at both 351 and 1053 nm.

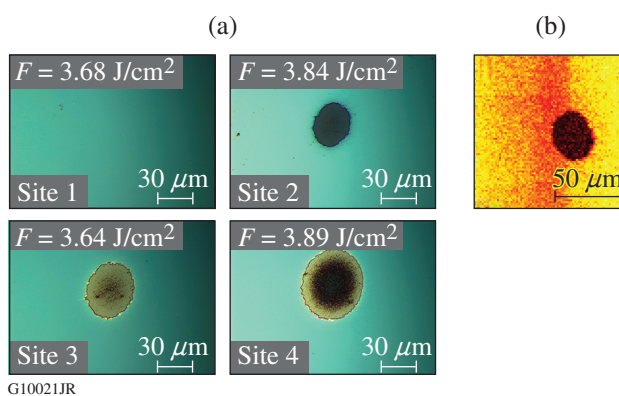


Figure 138.40

(a) Optical micrographs of 600-fs-pulse damage morphology. Sites 1 and 2: cw-laser irradiated; sites 3 and 4: unirradiated. (b) PHI scan of site 2 showing relative positions of the cw-laser-irradiated area and damaging-pulse imprint.

3. Absorption-Annealing Mechanisms

Mechanisms of the near-UV, cw-laser annealing of absorption in HfO₂ films and related improvements in pulsed-laser-damage resistance may be explained if one considers electronic defects as a main source of absorption and damage initiation. Numerous types of defects can exist in HfO₂ bulk material with electronic energy levels located inside the bandgap⁹ and even more are expected to exist for HfO₂ films caused by the columnar film structure. As suggested earlier,² in the case of near-UV, nanosecond-pulse damage, some of these states—as single- and double-ionized oxygen vacancies [V⁺, V²⁺, respectfully (see Fig. 138.41)]—are shallow enough that absorption of 351-nm photons (3.54 eV) can initiate transition of the electron into the conduction band. Further heating of these free electrons by the remaining laser pulse energy can promote electron-avalanche formation and damage. The same defect-energy levels might initiate multiphoton absorption and damage in the case of short, 600-fs pulses at 1053 nm. Assuming the validity of such a damage mechanism, the cw-laser-induced absorption-annealing effect and linked increase in pulsed-laser-damage resistance can be explained by depopulating the absorbing states.

The first possible scenario involves cw-laser-excited electron transition into the conduction band, where the electron spends time of the order of 10 ps (Ref. 8), followed by recombination with holes in the valence band or trapping into the deep defect states in the band gap, as shown in Fig. 138.41. Modeling this scenario using kinetic equations may provide further clarification of the annealing mechanism. This type of study, as well as extending the investigation of cw-laser anneal-

ing from monolayers to multilayer systems, should become the subject of future research.

The second absorption-annealing scenario may be linked to heating the film material resulting from absorption of UV-laser photons. Thermal annealing is widely used to improve the mechanical and optical performance of thin films, including laser-damage resistance in the near UV, as was recently demonstrated¹⁰ for HfO₂ monolayer films at a 355-nm wavelength. In that work, the HfO₂ film temperature was increased by at least 100°C above room temperature to observe the absorption-annealing effect, with maximum effect obtained at an annealing temperature of 300°C. To evaluate possible thermal effects in our study, the temperature distribution in HfO₂ film was modeled with the assumption that all the energy absorbed in the film is released in the form of heat. The energy deposition was considered homogeneous in the cylindrical film volume with a diameter equal to the FWHM diameter of the laser beam (~600 nm) and a height equal to a 180-nm film thickness. The geometry of the model is shown in Fig. 138.42(a). The cw-laser intensity was fixed at 1 MW/cm² (highest used in the experiment), and the energy deposited in the film was varied by changing the film absorption in the range of 10 ppm (parts per million) to 1000 ppm, with an upper absorption boundary (1000 ppm) being well above the film absorption estimated from photothermal measurements. Heat conduction was considered to be the only channel of energy dissipation, and temperature rise in the film was obtained by solving appropriate heat-conduction equations:

$$\rho C \frac{\partial T}{\partial t} = \nabla \kappa \nabla T + S, \quad (1)$$

where ρ , C , and κ are the density, heat capacity, and heat conductivity of the materials, respectively; T is the temperature; and S is the absorbed laser power per unit volume. The material parameters for modeling are listed in Table 138.VII. No reliable data are available for the heat capacity and density values for HfO₂ and SiO₂ films; for that reason, their values were set equal to the bulk values. It should be noted here that these parameters in the cw-laser regime affect only the time necessary to reach peak temperature but not the peak temperature value [as can be seen from Eq. (1) by setting the temperature derivative to zero]. A standard two-dimensional (2-D) cylindrical (five-point spatial), time-explicit finite-difference scheme was used to discretize and solve the heat-conduction equation (see, e.g., Chap. 8 of Ref. 11). The zero heat-flux boundary condition was applied at the film/air interface ($z = 0$), and a zero-temperature boundary condition was applied at the other boundaries of the computational domain, which was chosen to be large enough to

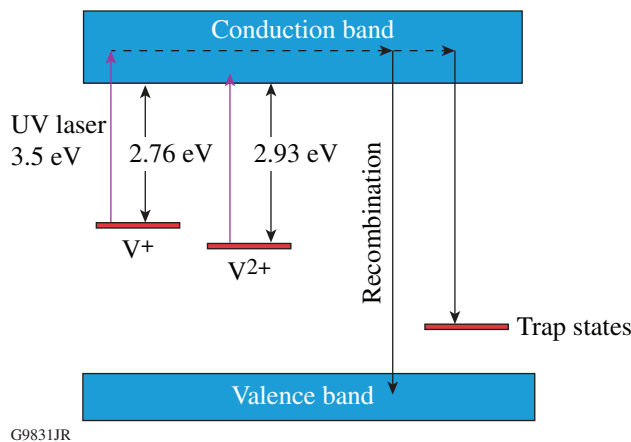
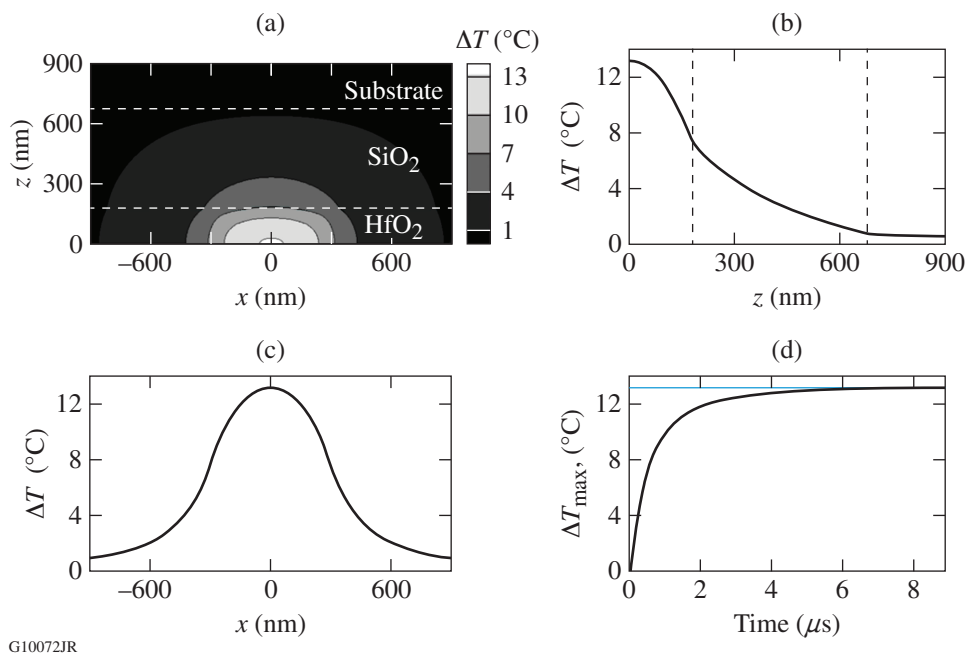


Figure 138.41
HfO₂ energy-level diagram illustrating the possible mechanism of near-UV absorption annealing.



G10072JR

Figure 138.42

Peak temperature-rise distribution in a thin-film sample: (a) modeling geometry and distribution in x - z plane ($y = 0$); (b) lineout along z axis ($y = x = 0$); (c) lineout along x axis ($y = z = 0$); and (d) time evolution of the maximum temperature rise.

Table 138.VII: Parameters used to calculate the rise in HfO₂ film temperature.

	Thermal Conductivity (W/m·K)	Heat Capacity (J/kg·K)	Density (kg/m ³)
HfO ₂ film	0.10	287	9700
SiO ₂ film	0.25	741	2200
Fused-silica substrate	1.38	741	2200

not affect the calculated temperature by more than 0.1°C. The modeling results presented in Fig. 138.42 show that at the highest chosen absorption level of 1000 ppm, the peak temperature rise does not exceed 14°C, which is not enough to produce the absorption-annealing effect. Two-dimensional temperature change distribution is shown in Fig. 138.42(a) along with its lineouts along the axis of symmetry z ($x = y = 0$) in Fig. 138.42(b) and along the x axis ($y = z = 0$) in Fig. 138.42(c). The time evolution of the maximum temperature rise, which is observed along the center of the laser beam at the HfO₂/air interface, $x = y = z = 0$, after the laser is turned on at time $t = 0$, is shown in Fig. 138.42(d). It is worth noting that all these conditions lead to the highest-possible peak film-temperature estimates. Adding energy dissipation channels (such as luminescence or structural transformations) would lead to lower peak tempera-

tures. Consequently, one can conclude that depopulation of the absorbing states is not caused by heat-induced structural matrix transformation.

Finally, it should be noted that irradiation of thin films by cw lasers with power densities used in this work can produce different absorption-modification effects. For instance, in similar experimental conditions,¹² irradiation of TiO₂ monolayer films using an 800-nm cw laser caused an increase in absorption that was also dependent on exposure time. Consequently, absorption-modification effects are thin-film material and cw-laser wavelength specific.

Conclusions

Irradiation of e-beam-deposited HfO₂ monolayer films by near-UV, cw-laser light with power densities of 50 kW/cm² to 1 MW/cm² produced significant modification of near-UV film absorption. A reduction in absorption as high as 70% was achieved in film areas subjected to exposure. The effect is permanent, as confirmed by repeated measurements over a several-month period. It has been shown that absorption modification is achieved without any changes in the film's columnar structure on a spatial scale of up to a few nanometers. This led to the conclusion that a reduction of absorption is linked to the modification of the atomic film structure—in particular, to changes in the concentration of structural

defects responsible for near-UV absorption. Investigation of 351-nm, ns-pulse laser-damage behavior of HfO_2 monolayer films subjected to cw-laser exposure showed a >25% increase in damage thresholds and confirmed that absorption can be reduced by annealing the absorbing defects residing inside the HfO_2 film. Short, 600-fs pulse irradiation also indicated an increase in laser-damage resistance of cw-laser-exposed areas as compared to unexposed areas. This result suggests partial cw-laser annealing of electronic defects participating in the multiphoton absorption process that initiates damage by 600-fs pulses. Future research will concentrate on further clarification of the annealing mechanism and will extend the study to multilayer systems.

ACKNOWLEDGMENT

This material is based upon work supported by the Department of Energy National Nuclear Security Administration under Award Number DE-NA0001944, the University of Rochester, and the New York State Energy Research and Development Authority. The support of DOE does not constitute an endorsement by DOE of the views expressed in this article.

REFERENCES

1. S. Papernov and A. W. Schmid, *J. Appl. Phys.* **82**, 5422 (1997).
2. S. Papernov, A. Tait, W. Bittle, A. W. Schmid, J. B. Oliver, and P. Kupinski, *J. Appl. Phys.* **109**, 113106 (2011).
3. M. Tilsch, V. Scheuer, and T. T. Tschudi, in *Optical Thin Films V: New Developments*, edited by R. L. Hall (SPIE, Bellingham, WA, 1997), Vol. 3133, pp. 163–175.
4. G. Tian *et al.*, *Appl. Surf. Sci.* **239**, 201 (2005).
5. S. Berciaud *et al.*, *Phys. Rev. B* **73**, 045424 (2006).
6. A. V. Okishev, I. A. Begishev, R. Cuffney, S. Papernov, and J. D. Zuegel, in *Solid State Lasers XXII: Technology and Devices*, edited by W. A. Clarkson and R. Shori (SPIE, Bellingham, WA, 2013), Vol. 8599, Paper 85990Q.
7. H. P. Howard, A. F. Aiello, J. G. Dressler, N. R. Edwards, T. J. Kessler, A. A. Kozlov, I. R. T. Manwaring, K. L. Marshall, J. B. Oliver, S. Papernov, A. L. Rigatti, A. N. Roux, A. W. Schmid, N. P. Slaney, C. C. Smith, B. N. Taylor, and S. D. Jacobs, *Appl. Opt.* **52**, 1682 (2013).
8. D. N. Nguyen *et al.*, *Appl. Phys. Lett.* **97**, 191909 (2010).
9. A. S. Foster *et al.*, *Phys. Rev. B* **65**, 174117 (2002).
10. S. Kičas *et al.*, in *Laser-Induced Damage in Optical Materials: 2013*, edited by G. J. Exarhos *et al.* (SPIE, Bellingham, WA, 2013), Vol. 8885, Paper 888521.
11. R. D. Richtmyer and K. W. Morton, *Difference Methods for Initial-Value Problems*, 2nd ed. (Interscience, New York, 1967).
12. W. Rudolph *et al.*, in *Laser-Induced Damage in Optical Materials: 2013*, edited by G. J. Exarhos *et al.* (SPIE, Bellingham, WA, 2013), Vol. 8885, Paper 888516.

Static and Optical Properties of Warm Dense Polystyrene Along the Principal Hugoniot

Warm dense matter (WDM) occupies a critical regime within the physics branches more traditionally addressed by condensed matter and plasma physics. WDM has recently received considerable attention because of identification with environments as diverse as the interiors of exoplanets,¹ the atmospheres of stars,² inertial confinement fusion (ICF) capsules,³ and the plasma from laser interactions⁴ with materials. Broadly, WDM spans temperatures from a few tens to several hundred electron volts and densities from 10^{21} to 10^{25} atoms/cm³, covering conditions from melt to fully ionized plasmas. Modeling this regime presents a particularly difficult challenge given that quantum mechanical effects play a crucial role in accurately representing this complex medium under extreme conditions. In addition, many of these environments constitute the dynamic interplay between mixtures of species in various physical states. Because of this complexity, few systematic experimental studies have examined its nature. One exception is ICF, in which laser-powered shocks combined with accurate diagnostic tools have begun to penetrate its intricacies and provide detailed tests of various WDM theoretical models.

For example, hydrocarbon polymers such as polystyrene (CH) and glow-discharge-polymer (GDP) plastic are often used as the ablator material in inertial confinement targets, for both indirect-drive⁵ and direct-drive⁶ ICF configurations. In ICF implosions, the ablator materials are compressed into the WDM regime by shocks. Typically, the shocked ablators can have temperatures of $T = 5$ to 50 eV and densities of $2\times$ to $10\times$ solid density. Accurate knowledge of the ablator properties in the WDM regime is just as crucial for ICF designs as the properties of the deuterium-tritium (DT) fuel.^{7–14} The static equation of state (EOS) determines the material's compressibility,¹⁵ while the dynamic and optical properties affect the thermal and radiation transports in the material.^{16–18}

Because of their importance to ICF target designs, the properties of various polymers in the WDM regime have recently been extensively studied using laser-driven shock waves. In contrast to the previous gas-gun experiment¹⁹ in the low-pressure regime ($P < 1$ Mbar), an early Nova experi-

ment²⁰ showed a stiffer behavior of CH at pressures of 10 to 40 Mbar than the Hugoniot derived from the *SESAME*²¹ and “quotidian” equation-of-state (QEOS)²² models. This has stimulated more-recent experimental studies^{23–26} of the CH Hugoniot in the 1- to 10-Mbar regime. In addition to the Hugoniot pressure, the temperature and optical reflectivity of CH shocks have also been measured in some impedance-matching experiments using the velocity interferometer system for any reflector (VISAR).^{27,28} These high-quality experimental data could advance our understanding of the properties of shocked polymers.

In general, the theoretical exploration of material properties in the WDM regime remains difficult because of the co-existence of different species including electrons, ions, atoms, and molecules in strongly coupled and degenerate conditions. To simulate such complex systems, one must adopt first-principles methods such as quantum molecular dynamics (QMD),^{29–35} path-integral Monte Carlo (PIMC),^{36–39} and coupled electron-ion Monte Carlo (CEIMC)⁴⁰ methods. For example, using the QMD method, the principal shock Hugoniots of polyethylene,⁴¹ CH,⁴² and plastic²⁶ with a composition of CH_{1.36} have recently been investigated up to ~ 15 Mbar. Noticeable differences for CH_{1.36} in the pressure range have been observed when compared to the QEOS-based Livermore EOS prediction.²⁶ For CH, the previous QMD simulations (up to only ~ 8 Mbar) by Wang *et al.*⁴² showed good agreement with a recent OMEGA experiment²⁵ but failed to predict the measured reflectivity.

In this article, we employed the QMD method to investigate the principal Hugoniot of CH up to a very high pressure of 62 Mbar. The shock pressure and temperature from our QMD calculations agree very well with recent impedance-matching measurements ($P < 10$ Mbar) on OMEGA. When compared to the *SESAME* EOS model, a stiffer behavior in CH is predicted by QMD simulations at pressures above 10 Mbar. In addition, the reflectivity discrepancy seen in previous QMD simulations⁴² has been resolved. The present QMD calculations recover the measured reflectivity only when the proper refraction index n_0 of the unshocked CH is taken into account.

The structure change in CH at 1 to 2 Mbar has been found to be consistent with the turn-on of reflectivity in both experiment and QMD calculations.

The Vienna *ab initio* simulation package (VASP)^{43–45} was used for our QMD calculations within the isokinetic ensemble (particle/volume/temperature *NVT* constant). The VASP code is based on the finite-temperature density-functional theory (FTDFT) in which electrons are treated quantum-mechanically by a plane-wave basis within the generalized gradient approximation (GGA), using the Perdew–Burke–Ernzerhof (PBE) exchange-correlation function.⁴⁶ Projector augmented wave (PAW) pseudopotentials were used to account for the core electrons. To converge the energy and pressure calculations, we set the plane-wave cutoff energy to 1000 eV and adopted hard potentials with tight cores (core radii of 1.1 and 0.8 a.u. for C and H, respectively). The system was assumed to be in local thermodynamical equilibrium with equal electron and ion temperatures ($T_e = T_i$). A periodically replicated cubic cell was used with 125 atoms for each species of H and C, with the volume of the cell determined by the CH density. For each molecular dynamics (MD) step, a set of electronic-state functions for each k point was self-consistently determined for a given ionic configuration. Then, the ions were moved classically with a velocity Verlet algorithm, according to the combined ionic and electronic forces. The ion temperature was kept constant by a simple velocity scaling. A set of self-consistent ion trajectories and electronic-wave functions resulted from the MD time propagation. These trajectories provide a consistent set of static, dynamic, and optical properties of warm dense CH. The QMD calculations employed a Γ -point ($\mathbf{k} = 0$) sampling of the first Brillouin zone in the cubic cell. Testing with a $2 \times 2 \times 2$ Monkhorst–Pack k -point grid, we found that the resulting pressure and energy varied by only $\sim 2\%$. For the lowest

temperature point, we used 650 bands and a time step of $\Delta t = 0.5$ fs, while for the highest temperature points, we employed a larger number (8000) of bands and a smaller time step of $\Delta t = 0.0325$ fs. The correlation times varied slightly at 5.0 to 6.0 fs.

To search for the shock Hugoniot of CH at a given temperature, we performed QMD calculations for two close densities differing by only ~ 0.05 g/cm³. The obtained energy and pressure were used to evaluate how far the two calculated densities were from the true Hugoniot point, which is defined by the Hugoniot equation

$$\text{Hug} = E_f - E_0 + \frac{1}{2}(P_f + P_0) \times \left(\frac{1}{\rho_f} - \frac{1}{\rho_0} \right) = 0.$$

The pressure, internal energy, and density of the initial unshocked CH are characterized by (P_0, E_0, ρ_0) , while the shock has the quantities of (P_f, E_f, ρ_f) . The initial density used in the experiments was $\rho_0 = 1.05$ g/cm³. By linearly interpolating/extrapolating through the two calculated points to make $\text{Hug} \equiv 0$, we can determine the Hugoniot point (P_h, E_h, ρ_h) for the given temperature. The principal Hugoniot of CH is displayed in Table 138.VIII, in which the shock and particle velocities $[U_s = \sqrt{\rho_h(P_h - P_0)/(\rho_h \rho_0 - \rho_0^2)}$ and $U_p = (P_h - P_0)/(\rho_0 U_s)]$, respectively, are also given. The highest calculated pressure point reached an unprecedented level of $P \sim 62$ Mbar.

To explore the change of material structure along the principal Hugoniot, we have plotted the pair-correlation functions $g(r)$ in Fig. 138.43 among ions of (a) carbon–carbon, (b) carbon–hydrogen, and (c) hydrogen–hydrogen. Figure 138.43 displays calculations for two temperatures at $T = 5000$ K (solid red line) and $T = 15,000$ K (dashed blue line), corresponding to pressures of 0.914 Mbar and 2.198 Mbar, respectively. The peaks in $g(r)$ appearing at a low temperature of 5000 K wash out as

Table 138.VIII: The principal Hugoniot of polystyrene (CH) predicted by QMD calculations.

T (K)	ρ (g/cm ³)	P (Mbar)	U_s (km/s)	U_p (km/s)	ρ/ρ_0
2,000	1.941	0.264	6.966	3.198	1.848
5,000	2.551	0.914	11.961	7.037	2.429
15,000	2.938	2.198	17.924	11.519	2.798
30,000	3.139	3.872	23.448	15.605	2.990
60,000	3.379	7.370	31.848	21.951	3.218
90,000	3.561	11.392	39.174	27.624	3.392
120,000	3.681	15.698	45.691	32.659	3.506
220,000	3.959	31.468	63.835	46.904	3.770
400,000	4.136	62.406	89.230	66.575	3.939

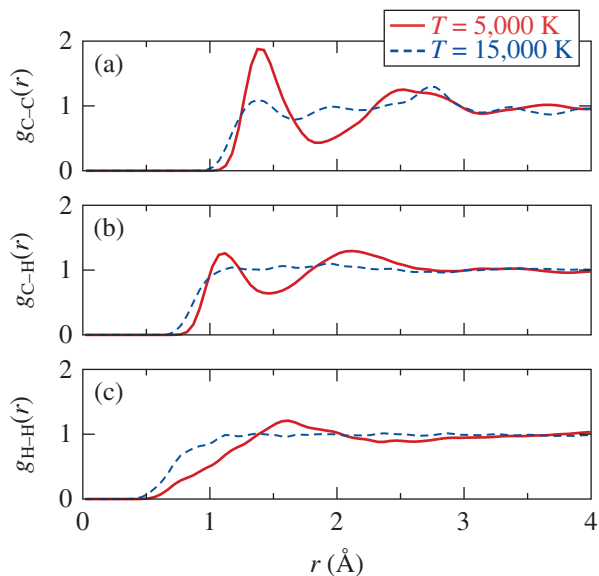


Figure 138.43

The QMD-predicted pair-correlation functions of shocked CH, along the principal Hugoniot at temperatures of $T = 5,000$ K (solid red line) and $T = 15,000$ K (dashed blue line) for (a) carbon–carbon, (b) carbon–hydrogen, and (c) hydrogen–hydrogen correlations.

the pressure increases to ~ 2 Mbar, indicating a change in the material structure around $P \simeq 1$ to 2 Mbar, which is found to be consistent with the turn-on of reflectivity (discussed below).

CH Hugoniot is compared with both experiments and models in Fig. 138.44 by plotting the pressure as a function of the shock density. The QMD results (red circles) are compared with a gas-gun experiment¹⁹ (purple triangles), a Nova experiment²⁰ (green diamonds), a recent OMEGA experiment²⁵ (blue squares), and the *SESAME* model²¹ (dashed–dotted line). It is noted that the OMEGA data have been corrected using the improved quartz standard.⁴⁷ Figure 138.44 shows that the QMD-predicted Hugoniot pressure of CH is in good agreement (within 6% or less) with recent OMEGA experiments and gas-gun experiments for pressures less than ~ 10 Mbar, in which the *SESAME* model is also close to both QMD and experiments. In the high-pressure regime ($P = 10$ to 62 Mbar), however, the QMD predictions indicate a slightly stiffer behavior than the *SESAME* model (*SESAME* 7593). For the highest pressure explored ($P \sim 62$ Mbar), the compression predicted by the QMD calculation is $\sim 5\%$ lower than what the *SESAME* model suggested. For the same density of $\rho = 4.1$ g/cm³, the QMD-predicted pressure of ~ 62 Mbar is higher than the 33 Mbar inferred from *SESAME*. It is not as stiff, however, as the early Nova experiment²⁰ indicated.

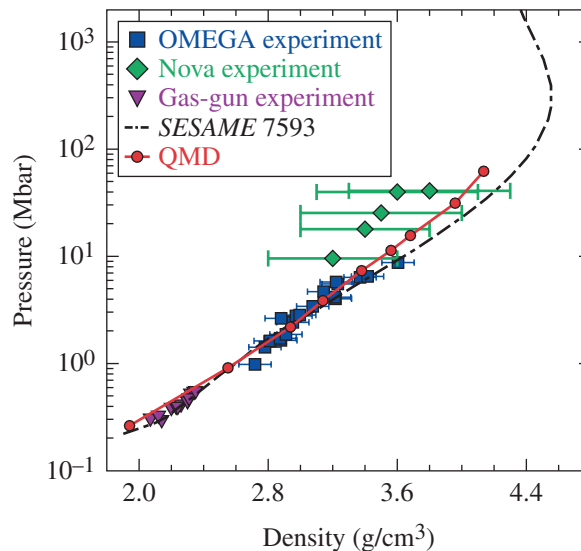


Figure 138.44

The pressure of shocked CH is plotted as a function of density, along the principal Hugoniot. The QMD results (red circles) are compared with a gas-gun experiment,¹⁹ a Nova experiment,²⁰ a recent impedance-matching experiment²⁵ on OMEGA, and *SESAME* model predictions.

In Fig. 138.45, the measured shock temperatures from the OMEGA experiment²⁵ are compared with both the QMD calculations and the *SESAME* model (*SESAME* 7593). It is found that the *SESAME* model slightly overestimates the shock temperature by $\sim 10\%$ for this low-pressure regime ($P < 10$ Mbar), while the QMD results reproduce the OMEGA measurement very well except for the highest data point. The highest data point, which has a higher temperature than both the QMD and *SESAME* predictions by 20% to 30%, might have been compromised by the normalization to that of the quartz standard.²⁵ A similar discrepancy for the highest data point was also observed in the previous QMD calculation⁴² by Wang *et al.*⁴² In the Fig. 138.45 inset, the comparison of shock temperature between QMD and the *SESAME* model has been extended to a wider range of pressures. The shock temperature predicted by QMD is higher than that of the *SESAME* model for pressures of $P > 20$ Mbar. This is consistent with the QMD-predicted stiffer behavior of CH for this high-pressure regime (see Fig. 138.44).

Finally, we examine the reflectivity of shocked CH along the principal Hugoniot. In both the OMEGA experiment²⁵ and a LULI experiment,²³ the reflectivity was determined by the signal level of the probe beam ($\lambda = 532$ nm) reflected by the CH

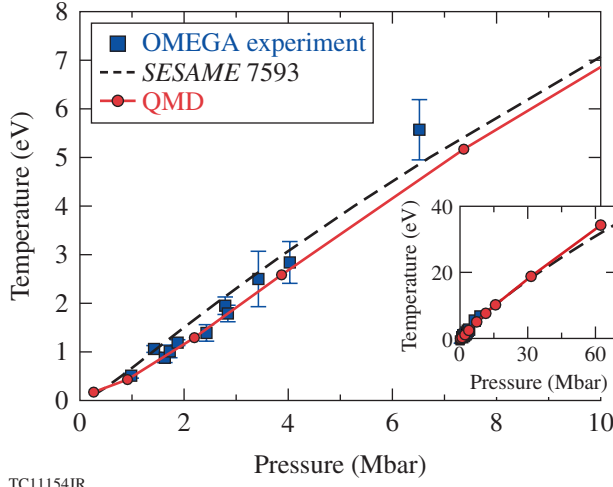


Figure 138.45

The shock temperature of CH is plotted as a function of pressure, along the principal Hugoniot. The QMD results (red circles) are compared with the recent impedance-matching experiment on OMEGA.²⁵ The inset shows the temperature comparison between the QMD prediction and the *SESAME* model to the entire explored pressure range.

shock front, which was detected by the VISAR streak camera. In the QMD calculations, we obtained a consistent set of trajectories of the ionic configuration during the molecular dynamics time propagation. We chose about ten uncorrelated snapshots of these configurations to calculate the velocity dipole matrix elements D_{mn} from the VASP wave functions. The quantity D_{mn} is used to compute the frequency-dependent Onsager coefficients within the Kubo–Greenwood formalism:⁴⁸

$$L_{ij}(\omega) = \sum_{mn} \frac{2\pi(-e)^{4-i-j}}{3Vm_e^2\omega} F_{mn} |D_{mn}|^2 \times \left(\frac{E_m + E_n}{2} - H \right)^{i+j-2} \delta(E_m - E_n - \hbar\omega), \quad (1)$$

where $V = 1/\rho$ is the atomic volume, $E_m(E_n)$ is the energy of the m th (n th) state, and H is the enthalpy (per atom) of the system. The quantity of F_{mn} is the difference between the Fermi–Dirac distributions for the m and n states at temperature T . In practical calculations, the δ function in the above equation is approximated by a Gaussian function of width ΔE ($\simeq 0.5$ eV). From the real part of the electric conductivity, $\sigma_1(\omega) = L_{11}(\omega)$, we obtain the imaginary part of the electric conductivity from a principal value integral:

$$\sigma_2(\omega) = -\frac{2}{\pi} P \left[\int \frac{\omega' \sigma_1(\omega')}{\omega'^2 - \omega^2} d\omega' \right]. \quad (2)$$

The dielectric function, $\epsilon(\omega) = \epsilon_1(\omega) + i\epsilon_2(\omega)$, can be calculated by

$$\begin{aligned} \epsilon_1(\omega) &= 1 - \frac{4\pi}{\omega} \sigma_2(\omega), \\ \epsilon_2(\omega) &= \frac{4\pi}{\omega} \sigma_1(\omega). \end{aligned} \quad (3)$$

Using the dielectric function, one obtains the real $[n(\omega)]$ and imaginary $[k(\omega)]$ parts of the refractive index:

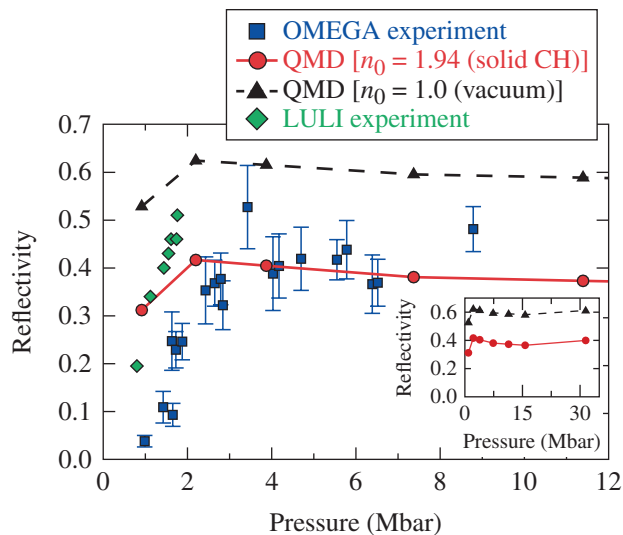
$$\begin{aligned} n(\omega) &= \sqrt{\frac{|\epsilon(\omega)| + \epsilon_1(\omega)}{2}}, \\ k(\omega) &= \sqrt{\frac{|\epsilon(\omega)| - \epsilon_1(\omega)}{2}}. \end{aligned} \quad (4)$$

Finally, the reflectivity is defined in the following general way:

$$R(\omega) = \frac{[n(\omega) - n_0]^2 + k(\omega)^2}{[n(\omega) + n_0]^2 + k(\omega)^2}, \quad (5)$$

where n_0 is the refractive index of the ambient. The choice of $n_0 = 1$ is often seen in textbooks, where the ambient is assumed to be vacuum or air. In the shock experiments, however, the reflectivity was measured as the shock propagated into the unshocked CH foil. The light reflection occurs at the interface between shocked and unshocked CH. Therefore, one must choose n_0 to be the refractive index of the unshocked CH, which was calculated to be $n_0 = 1.94$ in our QMD simulation of solid CH at room temperature. With this value of $n_0 = 1.94$, the resulting QMD reflectivity of CH shock is compared with both the OMEGA experiment²⁵ and the LULI measurement²³ in Fig. 138.46. The saturation level of the reflectivity predicted by the present QMD calculations agrees well with experiments. The turn-on of reflectivity ~ 1 to 2 Mbar is in closer agreement with the LULI experiment but seems to appear earlier than for the OMEGA experiment. If we improperly choose $n_0 = 1$, the results (black triangles) overestimate the reflectivity from $\sim 40\%$ to $\sim 60\%$. The overestimated reflection level of $\sim 60\%$ was exactly the same as what was seen in the previous QMD calculation by Wang *et al.*⁴² The inset in Fig. 138.46 plots the reflectivity for a wider range of pressures, and the reflectivity appears to be slowly increasing beyond 15-Mbar pressures, similar to the behavior seen in shocked deuterium^{18,49} occurring at $P \sim 2.8$ Mbar.

In summary, we have performed first-principles calculations for the principal Hugoniot of CH, using the QMD method. The



TC11155JR

Figure 138.46

The reflectivity of shocked CH pressure for VISAR light at $\lambda = 532$ nm along the principal Hugoniot. The QMD results, using the proper n_0 of unshocked CH (red circles) and the improper vacuum n_0 (black triangles), are compared with the LULI measurement²³ and the recent OMEGA experiment.²⁵ The inset shows the reflectivity in the entire pressure range.

QMD results agree very well with the pressure and temperature measurements up to $P = 10$ Mbar. In this pressure range, the *SESAME* model (*SESAME 7593*) predicted a similar pressure but slightly overestimated the shock temperature. For high-pressure regimes ($P = 10$ to 62 Mbar), the QMD-predicted shock temperature is higher than suggested by the *SESAME* model, thereby resulting in a stiffer CH shock in QMD simulations. Moreover, the QMD-predicted reflectivity of shocked CH agrees with a recent OMEGA experiment once the correct refraction index of the ambient (unshocked CH) is taken into account. It was found that the reflectivity starts to turn on at a somewhat smaller pressure than the recent experiment on OMEGA but appears to be closer to the LULI experiment. These results might stimulate more-accurate experiments at the high-pressure regime. Precise EOS and opacity tables based on these results could benefit fine tuning future ICF designs.

ACKNOWLEDGMENT

This material is based upon work supported by the Department of Energy National Nuclear Security Administration under Award Number DE-NA0001944, the University of Rochester, and the New York State Energy Research and Development Authority. The support of DOE does not constitute an endorsement by DOE of the views expressed in this article. This work was also supported by Scientific Campaign 10 at the Los Alamos National Laboratory, operated by Los Alamos National Security, LLC for the National Nuclear Security Administration of the U.S. Department of Energy under Contract No. DE-AC52-06NA25396.

REFERENCES

1. N. C. Santos, W. Benz, and M. Mayor, *Science* **310**, 251 (2005); A. Burrows, *Nature* **433**, 261 (2005); W. J. Borucki *et al.*, *Science* **327**, 977 (2010); S. Seager, *Science* **340**, 577 (2013).
2. G. Fontaine, P. Brassard, and P. Bergeron, *Publ. Astron. Soc. Pac.* **113**, 409 (2001).
3. B. A. Hammel *et al.*, *High Energy Density Phys.* **6**, 171 (2010).
4. K. Widmann *et al.*, *Phys. Rev. Lett.* **92**, 125002 (2004); A. Benuzzi-Mounaix *et al.*, *Phys. Rev. Lett.* **107**, 165006 (2011).
5. S. W. Haan, J. D. Lindl, D. A. Callahan, D. S. Clark, J. D. Salmonson, B. A. Hammel, L. J. Atherton, R. C. Cook, M. J. Edwards, S. Glenzer, A. V. Hamza, S. P. Hatchett, M. C. Herrmann, D. E. Hinkel, D. D. Ho, H. Huang, O. S. Jones, J. Kline, G. Kyrala, O. L. Landen, B. J. MacGowan, M. M. Marinak, D. D. Meyerhofer, J. L. Milovich, K. A. Moreno, E. I. Moses, D. H. Munro, A. Nikroo, R. E. Olson, K. Peterson, S. M. Pollaine, J. E. Ralph, H. F. Robey, B. K. Spears, P. T. Springer, L. J. Suter, C. A. Thomas, R. P. Town, R. Vesey, S. V. Weber, H. L. Wilkens, and D. C. Wilson, *Phys. Plasmas* **18**, 051001 (2011).
6. D. D. Meyerhofer, R. L. McCrory, R. Betti, T. R. Boehly, D. T. Casey, T. J. B. Collins, R. S. Craxton, J. A. Delettrez, D. H. Edgell, R. Epstein, K. A. Fletcher, J. A. Frenje, Y. Yu. Glebov, V. N. Goncharov, D. R. Harding, S. X. Hu, I. V. Igumenshchev, J. P. Knauer, C. K. Li, J. A. Marozas, F. J. Marshall, P. W. McKenty, P. M. Nilson, S. P. Padalino, R. D. Petrasso, P. B. Radha, S. P. Regan, T. C. Sangster, F. H. Séguin, W. Seka, R. W. Short, D. Shvarts, S. Skupsky, J. M. Soures, C. Stoeckl, W. Theobald, and B. Yaakobi, *Nucl. Fusion* **51**, 053010 (2011); R. L. McCrory, R. Betti, T. R. Boehly, D. T. Casey, T. J. B. Collins, R. S. Craxton, J. A. Delettrez, D. H. Edgell, R. Epstein, J. A. Frenje, D. H. Froula, M. Gatu-Johnson, V. Yu. Glebov, V. N. Goncharov, D. R. Harding, M. Hohenberger, S. X. Hu, I. V. Igumenshchev, T. J. Kessler, J. P. Knauer, C. K. Li, J. A. Marozas, F. J. Marshall, P. W. McKenty, D. D. Meyerhofer, D. T. Michel, J. F. Myatt, P. M. Nilson, S. J. Padalino, R. D. Petrasso, P. B. Radha, S. P. Regan, T. C. Sangster, F. H. Séguin, W. Seka, R. W. Short, A. Shvydky, S. Skupsky, J. M. Soures, C. Stoeckl, W. Theobald, B. Yaakobi, and J. D. Zuegel, *Nucl. Fusion* **53**, 113021 (2013).
7. L. Caillabet, S. Mazevet, and P. Loubeyre, *Phys. Rev. B* **83**, 094101 (2011).
8. L. Caillabet *et al.*, *Phys. Rev. Lett.* **107**, 115004 (2011).
9. P. Loubeyre, S. Brygoo, J. Eggert, P. M. Celliers, D. K. Spaulding, J. R. Rygg, T. R. Boehly, G. W. Collins, and R. Jeanloz, *Phys. Rev. B* **86**, 144115 (2012).
10. S. X. Hu, B. Militzer, V. N. Goncharov, and S. Skupsky, *Phys. Rev. Lett.* **104**, 235003 (2010).
11. S. X. Hu, B. Militzer, V. N. Goncharov, and S. Skupsky, *Phys. Rev. B* **84**, 224109 (2011).
12. M. A. Morales *et al.*, *High Energy Density Phys.* **8**, 5 (2012).
13. J. Vorberger, D. O. Gericke, and W. D. Kraeft, *High Energy Density Phys.* **9**, 448 (2013).

14. V. V. Karasiev *et al.*, Phys. Rev. B **88**, 161108 (2013).
15. S. X. Hu, V. A. Smalyuk, V. N. Goncharov, J. P. Knauer, P. B. Radha, I. V. Igumenshchev, J. A. Marozas, C. Stoeckl, B. Yaakobi, D. Shvarts, T. C. Sangster, P. W. McKenty, D. D. Meyerhofer, S. Skupsky, and R. L. McCrory, Phys. Rev. Lett. **100**, 185003 (2008).
16. V. Recoules *et al.*, Phys. Rev. Lett. **102**, 075002 (2009).
17. C. E. Starrett *et al.*, Phys. Plasmas **19**, 102709 (2012).
18. S. X. Hu, L. A. Collins, T. R. Boehly, V. N. Goncharov, and S. Skupsky, Phys. Rev. E **89**, 043105 (2014).
19. S. P. Marsh, ed. *LASL Shock Hugoniot Data*, Los Alamos Series on Dynamic Material Properties (University of California Press, Berkeley, CA, 1980).
20. R. Cauble *et al.*, Phys. Plasmas **4**, 1857 (1997).
21. B. I. Bennett *et al.*, Los Alamos National Laboratory, Los Alamos, NM, Report LA-7130 (1978).
22. R. M. More *et al.*, Phys. Fluids **31**, 3059 (1988).
23. M. Koenig *et al.*, Phys. Plasmas **10**, 3026 (2003).
24. N. Ozaki *et al.*, Phys. Plasmas **16**, 062702 (2009).
25. M. A. Barrios, D. G. Hicks, T. R. Boehly, D. E. Fratanduono, J. H. Eggert, P. M. Celliers, G. W. Collins, and D. D. Meyerhofer, Phys. Plasmas **17**, 056307 (2010).
26. S. Hamel, L. X. Benedict, P. M. Celliers, M. A. Barrios, T. R. Boehly, G. W. Collins, T. Döppner, J. H. Eggert, D. R. Farley, D. G. Hicks, J. L. Kline, A. Lazicki, S. LePape, A. J. Mackinnon, J. D. Moody, H. F. Robey, E. Schwegler, and P. A. Sterne, Phys. Rev. B **86**, 094113 (2012).
27. P. M. Celliers *et al.*, Appl. Phys. Lett. **73**, 1320 (1998).
28. P. M. Celliers, D. K. Bradley, G. W. Collins, D. G. Hicks, T. R. Boehly, and W. J. Armstrong, Rev. Sci. Instrum. **75**, 4916 (2004).
29. J. G. Clérouin and S. Bernard, Phys. Rev. E **56**, 3534 (1997).
30. L. A. Collins *et al.*, Phys. Rev. B **63**, 184110 (2001).
31. M. P. Desjarlais, J. D. Kress, and L. A. Collins, Phys. Rev. E **66**, 025401 (2002).
32. M. P. Desjarlais, Phys. Rev. B **68**, 064204 (2003).
33. S. A. Bonev, B. Militzer, and G. Galli, Phys. Rev. B **69**, 014101 (2004).
34. B. Holst, R. Redmer, and M. P. Desjarlais, Phys. Rev. B **77**, 184201 (2008).
35. B. Holst, M. French, and R. Redmer, Phys. Rev. B **83**, 235120 (2011).
36. C. Pierleoni *et al.*, Phys. Rev. Lett. **73**, 2145 (1994).
37. B. Militzer and D. M. Ceperley, Phys. Rev. Lett. **85**, 1890 (2000).
38. B. Militzer *et al.*, Phys. Rev. Lett. **87**, 275502 (2001).
39. K. P. Driver and B. Militzer, Phys. Rev. Lett. **108**, 115502 (2012).
40. J. M. McMahon *et al.*, Rev. Mod. Phys. **84**, 1607 (2012).
41. T. R. Mattsson *et al.*, Phys. Rev. B **81**, 054103 (2010).
42. C. Wang, X.-T. He, and P. Zhang, Phys. Plasmas **18**, 082707 (2011).
43. G. Kresse and J. Hafner, Phys. Rev. B **47**, 558 (1993).
44. G. Kresse and J. Hafner, Phys. Rev. B **49**, 14251 (1994).
45. G. Kresse and J. Furthmüller, Phys. Rev. B **54**, 11169 (1996).
46. J. P. Perdew, K. Burke, and M. Ernzerhof, Phys. Rev. Lett. **77**, 3865 (1996); J. P. Perdew, K. Burke, and M. Ernzerhof, Phys. Rev. Lett. **78**, 1396 (1997).
47. M. D. Knudson and M. P. Desjarlais, Phys. Rev. Lett. **103**, 225501 (2009).
48. R. Kubo, J. Phys. Soc. Jpn. **12**, 570 (1957); D. A. Greenwood, Proc. Phys. Soc. Lond. **71**, 585 (1958).
49. L. A. Collins, J. D. Kress, and D. E. Hanson, Phys. Rev. B **85**, 233101 (2012).

Fabrication of a Continuous-Enfolded Grating by Ion-Beam–Sputter Deposition

Introduction

The concept of depositing a corrugated multilayer dielectric reflector on a sinusoidal diffraction-grating surface as described by Li and Hirsh¹ is attractive for high-laser-damage applications since the diffraction grating does not contain contaminants from the grating patterning and etching processes, as is typical for multilayer dielectric diffraction gratings.^{1–4} The concept behind such a grating is that each layer in the multilayer structure acts as a diffractive element, with the overall diffraction efficiency of the grating being the combined efficiency of all the layers. When such a device is fabricated, any patterning, etching, or replication to provide the surface relief is done on the substrate surface, with low-absorption materials then deposited to achieve high diffraction efficiency. In this manner, the incident laser light encounters only high-damage-threshold materials, having sufficiently reflected and/or diffracted before reaching any remaining organic materials at the substrate surface. The performance of such a structure can be calculated based on the electric-field contributions from each interface, taking into account the local curvature of the surface relief as demonstrated by Li.⁵ The primary remaining challenge in such an approach is to improve the contour conformation of the coated dielectric layers, with traditional coating methods leading to a planarization of the surface relief, as illustrated in

Fig. 138.47(a) (Ref. 1). The goal in depositing such a coating is that each layer interface should have an identical surface relief, by depositing a consistent thickness over the surface structure regardless of the local orientation, as shown in Fig. 138.47(b).

Ion-beam sputtering (IBS) typically produces high-quality optical coatings, characterized by a dense film structure exhibiting low scatter and low absorption.^{6,7} By using appropriate high-band-gap materials, IBS may produce high-quality films suitable for high-fluence laser applications.⁸ In addition, IBS is based on the ablation of target material using a directional ion source, with film deposition resulting from well-characterized momentum transfer of the ions incident on the target surface. The resulting deposition source is of an extended-area, relative to evaporation sources that appear to be a point for sufficiently large deposition systems. In this manner, larger substrates may be coated with a directional deposition, rather than being limited by the extent of an evaporation source.

This effort describes a collimated IBS process and its application for depositing a conformal multilayer reflector over a sinusoidal diffraction grating. By conformally depositing alternating hafnia and silica dielectric layers to enhance a silver layer on a nominal 1740-lines/mm sinusoidal grating, a

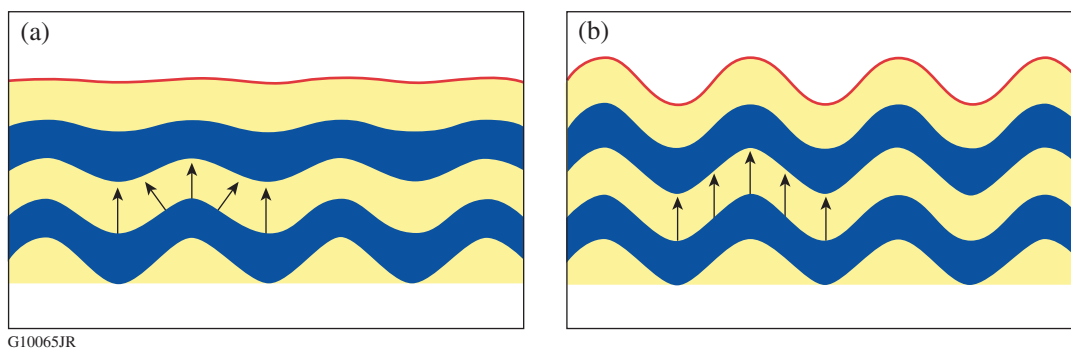


Figure 138.47

(a) Growth of the multilayer film over the grating normal to the *local* surface leads to rapid planarization of the grating structure. (b) Collimated deposition, with equal growth across the surface relief in the direction normal to the substrate plane, preserves the grating surface relief through the multilayer.

diffraction efficiency of 93% has been achieved for *p*-polarized light incident from the air surface. Laser-damage testing indicates that by using this type of structure, a 1-on-1 fluence of $2.66 \pm 0.15 \text{ J/cm}^2$ can be achieved at 1053-nm, 65° incidence with a 10-ps pulse. Modifications will be necessary to deposit both the metal and dielectric layers in a single coating cycle, and further improvements calibrating the conformal structure will be pursued. The transfer function of the layered surface relief must be determined under different deposition conditions, but the demonstrated control suggests that continuous-enfolded gratings may be fabricated with high diffraction efficiency by using this method.

Background

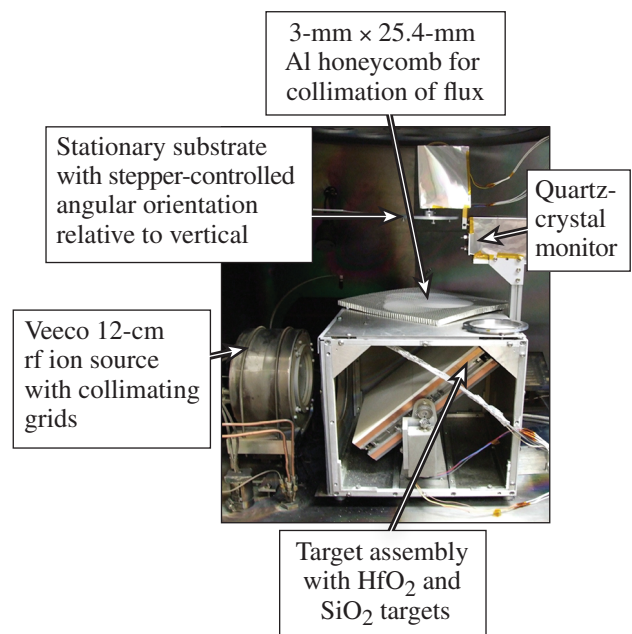
The basis of the continuous-enfolded grating structure is that the superposition of individual diffracted components from each layer in the multilayer coating results in overall high diffraction efficiency. The absorption present in a metallic coating limits the possible laser-damage threshold, so it is necessary to use a high-damage-threshold dielectric interference coating to limit the electric-field intensity striking the metal surface, increasing the overall laser-damage resistance of the diffraction grating. Each layer, however, must be conformally mapped to the surface beneath. Growth of a layer perpendicular to the local grating surface would rapidly planarize the grating structure; instead, the surface relief must be maintained in each layer, which is equivalent to uniform film growth perpendicular to the substrate surface without regard to the location or surface profile.

While evaporated coating processes can be designed to provide a uniform film thickness over a substrate surface, the angles of incidence on the substrate surface influence the relative thickness with a cosine dependence.⁹ Furthermore, the source extent is generally quite small, limiting the region that may be coated with a collimated evaporant vapor flux. Sputtering processes make use of extended target sources that might be configured to provide an incident vapor flux of small angular extent, even over an extended substrate aperture. Control of the source distribution and/or the orientation of the substrate surface was considered to yield the desired deposition profile over a sinusoidal grating structure.

Experimental Procedure

A single deposition system was not available to meet all needs in investigating this coating, so it was necessary to use three different coating chambers throughout this process: First, an MRC 902M magnetron sputtering system was used to deposit a layer of aluminum over a photoresist-patterned

grating to preserve the grating structure during epoxy replication. The aluminum film remained on the replicated grating, but the evaporation of an 80- to 100-nm-thick silver layer over the aluminum in a 54-in. coating chamber configured with a traditional planetary rotation was required to increase diffraction efficiency. This may also have the added benefit of preventing any remaining organic contaminants from the photoresist from being exposed to the incident laser intensity. The silver-coated replicated grating was then mounted in a custom 46-in. ion-beam-sputtering system equipped with a 12-cm Veeco radio-frequency (rf) ion source with converging grids, a rotatable target mount with hafnia and silica targets, a 25.4-mm-thick aluminum honeycomb filter with 3-mm hexagonal cells to collimate the vapor, and a stepper-motor-driven oscillating substrate mount as shown in Fig. 138.48. Coating thickness was controlled with a single quartz-crystal monitor.



G10067JR

Figure 138.48

Experimental ion-beam-sputtering system for depositing hafnia/silica multilayer coatings over a sinusoidal grating structure. The target assembly was rotated to select a hafnium-dioxide or silicon-dioxide target, while the grating substrate remained directly above the target, oscillating in a controlled manner to provide uniform coating distribution over the surface relief of the grating. rf: radio frequency.

The deposited-coating design is an enhanced silver reflector with seven dielectric layers deposited over the metal coating:

Al-coated grating / Ag / 0.9L HHLHL / air,

where L and H represent quarter-wave optical thicknesses at 1053 nm of silica and hafnia, respectively. This design provides a reflectance of greater than 99% at 1053 nm in p polarization over an angle range of 62° to 72° . The substrate is an epoxy-replicated sinusoidal grating with 1740 lines/mm and a depth of ~ 150 nm, coated with an aluminum release layer (transferred from the original photoresist master grating). At this time we have not identified a method for cleaning the replicated grating, so deposition is performed on the aluminum, with potential contaminants remaining from the photoresist master grating. The opaque silver layer is evaporated while the substrate is rotated in a planetary rotation system. The IBS process is carried out with the substrate positioned directly above the source and oscillating to $\pm 26^\circ$ from the incident vapor flux, with a 5-min dwell time at each end of the oscillation as shown in Fig. 138.49. The substrate continues to oscillate in this manner throughout the deposition of each layer, with average deposition times for individual layers being greater than 3 h.

Diffraction efficiency was measured with a 1053-nm laser source. Laser-damage testing was performed at 1053 nm with 10-ps pulses at 66° incidence in air with standard damage-test protocols.⁴ Finally, the samples were cleaved and cross-section scanning electron microscopy was performed to characterize the conformal mapping of the coating to the underlying grating structure. Grating samples were mounted, coated with a thin layer of platinum, and imaged in a Zeiss 1530 scanning electron microscope (SEM), using in-lens secondary electron imaging as well as backscatter detection to enhance the contrast of the individual layers.

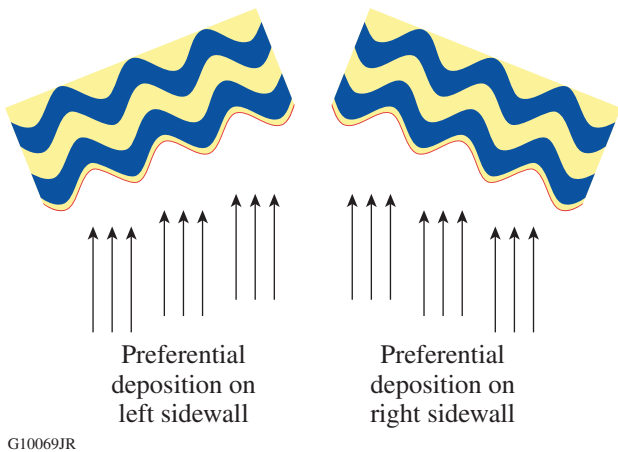


Figure 138.49 Oscillation of the grating surface relief to $\pm\theta$ provides improved deposition on the grating sidewalls and reduced planarization.

Results and Discussion

An evaporated coating deposition over a surface-relief grating was performed previously, confirming the challenges associated with coating over a grating structure as identified by Li and Hirsh.^{1,10} A cross-sectional image is shown in Fig. 138.50(a), with a clear planarization within approximately eight layers.¹⁰ The use of a collimated IBS process makes it possible to deposit a similar number of layers over a grating surface, but with a much higher degree of conformal mapping, as shown in Figs. 138.50(b)–138.50(e). The grating image in Fig. 138.50(b) results from a deposition without oscillation of the substrate above the source, showing greater deposited thickness in the minima of the grating profile and leading to sharper peaks in the maxima. The grating images in Figs. 138.50(c) and 138.50(d) also appear to have relatively sharp peaks, incorporating oscillation and honeycomb filtration, respectively, leading to a somewhat triangular shape in the grating profile. As seen in Fig. 138.50(e), this may be rounded somewhat by

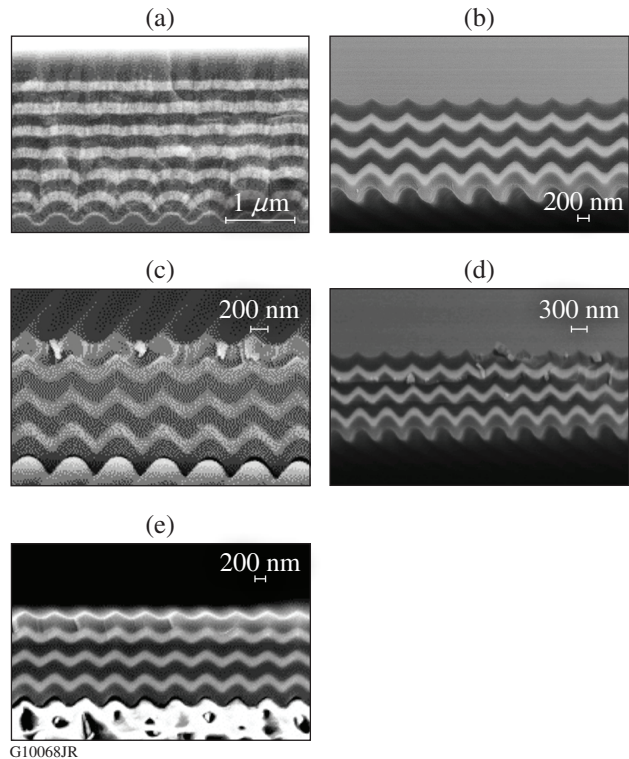


Figure 138.50 Scanning electron micrographs of multilayer interference coatings deposited over nominally sinusoidal diffraction-grating surfaces. The coating deposited by (a) electron-beam deposition quickly planarized, while (b) the IBS coating showed significant promise. The addition of (c) an aluminum honeycomb to improve vapor flux collimation, (d) $\pm 26^\circ$ substrate oscillation, and (e) a 0° dwell in the tip-tilt substrate oscillations significantly improved the conformal properties of the coating deposition.

dwelling at a normal-incidence deposition position for 1 min between the 5-min depositions at $\pm 26^\circ$ substrate orientation (as measured from normal-incidence vapor flux). Deposition with the relatively collimated IBS source on the stationary grating structure provides improved control of the film-growth direction, enabling one to fabricate a conformal multilayer structure.

The performance of the grating in Fig. 138.50(e) was evaluated for diffraction efficiency and laser-damage threshold. Given that the coating process was executed in three separate deposition systems and the epoxy replication process proved to be difficult, there were large regions of the 100-mm substrate where the coating delaminated from the epoxy surface. In the central region of the grating, however, there remained a test area with 93% diffraction efficiency and a 1-on-1 laser-damage threshold of $2.66 \pm 0.15 \text{ J/cm}^2$ for 1053-nm, 65° incidence with a 10-ps pulse. For our initial effort, this result is quite encouraging since significant degradation of the laser-damage resistance is expected as the diffraction efficiency is decreased from the theoretical maximum of 98% for a sinusoidal continuous-enfolded grating at 1740 lines/mm. Such a degradation in efficiency leads to significant electric-field enhancement from multibeam interference of the incident, reflected, and diffracted components. Furthermore, this represents a significant improvement relative to the 84% diffraction efficiency reported by Li and Hirsh,¹ which required illumination from the substrate side of the grating, a configuration with negligible functionality for a high-fluence laser application.

To increase the utility of this grating fabrication technique, improved grating-performance modeling as a function of the profile of each layer is being pursued to determine the impact of deviations from a perfect sinusoidal shape. Control of variations in the conformal structure can be realized depending on the oscillation profile, particularly between the images in Figs. 138.50(c) and 138.50(e), where a normal-incidence deposition was added between each $\pm 26^\circ$ deposition. Deposition perpendicular to the substrate surface can lead to planarization, given the high arrival energies of the ion-beam-sputtered flux, while deposition at high angles appears to lead to an alteration of the grating profile to more of a triangular or saw-toothed shape. The surface mobility of sputtered material can be significant for high arrival energies and impact at a glancing angle relative to the local substrate surface relief. By orienting the local surface relief normal to the incident flux, the mobility of arriving material can be limited.

The ideal grating shape must be determined for fabrication prior to the coating deposition, which, in conjunction with the transfer function of the coating process, determines the overall grating performance. Reactive ion etching, epoxy replication, and even direct coating of the developed photoresist grating are all possible means of fabricating a substrate with the appropriate surface-relief profile prior to deposition of the multilayer coating, but maintaining such a profile over large apertures is essential for developing a suitable production process. As larger substrates with high-quality surface relief become available, it is expected that a linear translation system will be incorporated to uniformly deposit over large apertures.

Conclusions

A continuous-enfolded grating has been demonstrated with 93% diffraction efficiency and a laser-damage threshold of $2.66 \pm 0.15 \text{ J/cm}^2$ at 1053-nm, 65° incidence in *p* polarization when tested in an *N*-on-1 configuration with a 10-ps pulse. The coating consists of a silver layer overcoated with ion-beam-sputtered hafnia and silica layers to provide greater than 99% reflectivity. SEM imaging shows good conformal mapping of the coating to the underlying grating structure, with available controls within the process to adjust the evolution of the grating profile throughout the layers. Efforts will continue to integrate the coating process in a single deposition system, better characterize the deposited film, develop a means to better clean the replicated grating prior to deposition, and expand the usable area of the coated grating. Improved modeling of the variations in the grating profile should lead to greater diffraction efficiency and laser-damage resistance.

ACKNOWLEDGMENT

The authors express their appreciation to H. Huang for grating modeling and A. Kozlov for providing laser-damage-threshold measurements of the completed grating. This material is based upon work supported by the Department of Energy National Nuclear Security Administration under Award Number DE-NA0001944, the University of Rochester, and the New York State Energy Research and Development Authority. The support of DOE does not constitute an endorsement by DOE of the views expressed in this article.

REFERENCES

1. L. Li and J. Hirsh, *Opt. Lett.* **20**, 1349 (1995).
2. J. A. Britten *et al.*, in *Laser-Induced Damage in Optical Materials: 1995*, edited by H. E. Bennett *et al.* (SPIE, Bellingham, WA, 1996), Vol. 2714, pp. 511–520.
3. M. D. Perry *et al.*, *Opt. Lett.* **20**, 940 (1995).

4. H. P. Howard, A. F. Aiello, J. G. Dressler, N. R. Edwards, T. J. Kessler, A. A. Kozlov, I. R. T. Manwaring, K. L. Marshall, J. B. Oliver, S. Papernov, A. L. Rigatti, A. N. Roux, A. W. Schmid, N. P. Slaney, C. C. Smith, B. N. Taylor, and S. D. Jacobs, *Appl. Opt.* **52**, 1682 (2013).
5. L. Li, *J. Opt. Soc. Am. A* **11**, 2816 (1994).
6. D. T. Wei and A. W. Louderback, U.S. Patent No. 4,142,958 (6 March 1979).
7. D. T. Wei, *Appl. Opt.* **28**, 2813 (1989).
8. X. Fu *et al.*, in *Laser-Induced Damage in Optical Materials: 2012*, edited by G. J. Exarhos *et al.* (SPIE, Bellingham, WA, 2012), Vol. 8530, Paper 85300X.
9. J. B. Oliver and D. Talbot, *Appl. Opt.* **45**, 3097 (2006).
10. J. B. Oliver, <http://www.optics.rochester.edu/workgroups/cml/opt307/spr04/jim/> (12 February 2014).

Publications and Conference Presentations

Publications

- S.-W. Bahk, J. Bromage, and J. D. Zuegel, "Offner Radial Group Delay Compensator for Ultra-Broadband Laser Beam Transport," *Opt. Lett.* **39**, 1081 (2014).
- C. Dorrer, "Spectral and Temporal Properties of Optical Signals with Multiple Sinusoidal Phase Modulations," *Appl. Opt.* **53**, 1007 (2014).
- M. Hohenberger, W. Theobald, S. X. Hu, K. S. Anderson, R. Betti, T. R. Boehly, A. Casner, D. E. Fratanduono, M. Lafon, D. D. Meyerhofer, R. Nora, X. Ribeyre, T. C. Sangster, G. Schurtz, W. Seka, C. Stoeckl, and B. Yaakobi, "Shock-Ignition Relevant Experiments with Planar Targets on OMEGA," *Phys. Plasmas* **21**, 022702 (2014).
- O. A. Hurricane, D. A. Callahan, D. T. Casey, P. M. Celliers, C. Cerjan, E. L. Dewald, T. R. Dittrich, T. Döppner, D. E. Hinkel, L. F. Berzak Hopkins, J. L. Kline, S. Le Pape, T. Ma, A. G. MacPhee, J. L. Milovich, A. Pak, H.-S. Park, P. K. Patel, B. A. Remington, J. D. Salmonson, P. T. Springer, and R. Tommasini, "Fuel Gain Exceeding Unity in an Inertially Confined Fusion Implosion," *Nature* **506**, 343 (2014).
- R. L. McCrory, D. D. Meyerhofer, R. Betti, T. R. Boehly, D. T. Casey, T. J. B. Collins, R. S. Craxton, J. A. Delettrez, D. H. Edgell, R. Epstein, J. A. Frenje, D. H. Froula, M. Gatu-Johnson, V. Yu. Glebov, V. N. Goncharov, D. R. Harding, M. Hohenberger, S. X. Hu, I. V. Igumenshchev, T. J. Kessler, J. P. Knauer, C. K. Li, J. A. Marozas, F. J. Marshall, P. W. McKenty, D. T. Michel, J. F. Myatt, P. M. Nilson, S. J. Padalino, R. D. Petrasso, P. B. Radha, S. P. Regan, T. C. Sangster, F. H. Séguin, W. Seka, R. W. Short, A. Shvydky, S. Skupsky, J. M. Soures, C. Stoeckl, W. Theobald, B. Yaakobi, and J. D. Zuegel, "Progress Toward Polar-Drive Ignition for the NIF," in *Proceedings of the 24th IAEA Fusion Energy Conference* (IAEA, Vienna, 2013), Paper IFE 2-1.
- M. Mikulics, H. Hardtdegen, R. Adam, D. Grützmacher, D. Gregušová, J. Novák, P. Kordoš, Z. Sofer, J. Serafini, J. Zhang, R. Sobolewski, and M. Marso, "Impact of Thermal Annealing on Nonequilibrium Carrier Dynamics in Single-Crystal, Freestanding GaAs Mesostructures," *Semicond. Sci. Technol.* **29**, 045022 (2014).
- A. V. Okishev, "Abnormal Beam-Profile Behavior in a Nd:YAG Ceramic Regenerative Amplifier," in *Solid State Lasers XXIII: Technology and Devices*, edited by W. A. Clarkson and R. K. Shori (SPIE, Bellingham, WA, 2014), Vol. 8959, Paper 89591O.
- J. B. Oliver, J. Bromage, C. Smith, D. Sadowski, C. Dorrer, and A. L. Rigatti, "Plasma-Ion-Assisted Coatings for 15 Femtosecond Laser Systems," *Appl. Opt.* **53**, A221 (2014).
- S. Papernov, A. A. Kozlov, J. B. Oliver, T. J. Kessler, and B. Marozas, "Near-Ultraviolet Absorption-Annealing Effects in HfO₂ Thin Films Subjected to Continuous-Wave Laser Irradiation at 355 nm," in *Laser-Induced Damage in Optical Materials: 2013*, edited by G. J. Exarhos, V. E. Gruzdev, J. A. Menapace, D. Ristau, and M. J. Soileau (SPIE, Bellingham, WA, 2013), Vol. 8885, Paper 888504.
- H. F. Robey, P. M. Celliers, J. D. Moody, J. Sater, T. Parham, B. Kozioziemski, R. Dylla-Spears, J. S. Ross, S. LePape, J. E. Ralph, M. Hohenberger, E. L. Dewald, L. Berzak Hopkins, J. J. Kroll, B. E. Yoxall, A. V. Hamza, T. R. Boehly, A. Nikroo, O. L. Landen, and M. J. Edwards, "Shock Timing Measurements and Analysis in Deuterium-Tritium-Ice Layered Capsule Implosions on NIF," *Phys. Plasmas* **21**, 022703 (2014).
- J. E. Schoenly, W. Seka, and P. Rechmann, "Pulsed Laser Ablation of Dental Calculus in the Near Ultraviolet," *J. Biomed. Opt.* **19**, 028003 (2014).

Forthcoming Publications

D. Eimerl, E. M. Campbell, W. F. Krupke, J. Zweiback, W. L. Kruer, J. Marozas, J. Zuegel, J. Myatt, J. Kelly, D. Froula, and R. L. McCrory, “StarDriver: A Flexible Laser Driver for Inertial Confinement Fusion and High Energy Density Physics,” to be published in the *Journal of Fusion Energy*.

V. N. Goncharov, T. C. Sangster, R. Betti, T. R. Boehly, T. J. B. Collins, R. S. Craxton, J. A. Delettrez, D. H. Edgell, R. Epstein, C. J. Forrest, D. H. Froula, V. Yu. Glebov, D. R. Harding, S. X. Hu, I. V. Igumenshchev, R. Janezic, J. H. Kelly, T. J. Kessler, T. Z. Kosc, S. J. Loucks, J. A. Marozas, F. J. Marshall, A. V. Maximov, R. L. McCrory, P. W. McKenty, D. D. Meyerhofer, D. T. Michel, J. F. Myatt, R. Nora, P. B. Radha, S. P. Regan, W. Seka, W. T. Shmayda, R. W. Short, A. Shvydky, S. Skupsky, C. Sorce, C. Stoeckl, B. Yaakobi, J. A. Frenje, M. Gatu Johnson, R. D. Petrasso, and D. T. Casey, “Improving the Hot-Spot Pressure and Demonstrating Ignition Hydrodynamic Equivalence in Cryogenic Deuterium–Tritium Implosions on OMEGA,” to be published in *Physics of Plasmas* (invited).

D. Haberberger, S. Ivancic, S. X. Hu, R. Boni, M. Barczys, R. S. Craxton, and D. H. Froula, “Measurements of the Electron Density Profiles Using an Angular Filter Refractometer,” to be published in *Physics of Plasmas* (invited).

S. X. Hu, L. A. Collins, T. R. Boehly, V. N. Goncharov, and S. Skupsky, “First-Principles Thermal Conductivity of Deuterium for Inertial Confinement Fusion Applications,” to be published in *Physical Review E*.

J. F. Myatt, A. V. Maximov, A. A. Solodov, J. Zhang, R. S. Craxton, C. Ren, R. Yan, I. V. Igumenshchev, S. X. Hu, V. N. Goncharov, W. Seka, D. H. Edgell, D. H. Froula, B. Yaakobi, D. T. Michel, D. F. DuBois, D. A. Russell, D. E. Hinkel, P. Michel, and H. X. Vu, “Multibeam Laser–Plasma Interac-

tions in Inertial Confinement Fusion,” to be published in *Physics of Plasmas* (invited).

T. Nagayama, R. C. Mancini, R. Florido, D. Mayes, R. Tommasini, J. A. Koch, J. A. Delettrez, S. P. Regan, and V. A. Smalyuk, “Direct Asymmetry Measurement of Temperature and Density Spatial Distributions in Inertial Confinement Fusion Plasmas From Pinhole Space-Resolved Spectra,” to be published in *Physics of Plasmas*.

R. Nora, R. Betti, K. S. Anderson, A. Shvydky, A. Bose, K. M. Woo, A. R. Christopherson, J. A. Marozas, T. J. B. Collins, P. B. Radha, S. X. Hu, R. Epstein, F. J. Marshall, T. C. Sangster, and D. D. Meyerhofer, “Theory of Hydro-Equivalent Ignition for Inertial Fusion and Its Applications to OMEGA and the NIF,” to be published in *Physics of Plasmas* (invited).

H. G. Rinderknecht, H. Sio, C. K. Li, A. B. Zylstra, M. J. Rosenberg, P. Amendt, J. Delettrez, C. Bellei, J. A. Frenje, M. Gatu Johnson, F. H. Séguin, R. D. Petrasso, R. Betti, V. Yu. Glebov, D. D. Meyerhofer, T. C. Sangster, C. Stoeckl, O. Landen, V. A. Smalyuk, S. Wilks, A. Greenwood, and A. Nikroo, “First Observations of Nonhydrodynamic Mix at the Fuel–Shell Interface in Shock-Driven Inertial Confinement Implosions,” to be published in *Physical Review Letters*.

W. Seka, J. F. Myatt, R. W. Short, D. H. Froula, J. Katz, V. N. Goncharov, and I. V. Igumenshchev, “Localized Time-Resolved Electron Temperature Measurements Indicate Non-uniformly Driven Two-Plasmon–Decay Instability in Direct-Drive Implosions,” to be published in *Physical Review Letters*.

H. X. Vu, D. F. DuBois, D. A. Russell, J. F. Myatt, and J. Zhang, “Nonlinear Development of the Two-Plasmon–Decay Instability in Three Dimensions,” to be published in *Physics of Plasmas*.

Conference Presentations

A. V. Okishev, "Abnormal Beam-Profile Behavior in a Nd:YAG Ceramic Regenerative Amplifier," Photonics West, San Francisco, CA, 1–6 February 2014.

D. H. Barnak, G. Fiksel, H. Chen, P.-Y. Chang, and D. D. Meyerhofer, "Positron Focusing Using Externally Applied Axially Symmetric Magnetic Fields," NIF and JLF User Group Meeting, Livermore, CA, 9–12 February 2014.

T. Jacobs, M. Mayton, Z. Hobbs, and S. D. Jacobs, "Process Improvements and Future Work for Flint Creek Resources' Cerium Oxide Reclamation Project," The Institute of Optics Industrial Associates Meeting, Rochester, NY, 3 March 2014.

C. Stoeckl, R. Epstein, G. Fiksel, D. Guy, V. N. Goncharov, D. W. Jacobs-Perkins, R. K. Junquist, C. Mileham, P. M. Nilson, T. C. Sangster, M. J. Shoup III, and W. Theobald, "Soft X-Ray Backlighting of Cryogenic Implosions Using a Narrowband Crystal Imaging System," COST LMJ Meeting, Bordeaux, France, 5–7 March 2014.

